



**UNIVERSITÁ DEGLI STUDI DI ROMA  
TOR VERGATA**

FACOLTÁ DI INGEGNERIA

CORSO DI LAUREA IN INGEGNERIA MECCANICA

A.A. 2013/2014

**Tesi di Laurea Magistrale**

Goal driven multi-objective shape optimization for conjugate heat transfer in an effusion cooling system of a combustion chamber, through a CFD-mesh-morphing based approach.

**RELATORE**

Prof. Marco E. Biancolini

**LAUREANDO**

Walter Savastano  
0185986

**CORRELATORE**

Prof. Gordon E. Andrews  
Ing. Alessandro Pranzitelli

*Ai Miei Genitori Nino e Daniela,  
Che mi hanno sempre sostenuto  
e supportato nel mio percorso*

# Abstract

Full coverage effusion cooling was studied for a square array of 90° effusion cooling holes. Active cooling was used with Nimonic 75 wall, and 300 K effusion cooling into a 27 m/s mean velocity duct flow at 770K crossflow temperature. First wall investigated for the validation of the experimental results had square arrays of normal holes with the same total cooled wall size 152x152mm.

The injection holes length was 6.35mm. Diameter of the holes was 3.27mm, and call X the pitch between the holes, ratio  $X/D=4.6$ . The computational results of the overall cooling effectiveness were found to be reasonable agreement with the experimental data. After validation procedure, a shape optimization was developed. The aim is improve the overall cooling effectiveness, along the plate. In the past this was done using different model and different mesh.

In this work this process without re-meshing but just using a morpher algorithm to modify the mesh inside the CFD software, this is RBF-Morph. The parameters modified in the plate in order to have an improvement of the overall cooling effectiveness are three and they are: rotation of the angle, stretch X-pitch, stretch Y-Pitch. Changing in independent way the pitch along x or y direction is done order to find if it exist an optimum with not a distribution of arrays not squared.

---

Then 15 design point were developed using different amplification for this shape modifications, and looking at the variation of the output parameters as function of input parameters, 3 candidate point were chosen for the optimization.

The results show that changing the angle the overall effectiveness has an improvement, event with an opposite flow that gives a better coverage of the plate, also in Y direction the pitch gives better results if decreased, in X direction if increased, but in this last case gives not a significant improvement.

In the end for the better solution among the three candidate points it is shown that this geometry gives an improvement because allow to use lower cool air to have the same overall effectiveness.

# Contents

<b>1</b>	<b>Introduction</b>	<b>1</b>
1.1	Combustion Chamber . . . . .	1
1.1.1	Combustors . . . . .	1
1.1.2	Combustion Chamber Geometry . . . . .	2
1.1.3	Mass flow transient . . . . .	4
1.1.4	Typical Combustor Arrangements . . . . .	5
1.2	Materials . . . . .	11
1.3	Combustor Design Considerations . . . . .	13
1.4	Effusion Cooling . . . . .	14
1.4.1	Experimental and numerical consideration . . . . .	15
1.4.2	Design consideration . . . . .	16
1.4.3	State of the Art . . . . .	17
<b>2</b>	<b>Approach and tools used</b>	<b>24</b>
2.1	Computational fluid dynamics . . . . .	24
2.1.1	Discretization . . . . .	25
2.2	Modelling of turbulence . . . . .	28
2.2.1	Linear eddy viscosity models . . . . .	29

2.2.2	Nonlinear eddy viscosity models . . . . .	34
2.2.3	Reynolds stress model (RSM) . . . . .	34
2.3	SOLIDWORKS . . . . .	36
2.4	ANSYS ICEM . . . . .	38
2.5	ANSYS FLUENT . . . . .	41
2.5.1	CAD Import and Meshing . . . . .	43
2.5.2	Multiphysics . . . . .	43
2.5.3	Calculation procedure for CFD Fluent . . . . .	44
2.6	Morphing with RBF Moph . . . . .	53
2.6.1	Introduction . . . . .	53
2.6.2	RBF Morph . . . . .	55
2.6.3	Conclusion . . . . .	58
2.7	Ansys DesignXplorer . . . . .	60
2.7.1	Parameters . . . . .	60
2.7.2	Design Points . . . . .	61
2.7.3	DesignXplorer Systems . . . . .	62
<b>3</b>	<b>Experimental Data</b>	<b>67</b>
3.1	Experimental Apparatus . . . . .	67
3.2	Effusion Wall Geometries Investigated . . . . .	68
3.3	Experimental Facilities . . . . .	71
<b>4</b>	<b>Mesh and CFD Model</b>	<b>76</b>
4.1	Computational Geometry . . . . .	76

4.2	Mesh . . . . .	76
4.3	CFD Model . . . . .	81
4.3.1	Boundary zones . . . . .	81
4.3.2	Turbulence model . . . . .	82
4.3.3	Radiation model . . . . .	82
4.3.4	Materials . . . . .	82
4.3.5	Boundary condtion . . . . .	83
4.4	Validation . . . . .	87
4.4.1	Mesh sensitivity study . . . . .	87
4.4.2	Effect of turbulence model in refined mesh . . . . .	88
4.5	Baseline Results . . . . .	92
4.5.1	Temperature . . . . .	92
4.5.2	Velocity vectors . . . . .	92
4.5.3	Concentration of tracer . . . . .	93
4.5.4	Overall Effectiveness on the plate . . . . .	94
4.5.5	Pseudo-Adiabatic Effectiveness . . . . .	95
<b>5</b>	<b>RBF-Morph for shape optimization</b>	<b>96</b>
5.1	RBF Morph . . . . .	96
5.1.1	X-Pitch . . . . .	98
5.1.2	Y-Pitch . . . . .	100
5.1.3	Rotation . . . . .	102
<b>6</b>	<b>Workbench and Results</b>	<b>104</b>

6.1	Workbench Implementation . . . . .	104
6.1.1	Design of experiment . . . . .	104
6.1.2	Response Surface . . . . .	105
6.1.3	Optimization . . . . .	108
6.2	Computational Procedure . . . . .	110
6.3	Results . . . . .	112
6.3.1	Average Overall effectiveness . . . . .	114
6.3.2	Maximum Overall effectiveness . . . . .	117
6.3.3	Minimum Overall effectiveness . . . . .	120
6.3.4	Average Adiabatic effectiveness . . . . .	124
6.3.5	Maximum Adiabatic effectiveness . . . . .	127
6.3.6	Sensitivity . . . . .	131
6.3.7	Check Method . . . . .	133
6.3.8	Candidate points . . . . .	134
6.4	Overall effectiveness as a function of G . . . . .	142
<b>List of figures</b>		<b>147</b>
<b>Bibliography</b>		<b>152</b>



# Chapter 1

## Introduction

### 1.1 Combustion Chamber

#### 1.1.1 Combustors

All gas turbine combustors perform the same function; they increase the temperature of the high-pressure gas. Combustor inlet temperature depends on engine pressure ratio, load, engine type, and whether or not the turbine is regenerative or non-regenerative especially at the low-pressure ratios. The new industrial turbine pressure ratios are between 17:1 and 35:1, which means that the combustor inlet temperatures range from 454 °C to 649 °C. The new aircraft engines have pressure ratios that are in excess of 40:1. Regenerative gas turbines have combustor inlet temperatures which range from 371 °C to 593 °C. Combustor exit temperatures range from 927 °C to 1593 °C. Combustor performance is measured by efficiency, the pressure decrease encountered in the combustor, and the evenness of the outlet temperature profile. Combustion efficiency is a measure of combustion completeness. Combustion completeness affects the fuel consumption directly, since the heating value of any un-

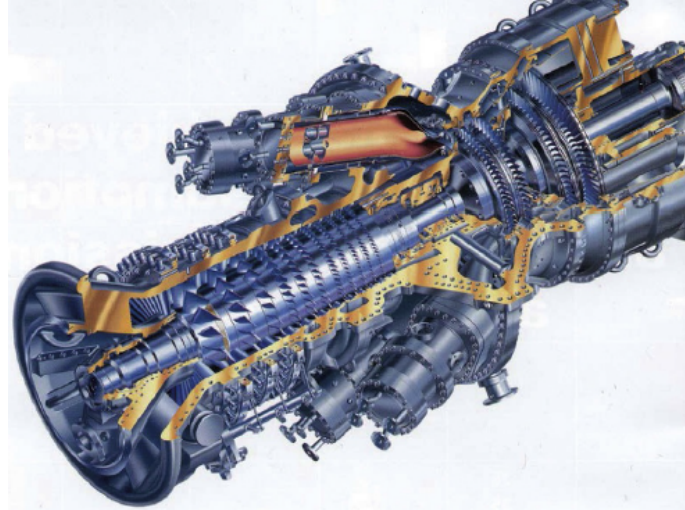


Figure 1.1: A frame-type gas turbine with DLE combustors.

burned fuel is not used to increase the turbine inlet temperature. Normal combustion temperatures range from 1871 °C to 1927 °C. At this temperature, the volume of nitric oxide in the combustion gas is about 0.01%. If the combustion temperature is lowered, the amount of nitric oxide is substantially reduced.

### 1.1.2 Combustion Chamber Geometry

A generic representation of three different types of combustion chambers used in aero- and power generation gas turbine engines is given in Fig.1.2. While the annular (a) and tubular type (b) combustion chambers are used in both aircraft and power generation gas turbines, the single cylindrical type (c) is utilized only in power generation gas turbine engines. All three types, regardless of their size and application field, share the following features: (1) Primary combustion zone, (2) secondary air zone for protecting the combustion

chamber casing against high excessive flame radiation temperature, (3) mixing zone, where the hot gas and the rest of the secondary air are mixed, and (4) the fuel/air inlet nozzle. Since these features are common to the above, almost all of the other types of combustion chambers, a generic module can be designed that entails the above features. Fig.1.3 exhibits such a generic module. Fig.1.3 is a modular representation of a gas turbine combustion chamber. It consists of a primary combustion zone, or primary zone, surrounded by  $n$  rows of segments, the secondary air zone, and the mixing zone. The actual combustion process occurs in the primary zone. The secondary air zone separates the hot primary combustion zone. The rows of segments in the combustion zone are subjected to a severe thermal loading due to direct flame radiation. Film and/or convection cooling on both the air and the gas sides cools these segments. The air required to cool these hot segments flows through

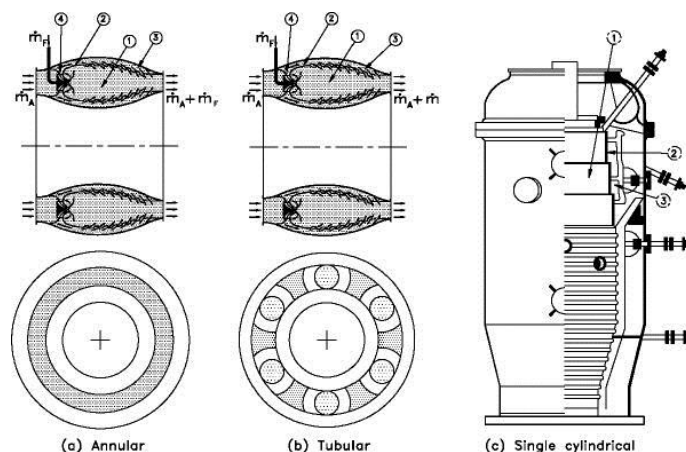


Figure 1.2: Three different types of combustion chambers utilized in aircraft and power generation gas turbines. (a) Annular type, (b) tubular type, (c) heavy duty, single cylindrical power generation (BBC)

finned cooling channels, thereby contributing to the convection cooling of the

segments on the air side. The cooling air flow exiting from the  $j^{th}$  segment row effects the film cooling process on the gas side within the boundary layer in the next row of segments. At the end of that process, the cooling air mass flow is mixed completely with the primary air mass flow. The mass flow relationships prevailing in the primary, the cooling, and the mixing zones are substituted into the energy equation. Their effect is significant, particularly in the case of energy balance, because they determine temperature distribution in the individual combustion chamber stations. For that reason, we first determine the mass flow relationships and then deal with the energy balance.

### 1.1.3 Mass flow transient

The combustion chamber mass flow is divided into primary mass flow, secondary (cooling) mass flow, and mixing mass flow, as shown in Fig.1.3

$$\dot{m}_{S_j} = \mu_j \dot{m}_S = \mu_j \mu_S \dot{m} \tag{1.1.1}$$

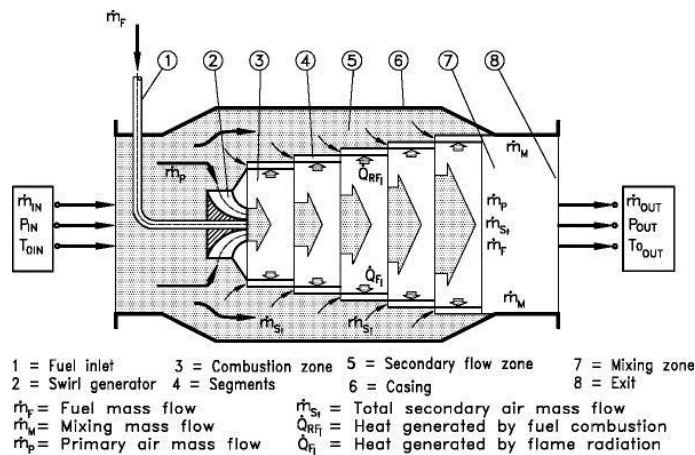


Figure 1.3: Generic modular representation of a combustion chamber

In Eq.1.1.1  $\mu_p$ ,  $\mu_s$ , and  $\mu_M$  denote the primary, secondary, and mixing mass flow ratios, respectively. If the primary zone consists of  $n$  rows of segments, and considering the fuel/air ratio  $\mu_F = \dot{m}_F/\dot{m}$  the cooling mass flow for the  $j^{th}$  row of segments is:

$$\dot{m}_j = \sigma_j \dot{m} = \mu_F + \mu_P + \mu_S \sum_{\nu=1}^j \mu_\nu \quad (1.1.2)$$

To determine the transient behaviour of a combustion chamber that has already been designed, it is necessary to start from the given ratios  $\mu_P$ ,  $\mu_S$ ,  $\mu_M$ ,  $\sigma_j$ . For a new design, it is possible to vary these ratios until the desired solution is attained. The mass flow in the combustion chamber is obtained as the solution to the equation:

$$\frac{\partial \dot{m}}{\partial t} = \frac{R \dot{m}^2 (1 + \mu_F)^2}{\Delta X * S} \left[ \left( \frac{T}{P} \right)_i - \left( \frac{T}{P} \right)_o \right] + \frac{S}{\Delta X} \frac{P_o I - P_o O}{1 + \mu_F} - c_f \frac{\dot{m}^2 (1 + \mu_F)}{2 \rho S D_h} \quad (1.1.3)$$

In Eq.1.1.3, the subscript  $i$  and  $o$  stand for the inlet and outlet plenum respectively. The volume of the combustion chamber is replaced here with an equivalent volume, a constant cross section  $S$  and length  $\Delta X$ . Thus, the pressures and temperatures in Eq.1.1.3 represent inlet and outlet quantities, which must be known at the design point.

### 1.1.4 Typical Combustor Arrangements

There are different methods to arrange combustors on a gas turbine. Designs fall into four categories:

- Can-annular
- Annular
- Silo-type combustor
- External (experimental).

**Can-annular** In aircraft applications where frontal area is important, either can-annular or annular designs are used to produce favorable radial and circumferential profiles because of the great number of fuel nozzles employed. The annular design is especially popular in new aircraft designs; however, the can-annular design is still used because of the developmental difficulties associated with annular designs. Annular combustor popularity increases with higher temperatures or low-BTU gases, since the amount of cooling air required is much less than in can-annular designs due to a much smaller surface area. The amount of cooling air required becomes an important consideration in low-BTU gas applications, since most of the air is used up in the primary zone and little is left for film cooling. Development of a can-annular design requires experiments with only one can, whereas the annular combustor must be treated as a unit and requires much more hardware and compressor flow. Can-annular combustors can be of the straight-through or reverse-flow design. If can-annular cans are used in aircraft, the straight-through design is used, while a reverse-flow design may be used on industrial engines. Annular combustors are almost always straight-through flow designs. Fig.1.1 is a can-annular combustor used on a frame-type turbine and Fig.1.4 is a photograph of a DLN



Figure 1.4: A DLN annular combustor in a Siemens V94.3 Gas Turbine.

**Silo-type combustor** These designs are found on large industrial turbines, especially European designs. Fig.1.5 shows a large frame-type gas turbine with two silo-type side combustors. Smaller side combustors and some small vehicular gas turbines have a combustor as shown in Fig.1.6. They offer the advantages of simplicity of design, ease of maintenance, and long-life due to low heat release rates. These combustors may be of the “straight-through” or “reverse-flow” design. In the reverse-flow design, air enters the annulus between the combustor can and its housing, usually a hot-gas pipe to the turbine. Reverse-flow designs have minimal length.

**External** The author Meherwan Boyce was one of the pioneers of the externally fired steam-injected gas turbine. A 500-kW turbine was developed by Dr. Boyce under a Department of Energy Contract in 1979. The concept was to

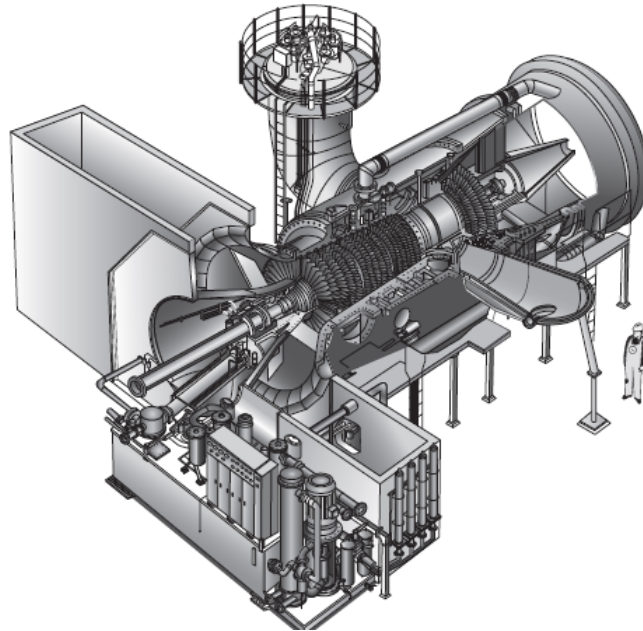


Figure 1.5: A large frame-type gas turbine with two silo-type side combustors

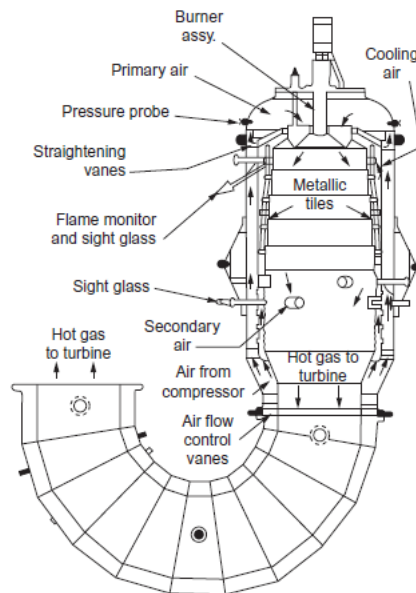


Figure 1.6: A Combustor



develop a turbine that could operate on any type of fuel without reducing the life of the hot section of the gas turbine. The project was developed to burn coal slurry or wood chips that could be combusted in a specially constructed gas turbine combustor. Fig.1.7 shows the combustion on a coal slurry in the externally fired combustor. The combustor used for an external-combustion gas turbine is similar to a direct-fired air combustor. The goals in any combustor are to achieve high temperatures with a minimum pressure decrease of the compressed air and minimal pollution. The combustor consists of a rectangular box with a narrow convection section at the top where steam is produced from the exhaust gas. The outer casings of the combustor consists of carbon steel lined with lightweight blanket material for insulation and heat re-radiation. The inside of the combustor consists of wicket-type coils (inverted “U”) supported from a larger-diameter inlet pipe and a return header running along the two lengths of the combustor. The combustor can have a number of passes for air. The one shown in Figure 1-78 has four passes. Each pass consists of 11 wickets, giving a total of 44 wickets. The wickets are made of different materials, since the temperature increases from about 149–927 C. Thus, the wickets can range from 304 stainless steel to RA330 at the high-temperature ends. The advantage of the wicket design is that the smooth transition of “U” tubes minimizes pressure drops. The Ushaped tubes also allow the wicket to freely expand with thermal stress. This feature eliminates the need for stress relief joints and expansion joints. The wickets are mounted on a rollaway section to facilitate cleaning, repairs, or coil replacement after a long period

of use. A horizontally fired burner is located at one end of the combustor. The flame extends along the central longitudinal axis of the combustor. In this way, the wickets are exposed to the open flame and can be subjected to a maximum rate of radiant heat transfer. The tubes should be sufficiently far away from the flame to prevent hot spots or flame impingement. The air from the gas turbine compressor enters the inlet manifold and is distributed through the first wicket set. A baffle in the inlet prevents the air flow from continuing beyond that wicket set. The air is then transferred to the return header and proceeds further until it encounters a second baffle. This arrangement yields various passes and helps to minimize the pressure drop due to friction. The air is finally returned to the end section of the inlet manifold and exits to the first-stage nozzles of the gas turbine. The combustor was designed for handling preheated combustion air. Preheated combustion air is obtained by diverting part of the exhaust from the gas turbine to the combustor. The air from the turbine is clean, hot air. To recover additional heat energy from the exhaust flue gases, a steam coil is placed in the convection section of the combustor. The steam is used for steam injection into the compressor discharge or to drive a steam turbine. The flue gas temperature exiting from the combustor should be around 316 C and out of the exhaust after passing the steam coils is about 121 C. The initial start up of the externally fired gas turbine was very complex. Unique concepts of start-up for the external gas turbine were developed. The prototype turbine was operated under the DOE contract for over 100 hours.



Figure 1.7: Combustion on cool slurry in the externally fired combustor

## 1.2 Materials

Three major changes have occurred since the original AISI 309 stainless louvercooled liners. The first change was the adoption of better materials such as Hastelloy X/RA333 in the 1960s and Nimonic 75 and the adoption of the slot-cooled liner in the early 1970s. This slot-cooled design offers considerably more liner cooling effectiveness and, from a materials standpoint, presents a new area of processing challenges. Fabrication and repair of liners is primarily by a combination of brazing and welding. On the other hand, earlier liners were made using a welded construction with mechanically formed louvers. For resistance against fatigue, Nimonic 75 has been used with Nimonic 80 and Nimonic 90. Nimonic 75 is an 80–20 nickel–chromium alloy stiffened with a

small amount of titanium carbide. Nimonic 75 has excellent oxidation and corrosion resistance at elevated temperatures, a reasonable creep strength, and good fatigue resistance. In addition, it is easy to press, draw, and mold. As firing temperatures have increased in the newer gas turbine models, HA-188, a Cr, Ni-based alloy, has recently been employed in the latter section of some combustion liners for improved creep rupture strength. Second, in addition to the base material changes, many of today's combustors also have thermal barrier coatings (TBCs), which have an insulation layer of the total thickness 0.4–0.6 mm and are based on  $ZrO_2$ - $Y_2O_3$  and can reduce metal temperatures by 50–150 °C. TBCs consist of two different materials applied to the hot side of the component: a bond coat applied to the surface of the part and an insulating oxide applied over the bond coat. The characteristics of TBCs are that the insulation is porous and they have two layers. The first layer is a bond coat of NiCrAlY and the second is a top coat of Y-TTRIA-stabilized zirconia. The advantages of the TBCs are the reduction of metal temperatures of cooled components, by about 4–9 °C per mil (25.4  $\mu$ m) of the coating, the microstructure, and a coated liner. The primary benefit of the TBCs is to provide an insulating layer that reduces the underlying base material temperature and mitigates the effects of hot streaking or uneven gas temperature distributions. These coatings are now standard on most high-performance gas turbines and have demonstrated excellent performance in production machines. The third major change was the introduction of steam cooling of the liners. This concept, especially in combined-cycle application,

has great potential.

## 1.3 Combustor Design Considerations

**Cross-Sectional Area** The combustor cross section can be determined by dividing the volumetric flow at the combustor inlet by a reference velocity, which has been selected as being appropriate for the particular turbine conditions based on the proven performance in a similar engine. Another basis for selecting a combustor cross section comes from correlations of thermal loading per unit cross section. Thermal loading is proportional to the primary-zone air flow because fuel/air mixtures are near stoichiometric in all combustors.

**Length** Combustor length must be sufficient to provide for flame stabilization, combustion, and mixing with dilution air. The typical value of the length-to-diameter ratio for liners ranges from three to six. Ratios for casing range from two to four.

**Reference Velocity** The theoretical velocity for flow of combustor-inlet air through an area is equal to the maximum cross section of the combustor casing (8 m/s in a reverse-flow combustor and 24–41 m/s in a straight-through flow turbojet combustor).

**Profile Factor** It is defined as the ratio between the maximum exit temperature and the average exit temperature. Temperature factor, also known as the traverse number, can be defined as the peak gas temperature minus mean

gas temperature divided by mean temperature rise in the nozzle design, or the difference between the highest and the average radial temperatures.

**Lower Heating Value** It is the ratio of the oxygen content at stoichiometric and actual conditions:

$$\Phi = \frac{\text{Oxygen/Fuel at stoichiometric condition}}{\text{Oxygen/Fuel at actual condition}} \quad (1.3.1)$$

**Pressure Drop** A pressure loss occurs in a combustor because of diffusion, friction, and momentum. The pressure drop value is 2–10% of the static pressure (compressor outlet pressure). The efficiency of the engine will be reduced by an equal percentage. The minimum practical pressure drop – excluding diffuser loss – is about 14 times higher than the reference velocity pressure. Higher values are frequently used. Some values for this pressure loss are as follows: 30 m/s, 10%; 24 m/s, 2.5%; 21 m/s, 2%; and 15 m/s, 1%.

**Wobbe Number** Wobbe number is an indicator of the characteristics and stability of the combustion process. Increasing the Wobbe number can cause the flame to burn closer to the liner, and decreasing the Wobbe number can cause pulsations in the combustor.

## 1.4 Effusion Cooling

Future aero engines combustion devices will operate with very lean mixtures in the primary combustion zone, switching as much as possible to premixed flames. In this kind of engine the amount of air for the primary zone grows

significantly at the expense of liner cooling air, which thus needs to be reduced. Consequently, important attention must be paid to the appropriate design of the liner cooling system, in order to optimize coolant consumption and guarantee an effective liner protection. An alternative solution to typical cooling system is the full coverage film cooling or effusion cooling, which consists of a large amount of small holes homogeneously distributed over the whole surface of the liner. Although this solution still relies on film cooling generation, it permits to lower the wall temperature reducing the coolant consumption, thanks to heat removal operated by the passage of the coolant through the holes (heat sink effect).

In the open literature, several studies were carried out to understand the thermal behaviour of effusion cooling schemes since the late 60's; many of these have been focused on measuring or estimating the film effectiveness generated by coolant jets.

Effusion cooling of combustor liners for gas turbine engines is quite challenging and necessary to prevent thermal distress of the combustor liner walls. The flow and thermal patterns in the cooling layer are affected by the closely spaced film-cooling holes. It is important to fully document how the film layer behaves with a full-coverage cooling scheme to gain an understanding into surface cooling phenomena.

### **1.4.1 Experimental and numerical consideration**

Temperature inside modern gas turbine combustion chamber can be as high as 2000 K which is too high for most engineering materials. In order to reduce

the wall temperature and improve reliability of the combustion chamber, the wall is protected from hot gases by various cooling methods. Amongst these, effusion cooling is widely used in modern engines because of its simplicity. In this technique, cold air is injected through small holes in the chamber wall which creates a film of cooler fluid and hence acts as a barrier between the wall material and hot gases. The improvement of overall efficiency of gas turbine highly depends on the effectiveness of film cooling.

A considerable amount of research has been conducted by various researchers over the last two decades. Due to the high cost and technical challenges, experimental tests are not usually considered for the entire combustion chamber. Numerical simulations, on the other hand, have become a way to accelerate the design of gas turbine engines and to optimize their performance largely due to the availability of advanced computational fluid dynamics (CFD) software accompanied by computing power.

To reduce the complexity, experimental investigations have been mostly conducted on flat plate with effusion cooling holes in subsonic wind tunnels. It has been found that the effusion film cooling performance can be influenced by aero-thermal conditions as well as by the geometrical design of the film cooled plate surface.

### **1.4.2 Design consideration**

Improved fuel economy, specific power and lower NO<sub>x</sub> emission levels have been the main driving force for the continuing demand for high performance industrial power generation gas turbines.



Increasing the thermal efficiency requires an increase in the turbine entry temperatures (TET), which is limited by the melting temperature of the hot-section components and the cooling effectiveness of these components. The provision of better cooling methods is critical in the design of gas turbine combustor wall and turbine hot-section cooling for higher TET.

However, the gain in efficiency, from the ability to operate at higher turbine inlet temperatures, leads to an overall cycle efficiency gain.

Eventually, the total mass flow of coolant used for effusion cooling will become the limiting factor in reaching the highest cycle thermal efficiency.

For gas turbine combustors, effusion cooling air flow is detrimental to NO<sub>x</sub> emissions, as this is air that has not passed through the combustor primary zone and this makes the primary zone richer and hotter with higher NO<sub>x</sub> emissions.

There are two ways of reducing the coolant mass flow rate: improving the effectiveness of effusion cooling and improving the effectiveness of the overall cooling, which relates to the hole array design and the internal wall cooling. Inclined cylindrical hole injection was introduced to reduce the jet momentum normal to the cooled wall surface, as a means of improving the effusion cooling performance .

### **1.4.3 State of the Art**

In real metal blades and combustor walls, the interaction of the heat exchange between the solid wall and the coolant flow is very important for accurate prediction of the metal temperature as this is not included when the adiabatic

film cooling effectiveness is measured alone. The heat transfer in the wall changes the coolant jet exit density ratio (DR) from that based on the plenum supply conditions. One of the earliest experimental studies of effusion cooling on a conjugate heat transfer basis was reported by Esgar. He found that for the hot-gas and coolant air supply temperatures of 1800 K and 811 K, respectively, the temperature rise of the coolant jet at the exit of the hole was about 250 K. Thus the exiting jet temperature would be 1061 K and the DR would be reduced from 2.2 to 1.7. Similarly, the 1D analytical heat transfer model for a flat plate film cooling presented by Martiny et al. yielded a cooling jet temperature rise of about 12K at the hole exit, for a hot gas and coolant air supply temperature of 600K and 300K, respectively. Thus, the DR was reduced from 2 to 1.9.

Also, Martiny et al. reported that about 60% of the total heat flux to the hot wall surface was absorbed by the coolant as it passed through the hole, leaving only 40% to be absorbed by the backside convection heat flux. It was shown that the overall cooling effectiveness increased as the Biot number (Bi) in the cooling hole, or the backside of the wall, increased. Finally, the model showed that the variation of the injection angle at a fixed wall thickness led to lower cooling effectiveness as the injection angle increased.

Crawford et al. studied the heat transfer performance over the turbulent boundary layer of a normal and inclined flat effusion film cooling wall. They found a lower jet penetration, and hence better adiabatic cooling effectiveness, for the inclined effusion wall than for the normal wall.

Andrews and his co-workers have extensively investigated experimentally the effusion film cooling on a conjugate heat transfer basis for practical gas turbine wall cooling configurations. Their experimental designs were for combustor liner effusion cooling and for impingement/effusion cooling, but their results have application to turbine blade cooling as the required hole geometries are similar. Their results are also one of the very few experimental data sets on effusion film cooling that has active heat transfer in the wall and hence can be used to validate conjugate heat transfer modelling of effusion cooling, which was the purpose of the present work.

Andrews et al. and Lin et al. investigated the effects of the injection flow directions to the mainstream on the cooling performance of an effusion wall. They found that the opposed flow coolant injection had better film cooling performance for the upstream region of the wall than for the co-flow injection wall design. This was because up to a critical blowing ratio the opposed flow caused a reverse flow of the coolant jet and forced it to cover more of the surface to be cooled. However, inclined holes only reduce the of the jet normal to the crossflow by a relatively small margin, 50% for 30°holes and 66% for 20°holes, which is at the limit of manufacturing capabilities. Reducing the pressure loss across the hole by simply making it bigger, offers much greater reductions in the film cooling effectiveness than inclined holes. This was first shown for effusion cooling by Andrews et al. who showed that varying the effusion hole square array  $X/D$  at constant with  $D$  as the variable, gave major improvements in the overall cooling effectiveness as the  $X/D$  was reduced from

11 to 1.9.

However, larger holes reduce the pressure loss and the coolant mass flow has to be controlled by an upstream restrictor, which is the impingement wall in impingement/effusion cooling. A reduction in  $X/D$  by a factor of 2 reduces the blowing ratio  $M$  by a factor of 4 which is greater than can be achieved at constant  $X/D$  using inclined holes. However, for constant mass flow the pressure loss is reduced by a factor of 16 and coolant air mass flow control must involve an upstream higher pressure loss and it is advantageous for the overall heat transfer if an impingement wall is used with the main pressure loss.

Andrews et al. showed that these low  $X/D$  effusion cooling results had a better overall cooling effectiveness than for inclined  $30^\circ$  holes with an  $X/D$  of 11. This was the reason for the present work studying  $90^\circ$  effusion holes at a low  $X/D$  of 4.66.

Yavuzkurt et al. measured the turbulence and velocity profiles over an effusion film cooling flat plate. They found that the turbulence kinetic energy level within the boundary layer decreases with an increase in blowing ratio ( $M$ ) due to the low velocity gradients at high  $M$ . The flow field of effusion film cooling jets was investigated by Scrittore et al.

They demonstrated that sparsely spaced effusion cooling holes had a unique scalable velocity profile. Harrington et al. investigated the effects of the mainstream turbulence on the effusion film cooling performance. Short normal injection holes, similar to those employed by Andrews and his co-workers, were

used in their studies. They found that high mainstream turbulence reduced the film cooling performance more at low blowing ratios than at high blowing ratios with jet lift-off.

Fric et al. presented flow visualization data which revealed the interaction and structure of the cooling jets in the crossflow. They found that the cooling jets coverage on the hot wall surface was higher for a blowing ratio less than 1.7 and greater than 3.3. The minimum coolant jet coverage was observed for the blowing ratios ranging from 1.7 – 3.3.

Gustafsson et al., Ceccherine et al. and Facchini et al. investigated the thermal performance of a cooled effusion flat wall. The generic findings from these studies were that increases in the coolant mass flow rate had a very small effect on the surface temperature distributions of the cooled effusion wall. The gradient of these surface temperature distributions was found to be very small. This was also found in the earlier work of Andrews and co-workers who showed that the increase in overall cooling effectiveness with increased mass flow was small once the effusion jets had lifted off the wall and were generating a stirred boundary layer. For attached effusion jets there was a strong influence of coolant mass flow rate on improved cooling effectiveness.

Jeromin et al. calculated the heat transfer coefficient of an effusion wall with a staggered holes array. The numerical results of their heat transfer coefficients demonstrated a good match with the experimental data for low blowing ratios.

Andrews et al. investigated the effects of the number of holes per square me-

tre surface area,  $N$ , on the overall cooling effectiveness of effusion cooled metal walls. They showed that the cooling performance increased with increasing the number of effusion holes per unit surface area at constant  $X/D$ . This data set is one of the very few experimental data for the validation of conjugate heat transfer modelling in metal walls of the overall cooling effectiveness. Amongst the other metal wall effusion cooled data, is that from the authors who showed that metal wall surface temperature gradients were very low, in contrast to adiabatic cooling effectiveness with its strong axial gradients. This is the basis of the work of Andrews et al. who used discrete thermocouples, brazed flush with the metal hot gas surface, to measure the wall surface temperature in the midspan region between the effusion holes as a function of the distance from the start of the effusion hole arrays. The need to accurately quantify cooling performance of real metal blades and combustor walls has led to a renewed interest in conjugate heat transfer studies by several gas turbine film cooling workers.

In recent years, several alternative injection hole designs have been proposed for gas turbine film-cooling. One of these alternative film-cooling hole geometries is inclined cylindrical holes embedded in a trench outlet.

Bunker investigated discrete holes embedded in a transverse trench, motivated by previous work by Wang et al., which reported a uniform velocity distribution at the outlet of the trench fed with discrete coolant holes.

Waye and Bogard experimentally investigated the effects of different trench hole outlet configurations on the effusion cooling performance. It was shown

that the narrow trenched configuration provided the best effusion cooling performance. The key process of the trench effusion cooling is that the vertical velocity of the jet was reduced as the jet impinged on the vertical trench wall at the trailing edge of the holes. This process converts the three-dimensional impinging jets into a two-dimensional slot jet with much lower slot outlet jet momentum than for the original effusion cooling hole without a trench outlet. This trench effusion cooling configuration was further improved with a shaped trench trailing edge outlet and the authors, for a single row of inclined effusion cooling holes, have suggested a new trench outlet configuration that was predicted to improve the trench effusion cooling performance.

# Chapter 2

## Approach and tools used

**Procedure:** The following procedure was implemented:

- Geometry was created with **Solidworks CAD 3D**
- Structured mesh was developed with **Ansys Icem CFD Mesh Generator**
- CFD model and simulations were done with **Ansys Fluent**
- Goal Driven multi-objective shape optimization is developed in **Ansys Workbench**

### 2.1 Computational fluid dynamics

Computational fluid dynamics, usually abbreviated as CFD, is a branch of fluid mechanics that uses numerical methods and algorithms to solve and analyze problems that involve fluid flows. Computers are used to perform the calculations required to simulate the interaction of liquids and gases with surfaces defined by boundary conditions. With high-speed supercomputers, better



solutions can be achieved. Ongoing research yields software that improves the accuracy and speed of complex simulation scenarios such as transonic or turbulent flows. Initial validation of such software is performed using a wind tunnel with the final validation coming in full-scale testing, e.g. flight tests.

The fundamental basis of almost all CFD problems are the Navier–Stokes equations, which define any single-phase fluid flow:

$$\rho \frac{D\vec{u}}{Dt} = -\nabla p + \rho f - \frac{2}{3} \nabla \cdot [(\mu \nabla \cdot \vec{u}) \tilde{I} + 2 \nabla \cdot (\mu \tilde{E})] \quad (2.1.1)$$

These equations can be simplified by removing terms describing viscosity to yield the Euler equations. Further simplification, by removing terms describing vorticity yields the full potential equations. Finally, these equations can be linearized to yield the linearized potential equations.

### 2.1.1 Discretization

The stability of the chosen discretization is generally established numerically rather than analytically as with simple linear problems. Special care must also be taken to ensure that the discretization handles discontinuous solutions gracefully. The Euler equations and Navier–Stokes equations both admit shocks, and contact surfaces. Some of the discretization methods being used are:

#### Finite volume method

The finite volume method (FVM) is a common approach used in CFD codes. The governing equations are solved over discrete control volumes.

Finite volume methods recast the governing partial differential equations (typically the Navier-Stokes equations) in a conservative form, and then discretize new equation. This guarantees the conservation of fluxes through a particular control volume. The finite volume equation yields governing equations in the form:

$$\frac{\delta}{\delta t} \iiint \mathbf{Q} \delta V + \iint \mathbf{F} \delta A = 0 \quad (2.1.2)$$

where  $\mathbf{Q}$  is the vector of conserved variables,  $\mathbf{F}$  is the vector of fluxes (see Euler equations or Navier–Stokes equations),  $V$  is the volume of the control volume element, and  $A$  is the surface area of the control volume element.

### Finite element method

The finite element method (FEM) is used in structural analysis of solids, but is also applicable to fluids. However, the FEM formulation requires special care to ensure a conservative solution. The FEM formulation has been adapted for use with fluid dynamics governing equations. Although FEM must be carefully formulated to be conservative, it is much more stable than the finite volume approach. However, FEM can require more memory than FVM. In this method, a weighted residual equation is formed:

$$R_i = \iiint W_i Q \delta V^e \quad (2.1.3)$$

where  $R_i$  is the equation residual at an element vertex  $i$ ,  $Q$  is the conservation equation expressed on an element basis,  $W_i$  is the weight factor, and  $V^e$  is the volume of the element.

**Finite difference method**

The finite difference method (FDM) has historical importance and is simple to program. It is currently only used in few specialized codes. Modern finite difference codes make use of an embedded boundary for handling complex geometries, making these codes highly efficient and accurate. Other ways to handle geometries include use of overlapping grids, where the solution is interpolated across each grid.

$$\frac{\delta \mathbf{Q}}{\delta t} + \frac{\delta F}{\delta x} + \frac{\delta G}{\delta y} + \frac{\delta H}{\delta z} = 0 \quad (2.1.4)$$

where  $\mathbf{Q}$  is the vector of conserved variables, and  $F$ ,  $G$ , and  $H$  are the fluxes in the  $x$ ,  $y$ , and  $z$  directions respectively.

**Spectral element method**

Spectral element method is a finite element type method. It requires the mathematical problem (the partial differential equation) to be casted in a weak formulation. This is typically done by multiplying the differential equation by an arbitrary test function and integrating over the whole domain. Purely mathematically, the test functions are completely arbitrary, they belong to an infinitely dimensional function space. Clearly an infinitely dimensional function space cannot be represented on a discrete spectral element mesh. And this is where the spectral element discretization begins. The most crucial thing is the choice of interpolating and testing functions. In a standard, low order FEM in 2D, for quadrilateral elements the most typical choice is the bilinear

test or interpolating function of the form:

$$v(x, y) = ax + by + cxy + d \quad (2.1.5)$$

In a spectral element method however, the interpolating and test functions are chosen to be polynomials of a very high order (typically e.g. of the 10th order in CFD applications). This guarantees the rapid convergence of the method. Furthermore, very efficient integration procedures must be used, since the number of integrations to be performed in a numerical codes is big. Thus, high order Gauss integration quadratures are employed, since they achieve the highest accuracy with the smallest number of computations to be carried out. At the time there are some academic CFD codes based on the spectral element method and some more are currently under development, since the new time-stepping schemes arise in the scientific world.

## 2.2 Modelling of turbulence

The objective of the turbulence models for the RANS equations is to compute the Reynolds stresses, which can be done by three main categories of RANS-based turbulence models:

- Linear eddy viscosity models
- Nonlinear eddy viscosity models
- Reynolds stress model (RSM)

### 2.2.1 Linear eddy viscosity models

These are turbulence models in which the Reynolds stresses, as obtained from a Reynolds averaging of the Navier-Stokes equations, are modelled by a linear constitutive relationship with the mean flow straining field, as:

$$-\rho\langle u_i u_j \rangle = 2\mu_t S_{ij} - \frac{2}{3}\rho k \delta_{ij} \quad (2.2.1)$$

where

- $\mu_t$  is the coefficient termed turbulence "viscosity" (also called the eddy viscosity)
- $k = \frac{1}{2} (\langle u_1 u_1 \rangle + \langle u_2 u_2 \rangle + \langle u_3 u_3 \rangle)$  is the mean turbulent kinetic energy
- $S_{ij} = \frac{1}{2} \left[ \frac{\partial U_i}{\partial x_j} + \frac{\partial U_j}{\partial x_i} \right] - \frac{1}{3} \frac{\partial U_k}{\partial x_k} \delta_{ij}$  is the mean strain rate.

This linear relationship is also known as the Boussinesq hypothesis. For a deep discussion on this linear constitutive relationship, check section Introduction to turbulence/Reynolds averaged equations. There are several subcategories for the linear eddy-viscosity models, depending on the number of (transport) equations solved for to compute the eddy viscosity coefficient.

- Algebraic models : Algebraic turbulence models or zero-equation turbulence models are models that do not require the solution of any additional equations, and are calculated directly from the flow variables. As a consequence, zero equation models may not be able to properly account for history effects on the turbulence, such as convection and diffusion of turbulent energy. These models are often too simple for use in general

situations, but can be quite useful for simpler flow geometries or in start-up situations (e.g. the initial phases of a computation in which a more complicated model may have difficulties). The two most well known zero equation models are the Baldwin-Lomax model and the Cebeci-Smith model.

- One equation models: One equation turbulence models solve one turbulent transport equation, usually the turbulent kinetic energy. The original one-equation model is Prandtl's one-equation model. Other common one-equation models are: Baldwin-Barth model, the Spalart-Allmaras model, and the Rahman-Agarwal-Siikonen Model.
- Two equation models.

Two equation turbulence models are one of the most common type of turbulence models. Models like the k-epsilon model and the k-omega model have become industry standard models and are commonly used for most types of engineering problems. Two equation turbulence models are also very much still an active area of research and new refined two-equation models are still being developed. By definition, two equation models include two extra transport equations to represent the turbulent properties of the flow. This allows a two equation model to account for history effects like convection and diffusion of turbulent energy. Most often one of the transported variables is the turbulent kinetic energy,  $k$ . The second transported variable varies depending on what type of two-equation model it is. Common choices are the turbulent dissipation,  $\epsilon$ , or the specific dissipation,  $\omega$ . The second variable

can be thought of as the variable that determines the scale of the turbulence (length-scale or time-scale), whereas the first variable,  $k$ , determines the energy in the turbulence.

The basis for all two equation models is the Boussinesq eddy viscosity assumption, which postulates that the Reynolds stress tensor,  $\tau_{ij}$ , is proportional to the mean strain rate tensor,  $S_{ij}$ , and can be written in the following way:

$$\tau_{ij} = 2\mu_t S_{ij} - \frac{2}{3}\rho k\delta_{ij} \quad (2.2.2)$$

Where  $\mu_t$  is a scalar property called the eddy viscosity which is normally computed from the two transported variables. The last term is included for modelling incompressible flow to ensure that the definition of turbulence kinetic energy is obeyed:

$$k = \frac{\overline{u'_i u'_i}}{2} \quad (2.2.3)$$

The same equation can be written more explicitly as:

$$-\rho\overline{u'_i u'_j} = \mu_t \left( \frac{\partial U_i}{\partial x_j} + \frac{\partial U_j}{\partial x_i} \right) - \frac{2}{3}\rho k\delta_{ij} \quad (2.2.4)$$

**The Boussinesq assumption** is both the strength and the weakness of two equation models. This assumption is a huge simplification which allows one to think of the effect of turbulence on the mean flow in the same way as molecular viscosity affects a laminar flow. The assumption also makes it possible to introduce intuitive scalar turbulence variables like the turbulent energy and dissipation and to relate these variables to even more intuitive variables like turbulence intensity and turbulence length scale. The weakness of the Boussinesq assumption is that it is not in general valid. There is nothing

which says that the Reynolds stress tensor must be proportional to the strain rate tensor. It is true in simple flows like straight boundary layers and wakes, but in complex flows, like flows with strong curvature, or strongly accelerated or decelerated flows the Boussinesq assumption is simply not valid. This gives two equation models inherent problems to predict strongly rotating flows and other flows where curvature effects are significant. Two equation models also often have problems to predict strongly decelerated flows like stagnation flows.

**Near wall treatments:** The structure of turbulent boundary layer exhibits large, compared with the flow in the core region, gradients of velocity and quantities characterising turbulence. See introduction to wall bounded turbulent flows for more detail. In a collocated grid these gradients will be approximated using discretisation procedures which are not suitable for such high variation since they usually assume linear interpolation of values between cell centres. Moreover, the additional quantities appearing in two-equation models require specification of their own boundary conditions that on purely physical grounds cannot be specified a priori. This situation gave rise to a plethora of near-wall treatments. Generally speaking two approaches can be distinguished:

- Low Reynolds number treatment (LRN)
- High Reynolds number treatment (HRN)

LRN integrates every equation up to the viscous sublayer and therefore the first computational cell must have its centroid in  $y^+ \sim 1$ . This results in very fine meshes close to the wall. Additionally, for some models



additional treatment (damping functions) of equations is required to guarantee asymptotic consistency with the turbulent boundary layer behaviour. This often makes the equations stiff and further increases computation time.

HRN also known as wall functions approach relies on log-law velocity profile and therefore the first computational cell must have its centroid in the log-layer. Use of HRN enhances convergence rate and often numerical stability.

Interestingly, none of the current approaches can deal with buffer layer i.e. the layer in which both viscous and Reynolds stresses are significant. The first computational cell should be either in viscous sublayer or in log-layer not in-between. Automatic wall treatments, available in some codes, are an ad hoc solution but the blending techniques employed there are usually arbitrary and though they can achieve the switching between HRN and LRN treatments they cannot be regarded as the correct representation of the buffer layer. There are two possible ways of implementing wall functions in a finite volume code: Additional source term in the momentum equations. Modification of turbulent viscosity in cells adjacent to solid walls. The source term in the first approach is simply the difference between logarithmic and linear interpolation of velocity gradient multiplied by viscosity (the difference between shear stresses). The second approach does not attempt to reproduce the correct velocity gradient. Instead, turbulent viscosity is modified in such a way as to guarantee the correct shear stress.

### 2.2.2 Nonlinear eddy viscosity models

This is class of turbulence models for the RANS equations in which an eddy viscosity coefficient is used to relate the mean turbulence field to the mean velocity field, however in a nonlinear relationship

$$-\rho \langle u_i u_j \rangle = 2 \mu_t \mathcal{F}_{nl} (S_{ij}, \Omega_{ij}, \dots) \quad (2.2.5)$$

where

- $\mathcal{F}_{nl}$  is a nonlinear function possibly dependent on the mean strain and vorticity fields or even other turbulence variable
- $\mu_t$  is the coefficient termed turbulence "viscosity" (also called the eddy viscosity)
- $S_{ij} = \frac{1}{2} \left[ \frac{\partial U_i}{\partial x_j} + \frac{\partial U_j}{\partial x_i} \right] - \frac{1}{3} \frac{\partial U_k}{\partial x_k} \delta_{ij}$  is the mean strain rate
- $\Omega_{ij} = \frac{1}{2} \left[ \frac{\partial U_i}{\partial x_j} - \frac{\partial U_j}{\partial x_i} \right]$  is the mean vorticity

### 2.2.3 Reynolds stress model (RSM)

The Reynold's Stress Models (RSM), also known as the Reynold's Stress Transport (RST) models, are higher level, elaborate turbulence models. The method of closure employed is usually called a Second Order Closure. This modelling approach originates from the work by [Launder (1975)]. In RSM, the eddy viscosity approach has been discarded and the Reynolds stresses are directly computed. The exact Reynolds stress transport equation accounts for the directional effects of the Reynolds stress fields.

The Reynolds stress model involves calculation of the individual Reynolds stresses,  $\overline{\rho u'_i u'_j}$ , using differential transport equations. The individual Reynolds stresses are then used to obtain closure of the Reynolds-averaged momentum equation. The exact transport equations for the transport of the Reynolds stresses,  $\overline{u'_i u'_j}$ , may be written as follows:

$$\begin{aligned} & \frac{\partial}{\partial t} (\overline{\rho u'_i u'_j}) + \frac{\partial}{\partial x_k} (\rho u_k \overline{u'_i u'_j}) = -\frac{\partial}{\partial x_k} \left[ \overline{\rho u'_i u'_j u'_k} + p' (\delta_{kj} \overline{u'_i} + \delta_{ik} \overline{u'_j}) \right] \\ & + \frac{\partial}{\partial x_k} \left[ \mu \frac{\partial}{\partial x_k} (\overline{u'_i u'_j}) \right] - \rho \left( \overline{u'_i u'_k} \frac{\partial u_j}{\partial x_k} + \overline{u'_j u'_k} \frac{\partial u_i}{\partial x_k} \right) - \rho \beta (g_i \overline{u'_j \theta} + g_j \overline{u'_i \theta}) + \\ & + p' \left( \frac{\partial u'_i}{\partial x_j} + \frac{\partial u'_j}{\partial x_i} \right) - 2\mu \overline{\frac{\partial u'_i}{\partial x_k} \frac{\partial u'_j}{\partial x_k}} - 2\rho \Omega_k (\overline{u'_j u'_m} \epsilon_{ikm} + \overline{u'_i u'_m} \epsilon_{jkm}) + S_{user} \end{aligned}$$

or Local Time Derivate +  $C_{ij} = D_{T,ij} + D_{L,ij} + P_{ij} + G_{ij} + \phi_{ij} - \epsilon_{ij} + F_{ij} +$  User-Defined Source Term where  $C_{ij}$  is the Convection-Term,  $D_{T,ij}$  equals the Turbulent Diffusion,  $D_{L,ij}$  stands for the Molecular Diffusion,  $P_{ij}$  is the term for Stress Production,  $G_{ij}$  equals Buoyancy Production,  $\phi_{ij}$  is for the Pressure Strain,  $\epsilon_{ij}$  stands for the Dissipation and  $F_{ij}$  is the Production by System Rotation. Of these terms,  $C_{ij}$ ,  $D_{L,ij}$ ,  $P_{ij}$ , and  $F_{ij}$  do not require modeling. After all,  $D_{T,ij}$ ,  $G_{ij}$ ,  $\phi_{ij}$ , and  $\epsilon_{ij}$  have to be modeled for closing the equations.



## 2.3 SOLIDWORKS

Parameters refer to constraints whose values determine the shape or geometry of the model or assembly. Parameters can be either numeric parameters, such as line lengths or circle diameters, or geometric parameters, such as tangent, parallel, concentric, horizontal or vertical, etc. Numeric parameters can be associated with each other through the use of relations, which allows them to capture design intent.

Design intent is how the creator of the part wants it to respond to changes and updates. For example, you would want the hole at the top of a beverage can to stay at the top surface, regardless of the height or size of the can. SolidWorks allows the user to specify that the hole is a feature on the top surface, and will then honor their design intent no matter what height they later assign to the can.

Features refer to the building blocks of the part. They are the shapes and operations that construct the part. Shape-based features typically begin with a 2D or 3D sketch of shapes such as bosses, holes, slots, etc. This shape is then extruded or cut to add or remove material from the part. Operation-based features are not sketch-based, and include features such as fillets, chamfers,

shells, applying draft to the faces of a part, etc.

Building a model in SolidWorks usually starts with a 2D sketch (although 3D sketches are available for power users). The sketch consists of geometry such as points, lines, arcs, conics (except the hyperbola), and splines. Dimensions are added to the sketch to define the size and location of the geometry. Relations are used to define attributes such as tangency, parallelism, perpendicularity, and concentricity. The parametric nature of SolidWorks means that the dimensions and relations drive the geometry, not the other way around. The dimensions in the sketch can be controlled independently, or by relationships to other parameters inside or outside of the sketch.

In an assembly, the analog to sketch relations are mates. Just as sketch relations define conditions such as tangency, parallelism, and concentricity with respect to sketch geometry, assembly mates define equivalent relations with respect to the individual parts or components, allowing the easy construction of assemblies. SolidWorks also includes additional advanced mating features such as gear and cam follower mates, which allow modeled gear assemblies to accurately reproduce the rotational movement of an actual gear train.

Finally, drawings can be created either from parts or assemblies. Views are automatically generated from the solid model, and notes, dimensions and tolerances can then be easily added to the drawing as needed. The drawing module includes most paper sizes and standards (ANSI, ISO, DIN, GOST, JIS, BSI and SAC).

## 2.4 ANSYS ICEM

ANSYS ICEM CFD is a popular proprietary software package used for CAD and mesh generation. Some open source software includes OpenFOAM, FeatFlow, Open FVM etc. Present discussion is applicable to ANSYS ICEM CFD software.

It can create structured, unstructured, multi-block, and hybrid grids with different cell geometries.

**Geometry** ANSYS ICEM CFD is meant to mesh a geometry already created using other dedicated CAD packages. Therefore, the geometry modelling features are primarily meant to 'clean-up' an imported CAD model. Nevertheless, there are some very powerful geometry creation, editing and repair (manual and automated) tools available in ANSYS ICEM CFD which assist in arriving at the meshing stage quickly. Unlike the concept of volume in tools like GAMBIT, ICEM CFD rather treats a collection of surfaces which encompass a closed region as BODY. Therefore, the typical topological issues encountered in GAMBIT (e.g. face cannot be deleted since it is referenced by higher topology) don't show up here. The emphasis in ICEM CFD to create a mesh is to have a 'water-tight' geometry. It means if there is a source of water inside a region, the water should be contained and not leak out of the BODY. Apart from the regular points, curves, surface creation and editing tools, ANSYS ICEM CFD especially has the capability to do BUILD TOPOLOGY which removes unwanted surfaces and then you can view if there are any 'holes' in the region

of interest for meshing. Existence of holes would mean that the algorithm which generates the mesh would cause the mesh to 'leak out' of the domain. Holes are typically identified through the colour of the curves.

**Meshing Approach** There are often some misunderstandings regarding structured/unstructured mesh, meshing algorithm and solver. A mesh may look like a structured mesh but may/may not have been created using a structured algorithm based tool. For e.g., GAMBIT is an unstructured meshing tool. Therefore, even if it creates a mesh that looks like a structured (single or multi-block) mesh through pain-staking efforts in geometry decomposition, the algorithm employed was still an unstructured one. On top of it, most of the popular CFD tools like, ANSYS FLUENT, ANSYS CFX, Star CCM+, OpenFOAM, etc. are unstructured solvers which can only work on an unstructured mesh even if we provide it with a structured looking mesh created using structured/unstructured algorithm based meshing tools. ANSYS ICEM CFD can generate both structured and unstructured meshes using structured or unstructured algorithms which can be given as inputs to structured as well as unstructured solvers, respectively.

**Structured meshing strategy** While simple ducts can be modelled using a single block, majority of the geometries encountered in real life have to be modelled using multi-block strategies if at all it is possible. The following are the different multi-block strategies available which can be implemented using ANSYS ICEM CFD.

- O-grid
- C-grid
- Quarter O-grid
- H-grid

**Unstructured meshing strategy** Unlike the structured approach for meshing, the unstructured meshing algorithm is more or less an optimization problem, wherein, it is required to fill-in a given space (with curvilinear boundaries) with standard shapes (e.g., triangle, quadrilaterals - 2D; tetrahedrals, hexahedrals, polyhedrals, prisms, pyramids - 3D) which have constraints on their size. The basic algorithms employed for doing unstructured meshing are: Octree (easiest from the user's perspective; robust but least control over the final cell count which is usually the highest) Delaunay (better control over the final cell count but may have sudden jumps in the size of the elements) Advancing front (performs very smooth transition of the element sizes and may result in quite accurate but high cell count)





## 2.5 ANSYS FLUENT

There are huge numbers of engineering applications that can benefit from computational fluid dynamics simulation. Whether are analyzed commonplace fluid flow and heat transfer or work with complex transient reacting flows, Ansys Fluent software should be an integral part of product design and optimization process.

A fully featured fluid dynamics solution for modeling flow and other related physical phenomena, Fluent offers unparalleled analysis capabilities. It provides all the tools needed to design and optimize new equipment and to troubleshoot existing installations. The versatile technology offers insight into how a product design will behave in the real world, all before a single prototype is built.

Fluent's capabilities are developed by world-renowned experts and supported by extremely experienced engineers so you can have confidence in the solution as you develop higher quality products faster, decrease time to market, reduce risk and increase innovation. To provide high productivity, the Ansys

Workbench platform directly couples with any CAD software and automatically extracts and meshes fluid volumes. You control this easy-to-perform operation via a small set of parameters; the yield is the high-quality meshes critical for both accurate and fast CFD simulation.

CFD package includes solvers that accurately simulate behavior of the broad range of flows that engineers encounter daily from Newtonian to non-Newtonian, from single-phase to multi-phase, and from subsonic to hypersonic. Each solver is highly robust, well tested, validated and optimized for fast simulation time. Time tested and part of a single environment, the highly efficient solvers deliver both accuracy and speed. For deeper insight such as making informed decisions about small adjustments that yield large performance improvements you can increase the granularity of the analysis.

Such improved resolution requires more computational resources and parallel computing. Fluent has a record of outstanding parallel scalability, ranging from two processors to thousands, giving you high-fidelity results in the shortest possible time.

Optimizing your product requires evaluating a large number of designs. Capabilities within Ansys Workbench enable efficient, fully automated optimization (or design of experiments) for tens or hundreds of design points; the technology can evaluate many design points concurrently. Workbench makes the process easy by controlling the execution, results data and file management for each set of design point.

### 2.5.1 CAD Import and Meshing

From CAD import to geometry meshing, flexible tools allow to automatically create meshes or hand-craft them.

Ansys meshing can extract fluid volume from a CAD assembly and automatically create tetrahedral or hexahedral meshes with inflation layers.

Ansys also offer advanced repair tools so can import and prep geometry for partly or fully manual meshing.

Ansys pre-processing tools provide the high-quality meshes project needs, so you obtain accurate results. Simulation-Driven Product Development relies on design process compression, using solutions that fully automate your simulation workflow so you can focus on your engineering goals. Advanced simulation workflow and application technologies are key to accelerating processes and gaining the necessary insight into your product so can quickly make the right design decisions

### 2.5.2 Multiphysics

The Ansys portfolio of simulation tools enables to accurately predict real-world, multiphysics behavior of industrial designs.

Phenomena such as flow-induced vibration and material deformation induced by fluid can be readily captured using our multiphysics tools. Ansys provide comprehensive technologies for all physics disciplines: structural mechanics, heat transfer, fluid flow and electromagnetics.

By combining these, it can solve complex industrial engineering challenges

to optimize entire product.

Ansys provides a powerful integrated solution for automating different physics simulations. Data transfer to and from multiple physics eliminates the time required to manually convert output from one stage of work process into input for another.

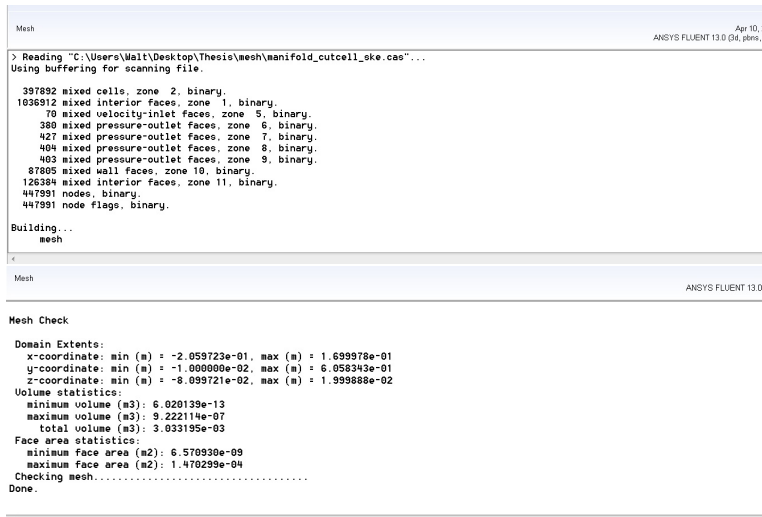
### 2.5.3 Calculation procedure for CFD Fluent

Fluent CFD has a very complex structure, at the base of which there are several mathematical models needed to define the physical properties and flow characteristics of the fluid.

It is essential, before starting any simulation with Fluent software, follow some basic points. The first thing doing after have imported the geometry model developed in any software, it is to check that there are no errors in the grid (e.g. parts of mesh finite element with distorted, negative volume, border zones not defined properly, etc.).

**Check** When Fluent start in the command line shows information regarding: the grid item type, the number of cells, the number of nodes, the minimum and maximum size of the volumes of the elements, the minimum and maximum spatial coordinates of geometric model along the axis x, y, z.

For a better view the other information can also be displayed by the command "General → Check.



```

Mesh
Apr 10, 2012
ANSYS FLUENT 13.0 (64_bits)

> Reading "C:\Users\Matt\Desktop\Thesis\mesh\manifold_cutcell_ske.cae"...
Using buffering for scanning file.

397892 mixed cells, zone 2, binary.
1036912 mixed interior faces, zone 1, binary.
70 mixed velocity-inlet faces, zone 5, binary.
399 mixed pressure-outlet faces, zone 6, binary.
427 mixed pressure-outlet faces, zone 7, binary.
404 mixed pressure-outlet faces, zone 8, binary.
403 mixed pressure-outlet faces, zone 9, binary.
87895 mixed wall faces, zone 10, binary.
126384 mixed interior faces, zone 11, binary.
447991 nodes, binary.
447991 node flags, binary.

Building...
mesh

Mesh
ANSYS FLUENT 13.0

Mesh Check

Domain Extents:
x-coordinate: min (m) = -2.059723e-01, max (m) = 1.699978e-01
y-coordinate: min (m) = -1.000000e-02, max (m) = 6.058243e-01
z-coordinate: min (m) = -6.093721e-02, max (m) = 1.939686e-02
Volume statistics:
minimum volume (m3): 6.020139e-13
maximum volume (m3): 9.222114e-07
total volume (m3): 3.033195e-03
Face area statistics:
minimum face area (m2): 6.570930e-09
maximum face area (m2): 1.470299e-04
Checking mesh.....
Done.

```

Figure 2.1: Fluent window: “Grid” menù

**General setup** In solver panel is possibly choose if the model will Run in Steady or in Transient. If the velocity formulation is Absolute or Relative, and if Solver Type is Pressure-Based or Density-Based

**Viscous Model:** The next step now is to define the type of viscous model for runoff. From the main menu you can do this by selecting “Define” → “Models” → “Viscous”.

Fluent software contains a wide range of viscous models: Inviscid, Laminar Spalart-Allmaras,  $k - \varepsilon$ ,  $k - \omega$ , etc.

In the ”Viscous Model” are also displays the values of the constants in the mathematical equations of viscous model chosen.

It can also determined the type of condition to the wall.

The energy equation could be activated selecting “Define” → “Models” → “Energy”.

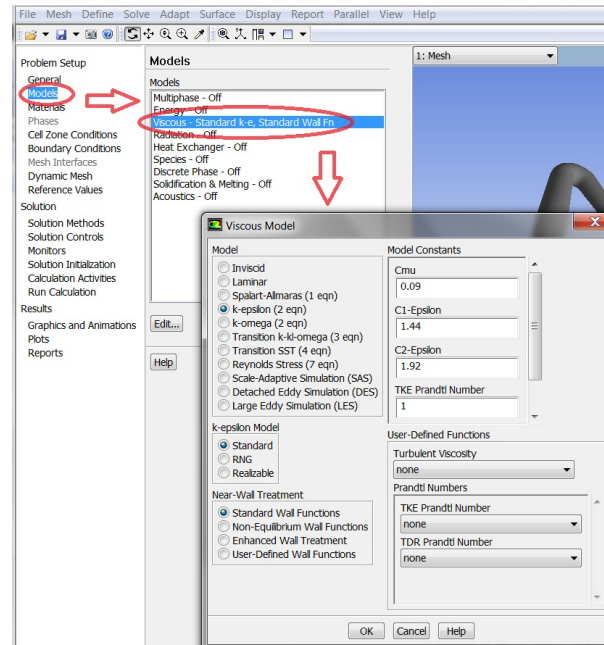


Figure 2.2: Fluent window: Viscous model

Inside the “Define” → “Models” there are many other physical models involving the thermal radiation, heat exchanger, etc.

**Fluid Type** Chosen the viscous model it is necessary to establish the operating fluid type during simulations. It is sufficient in this case select “Define” → “Materials” to define the physical characteristics of the fluid.

**Operative & Boundary Condition** Before moving on to ”Solve” it is necessary to establish operating conditions and the boundary conditions system to simulate.

Operating Condition can be set in “Cell Zone Condition”.

Boundary conditions must be defined for any area, from the “Boundary

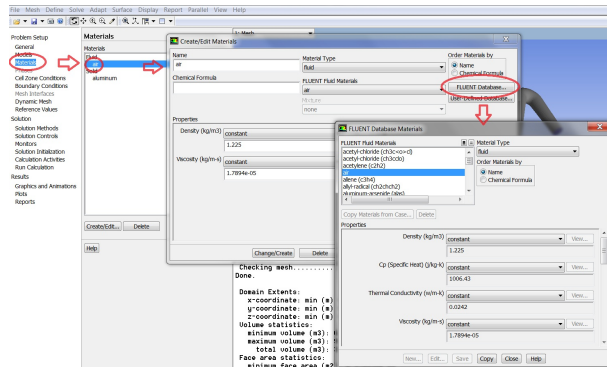
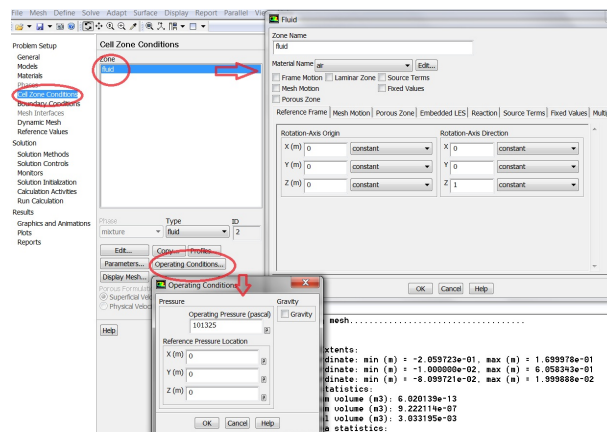


Figure 2.3: Fluent Database Materials

Conditions” you select the area of interest and then the type of boundary condition). In some cases, such as for sections of entry or exit, choose the type of boundary condition, another window opens in which you are prompted more physical variables (eg. speed, temperature, hydraulic diameter section, etc.). The operative condition must be modified only not atmospheric condition case



**Solution Control** The later stage, before moving to iterations, it is to control the parameters present in the mathematical equations of viscous model previously defined. Selecting path “Solution Control” is shown a window

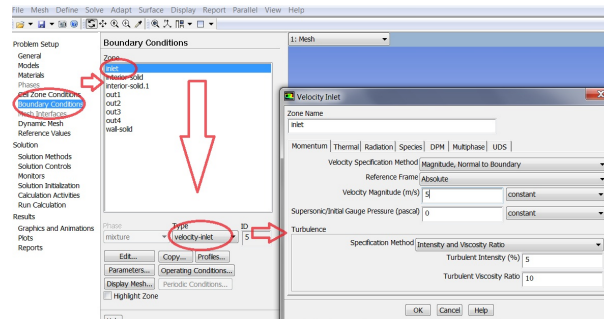


Figure 2.4: Operating Condition & Boundary Condition

that is composed mainly by subwindow: “Explicit Relaxation Factors, Under Relaxation Factors”. By clicking the text “Equation”, there are mathematical formulas that will iterate. The subwindows “Explicit Relaxation Factor” “Under Relaxation Factor” contain values of relax in the formulas of the moment of momentum in the continuity equation, the equation turbulence model, etc. These values should not be changed, usually at least that the simulations diverges, in this circumstance is convenient to reduce to promote convergence.

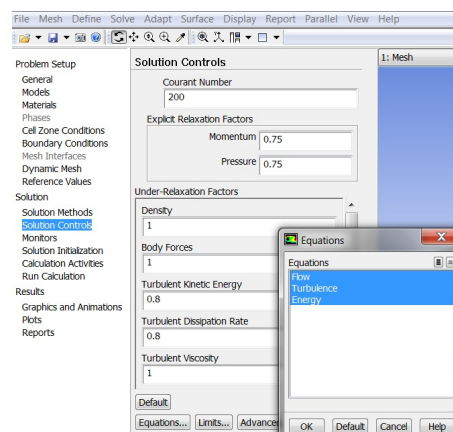


Figure 2.5: Solution Controls



**Solution Method** Selecting patch “Solution Method” it is allowed choosing the control parameters of the discretization solving equations.

In the subwindow “Scheme” is possible set the most appropriate algorithm for coupled equations of speed and pressure. The solver “Simple” is indicated for incompressible fluids or slightly compressible. Type “Coupled” instead is indicated for high speed compressible fluid outflow.

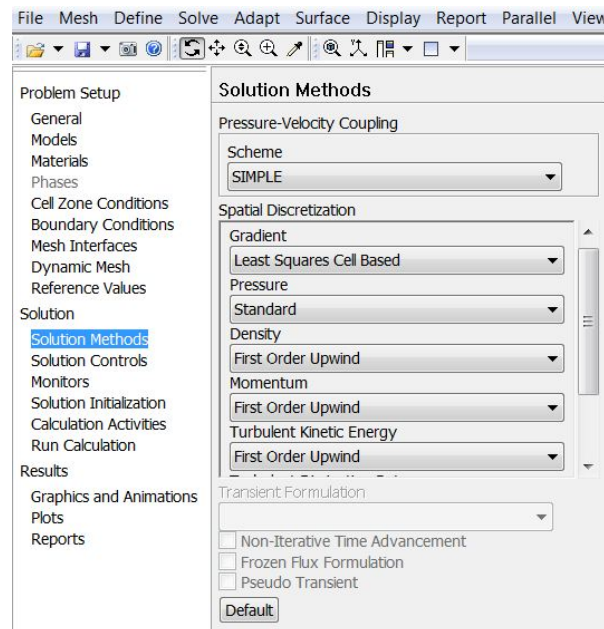


Figure 2.6: Solution Methods

**Monitors** Fluent software also allows to change the values of residue after each iteration.

The command “Solution” → “Monitors” → “Residual” → “Edit” displays the “Residual Monitors” in which values are assigned to the residual equation of

continuity, the components of the speed, the energy equation, coefficient of turbulent kinetic energy  $k$  at the rate of dissipation  $\varepsilon$ . Usually the residual values, except the continuity equation, are on the order of  $10^{-6}$ . The evolution of debris over time, or with each iteration, it can also be displayed on the monitor; to enable this command, select the command is simply “Plot” under “Option” window “Residual Monitors” and indicate the number of the view window under the heading “Plotting Window”

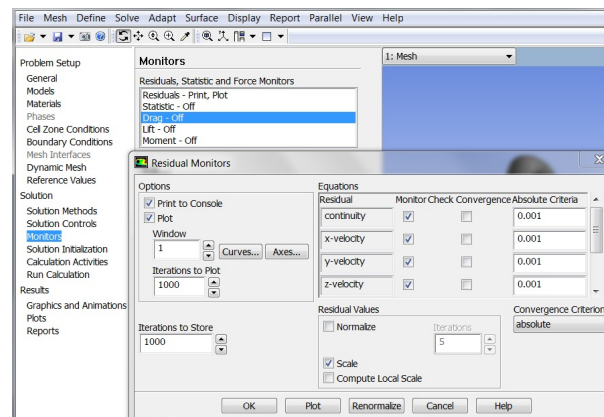


Figure 2.7: Monitors

**Solution Inizialization** Before starting simulation is necessary initialize the flow field in the entire domain. There are two methods to initialize the system. The first is to Hybrid Inizialization; the second defining initial values in some areas. The “Solution Initialization” sets the initial values for variables and initialize the fluid dynamics solution according to these values. They can be entered manually in the invoked by selecting or area of interest under “Compute From” and through the “Initialize” command you can initialize the

system.

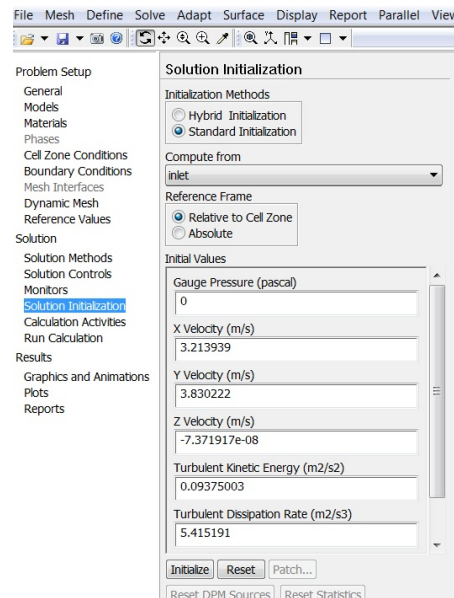


Figure 2.8: Solution Inizialization

**Run Calculation** Once the initialization phase you move to iterations. Through the command "Run Calculation", "Calculate" button is displayed. In the "Calculate" are requested: the number of intervals of time  $\Delta t$  or "time steps", the duration in seconds of each time interval and the maximum number of iterations for "time step".

Always "Calculate" window you can change the number of updates planned for the "UDF (User Defined Function) for each" time step ". Very important is the choice of time interval  $\Delta t$ . The time interval must be small enough so you don't miss any fast transients; usually the time interval must be less than one order of magnitude of time constant used by modelling system. A valid

method choosing the amplitude is based on the number of iterations.

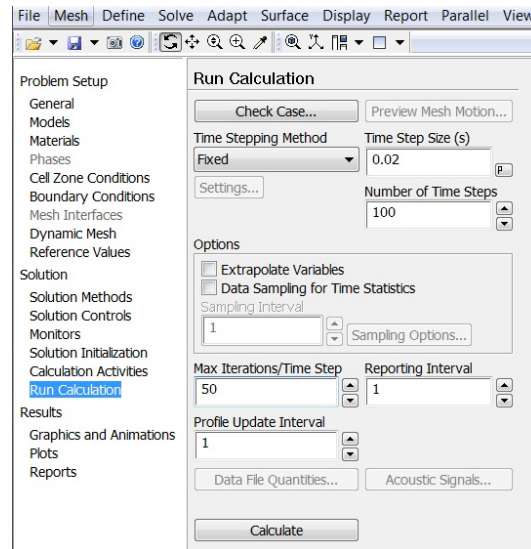


Figure 2.9: Run Calculation

Usually, a proper time interval Solver convergence leads to after about 20 iterations. If the number of iterations is greater need to reduce "time step", if it is less, it is necessary to increase the amplitude of time step".

In the steady flow case the "Calculate" takes a simpler form. In it are required only the number of iterations, the number of intervals to update the display of charts and the number of updates for each iteration of the UDF. The simulation can now be started by clicking the button "iterate" of the respective window. Many other commands in Fluent software can be activated before proceeding to a simulation.



## 2.6 Morphing with RBF Moph

### 2.6.1 Introduction

Morphing is the ability to change one thing into another smoothly. In modern computer graphics 3D character animation uses morphing for several reasons. The movement of characters is usually gained through motion capture techniques while the backbone of the character is considered to be constrained to rigid motions. However the characters are not rigid, with the obvious exclusion of characters representing mannequins or humanoid robots.

Morphing transforms the surfaces of the original model into a new position or shape. In computer graphics however the accuracy of the movement is not important because it just needs to look good. Morphing the mesh required for a numerical simulation is a more complicated and quite a delicate task, especially for a 3D CFD mesh. In this case morphing, also termed smoothing, is not limited to the surface but has to be extended to the entire volume of the mesh and the solver suffers dramatically. Although the concept is

basically the same as morphing in computer graphics, i.e. morphing defines the motion of a set of points and moves them accordingly to the action of a motion field. The way the task is accomplished, depends on which smoothing algorithm is selected and on the definition of the control points criteria which can substantially change the result.

A good morpher is one that preserves the exact shape that the user wants (i.e. it undergoes a rigid motion where there is a steady object and a null rigid motion prescribed) and gently deforms the surface and volume elements that are within the deformation field and minimises the distortion of each element. In general any mesh distortion introduces a reduction in the quality of the mesh, so the morpher is required to minimize this effect, still allowing for significant modification of the shapes.

The presented software is based on a well known technique related to the use of the so called Radial Basis Functions (RBF). The method is based on the use of a system of radial functions to produce a solution for the mesh movement/morphing, from a list of source points and their displacements. This approach is valid for both surface shape changes and volume mesh smoothing. The software allows the user to modify the shape of the surface in a user-friendly way, interacting directly with the graphical representation of the surface and being fully integrated with FLUENT. Then the smoother is capable to reduce the related distortion of the volume mesh and preserve an acceptable mesh quality, which is fundamental for a reliable flow solution. The impact on the CFD process is that, instead of re-generating the mesh, it is possible to specify

several shape modifications (compatible with the mesh topology which cannot be changed) directly in the solving stage inside FLUENT, without the need to step back to the meshing tools and so saving a significant amount of human and CPU time. Moreover the shape changes can be parameterized in order to perform parametric studies of shapes and component positions typical of the fluid dynamics development. Finally the morpher can be coupled with external optimizer tools to perform automatic optimizations.

### **2.6.2 RBF Morph**

RBF Morph is a unique morpher that combines a very accurate control of the geometrical parameters with an extremely fast mesh deformation, fully integrated in the CFD solving process.

RBF Morph is the meeting point between state-of-the-art scientific research and top-level industrial needs. The industrial need was very simple: move an object inside a very large CFD mesh (many millions of cell), preserving the original geometry of the other parts, and preserving the quality of the volume mesh without the need for remeshing, i.e. only by updating the node positions. To complete the specification of such a tool the following extra features were required: working in parallel, handling every kind of volume elements (tetrahedrons, prisms, hexahedrons, polyhedrons, preserving also non conformal interfaces) and working inside ANSYS Fluent with a simple interface.

**The aim**

The aim of RBF Morph is to perform fast mesh morphing using a mesh-independent approach based on the state-of-the-art RBF (Radial Basis Functions) techniques. The use of RBF Morph allows the CFD user to perform shape modifications, compatible with the mesh topology, directly in the solving stage, by just adding one single command line to the input file. The most important requirements are:

- a mesh-independent solution;
- parallel morphing of the grid;
- large size models (many millions of cells) to be morphed in a reasonable short time;
- and management of every kind of mesh element type (tetrahedral, hexahedral, polyhedral, prismatic, hexcore, non-conformal interfaces, etc.).

The final goal is to perform parametric studies of component shapes and positions typical of the fluid-dynamic design such as:

- design developments;
- multi-configuration studies;
- sensitivity studies;
- DOE (Design Of Experiment);
- and optimization.



## Usage Steps

RBF Morph is based on a three-step procedure:

- SERIAL: general setup (definition of the source points);
- SERIAL: solution of the RBF system;
- SERIAL or PARALLEL: morphing of the surface/volume mesh.

The serial setup requires an extensive use of the RBF Morph GUI. The GUI offers all the tools required for the definition of the problem. It is composed by a main panel that, acting on the radio buttons on the left, offers several different operative modes.

**The first** four panels (*Config, Encaps, Surfs, Points*) are addressed to the problem setup and the definition of the source points; *Solve and Multi-Sol* panels allow to calculate or combine the RBF solutions; *Preview and Morph* panels let the user to preview or apply the morphing to the mesh; in the CAD panel is possible to apply the morphing modification to a given STEP CAD file; the *Tools* panel contains various utilities and settings.

After completing **Step 1** it is possible to proceed to **Step 2** and calculate the RBF solution. The effect of the solution (often referred as *modifier or parameter*) can be verified using the Preview feature. It allows to pre-morph on-the-fly an arbitrary number of surfaces, without altering the actual mesh, overlaying them on the current graphical viewport. In alternative, it is also possible to morph the actual mesh, check the result in terms of shape deformation, mesh quality, etc. and then to go back to the original

configuration using the Undo capability. Once that the solution is satisfactory, it can be saved on file. The operation is then repeated for each desired modifier.

**Step 3** can be performed in serial or in parallel with or without the GUI. Once the solutions are available, they can be loaded and used to morph the mesh using the *Morph* panel of the GUI or using TUI commands that allow to prescribe a single morph, a multi-morph or a sequential morph, combining the effect of multiple modifiers. Given that each modifier can be applied with the desired magnitude (*Amplification*), a parametric FLUENT model results.

### 2.6.3 Conclusion

In this chapter RBF theory has been presented showing how these methods can be used for a very efficient solution of one of the most challenging application in the field of CFD: mesh morphing and smoothing of very large models. The complete research path from the industrial need to a software solution has been discussed. The RBF based approach for mesh morphing and smoothing has proven to have one of the best performances of any techniques in this field. The main reason is that it combines several advantages that are individually the key strength of the other methods: mesh quality preservation, the ability to handle very complex free form shape modifications, the ability to exactly prescribe rigid movement, element type independence, parallelism and reusability on different meshes.

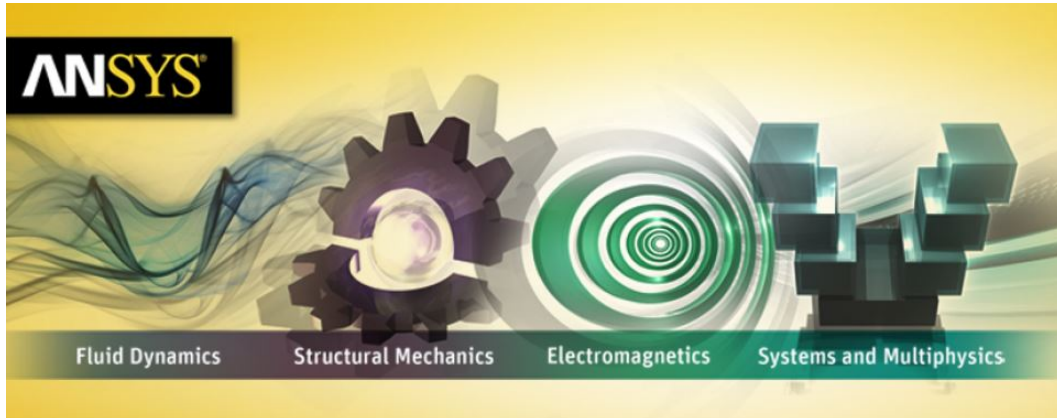
The importance of a high quality and very fast mesh morpher in CAE is clear and the benefit that comes from its application strongly relates to the size of the problem. For small problems, where a rebuild of the mesh is not an

issue, the main advantages are

- the simplicity of the geometry parameterization;
- the flexibility that make it good to use for multi-physics problems

These advantages are linked to the ease of synchronization of different calculation models to the same geometry. For medium sized models, where the CAD to model automation is still possible, an extra benefit comes from saving calculation time in rebuilding the mesh. For large problems where this automation is not feasible the benefits are very high:

- a "what if" analysis can be performed with minimum effort for the set-up (hours vs days are required for the rebuild of a new model);
- a parametric analysis (for the shape optimization or for the set-up of an investigation with adjustable parts) that with the traditional approach is limited to a small number of solutions.



## 2.7 Ansys DesignXplorer

### 2.7.1 Parameters

The following types of parameters are used in DesignXplorer:

- Input Parameters;
- Output Parameters .

Input parameters are those parameters that define the inputs to the analysis for the model under investigation. Input parameters have predefined ranges which can be changed. These include (and are not limited to) CAD parameters, Analysis parameters, DesignModeler parameters and Mesh parameters. CAD and DesignModeler input parameters may include length, radius, etc.; Analysis input parameters may include pressure, material properties, materials, sheet thickness, etc.; Mesh parameters may include relevance, number of prism layers or mesh size on an entity.

Input parameters can be discrete or continuous, and each of these have specific forms.

Discrete parameters physically represent different configurations or states of the model. An example is the number of holes in a geometry. Discrete parameters allow you to analyze different design variations in the same parametric study without having to create multiple models for parallel parametric analysis.

Continuous parameters physically vary in a continuous manner between a lower and an upper bound defined by the user. Examples are CAD dimension or load magnitude. Continuous parameters allow you to analyze a continuous value within a defined range, with each parameter representing a direction in the design and treated as a continuous function in the DOE and Response Surface.

Output parameters are those parameters that result from the geometry or are the response outputs from the analysis. These include (and are not limited to) volume, mass, frequency, stress, heat flux, number of elements, and so forth.

### **2.7.2 Design Points**

A design point is defined by a snapshot of parameter values where output parameter values were calculated directly by a project update. Design points are created by design exploration; for instance, when processing a Design of Experiments or a Correlation Matrix, or refining a Response Surface. It is also possible to insert a design point at the project level from an optimization candidate design, in order to perform a validation update. Note that the output parameter values are not copied to the created design point since they were

calculated by design exploration and are, by definition, approximated. Actual output parameters will be calculated from the design point input parameters when a project update is done.

### **2.7.3 DesignXplorer Systems**

The following DesignXplorer systems are available:

- Parameters Correlation System;
- Response Surface System;
- Goal Driven Optimization System.

#### **Parameters Correlation System**

You can use the Parameters Correlation system to identify the major input parameters. This is achieved by analyzing their correlation and the relative weight of the input parameters for each output parameter. Indeed, when your project has many input parameters (more than 10 or 15), building an accurate response surface becomes an expensive process. So it is recommended to identify the major input parameters with the Parameters Correlation feature in order to disable the minor input parameters when building the response surface. With less input parameters, the response surface will be more accurate and less expensive to build.

#### **Response Surface System**

The Response Surfaces are functions of different nature where the output parameters are described in terms of the input parameters. They are built

from the Design of Experiments in order to provide quickly the approximated values of the output parameters, everywhere in the analyzed design space, without having to perform a complete solution. The accuracy of a response surface depends on several factors: complexity of the variations of the solution, number of points in the original Design of Experiments and choice of the response surface type.

The Response Surface provides four types of chart allowing the exploration of the design space by graphically viewing the impact that parameters have on one another:

- Response chart: a graphical representation that allows you to see how changes to each input parameter affect a selected output parameter ;
- Local Sensitivity chart: is a powerful project-level tool, allowing you see at a glance the impact of all the input parameters on output parameters. For each output, it allows you to see the weight of the different input; it calculates the change of the output based on the change of each input independently, at the current value of each input parameter in the project
- Local Sensitivity curves chart: helps you to further focus your analysis by allowing you to view independent parameter variations within the standard Local Sensitivity chart. It provides a means of viewing the impact of each input on specific outputs, given the current values of other parameters. This multi-curve chart provides a means of viewing the impact of each input parameter on specific outputs, given the current values of the other parameters. The Local Sensitivities Curves chart

shows individual local sensitivities, with a separate curve to represent the impact of each input on one or two outputs;

- Spider chart: allows you to visualize the impact that changing the input parameter(s) has on all of the output parameters simultaneously .

### **Goal Driven Optimization System**

DesignXplorer offers two different types of Goal Driven Optimization systems: Response Surface Optimization and Direct Optimization. A Response Surface Optimization system draws its information from its own Response Surface component, and so is dependent on the quality of the response surface. The available optimization methods (Screening, MOGA, NLPQL, and MISQP) utilize response surface evaluations, rather than real solves. A Direct Optimization system is a single-component system which utilizes real solves. When used in a Direct Optimization context, the available optimization methods (Screening, , NLPQL, MISQP, Adaptive Single-Objective, and Adaptive Multiple-Objective) utilize real solves, rather than response surface evaluations. A Direct Optimization system does not have an associated Response Surface component, but can draw its information from any other system or component that contains design point data. It is possible to reuse existing design point data, reducing the time needed for the optimization, without altering the source of the design points. For example:

- You can transfer design point data from an existing Response Surface Optimization and improve upon the optimization without actually changing



the original response surface.

- You can use information from a Response Surface that has been refined with the Kriging method and validated. You can transfer the design point data to a Direct Optimization system and then adjust the quality of the original response surface without affecting the attached direct optimization.
- You can transfer information from any DesignXplorer system or component containing design point data that has already been updated, saving time and resources by reusing existing, up-to-date data rather than reprocessing it.

In the Goal Driven Optimization System three charts are available to analyze the results:

- Tradeoff chart: the Tradeoff chart is a 2D or 3D scatter chart representing the generated samples. In the Tradeoff chart, the samples are ranked by non-dominated Pareto fronts, and you can view the tradeoffs that most interest you. To make sense of the true nature of the tradeoffs, the plots must be viewed with the output parameters as the axes. This approach shows which goals can be achieved and whether this entails sacrificing the goal attainment of other outputs. Typically, a Tradeoff chart shows you a choice of possible, non-dominated solutions from which to choose.
- Samples chart: the aim of this chart is to provide a multidimensional graphical representation of the parameter space you are studying. The

chart uses the parallel Y axes to represent all of the inputs and outputs. Each sample is displayed as a group of line curves where each point is the value of one input or output parameter. The color of the curve identifies the Pareto front that the sample belongs to, or the chart can be set so that the curves display the best candidates and all other samples. Compared to the Tradeoff chart, the Samples chart has the advantage of showing all the parameters at once, whereas the Tradeoff chart can only show three parameters at a time. The Samples chart is better for exploring the parameter space. The Samples chart is a powerful exploration tool because of its interactivity. With the Samples chart axis sliders, you can filter for each parameter very easily, providing an intuitive way to explore the alternative designs. Samples are dynamically hidden if they fall outside of the bounds. Repeating the same operation with each axis allows you to manually explore and find trade-offs.

- Sensitivities chart: shows the global sensitivities of the output parameters with respect to the input parameters.

# Chapter 3

## Experimental Data

### 3.1 Experimental Apparatus

Full coverage effusion cooling was studied for a square array of 90°effusion cooling holes with backside cooling using a 5 mm duct air supply to the coolant holes. Active cooling was used with metal walls and 300K effusion cooling into a 27 m/s mean velocity duct flow at 770K crossflow temperature. The 152 mm square test section had 10 rows of holes and the hole diameter,  $D = 3.27$ , and hole pitch  $X=15.2$ . The  $X/D$  values studied was 4.6.

At a constant coolant mass flow rate the wall pressure loss was reduced as  $X/D$  was reduced and there was an associated reduction in the film blowing ratio,  $M$ . The duct air feed to the holes enhanced the backside cooling of the wall. In the experiment were tested other wall, with different ratio  $X/D$ , hole pitch  $X$  was varied for constant hole diameter  $D$ , and viceversa.

The decrease in  $X/D$  was the most effective way of increasing the overall cooling effectiveness as this reduced the blowing rate without decreasing the coolant mass flow rate. This was more effective than using 30°inclined holes

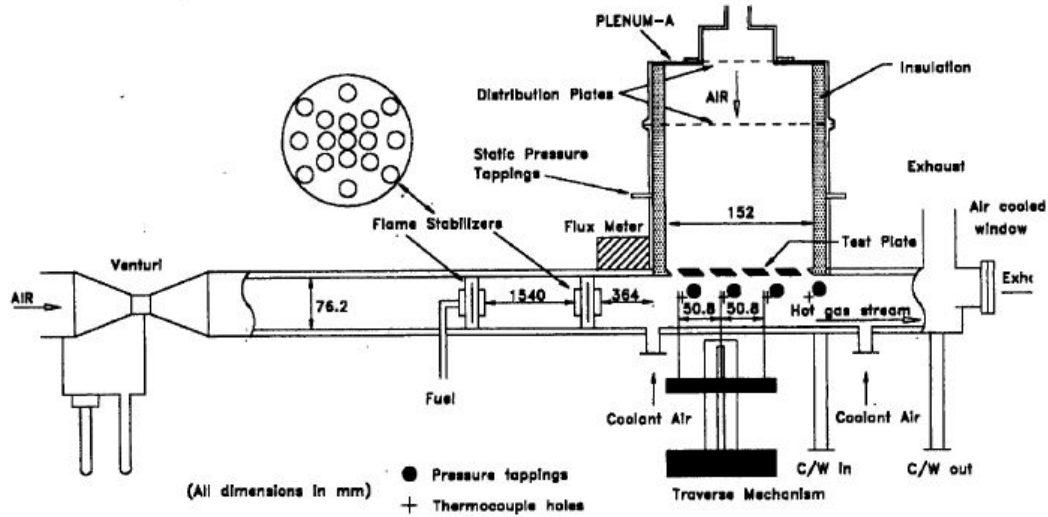


Figure 3.1: Experimental Apparatus

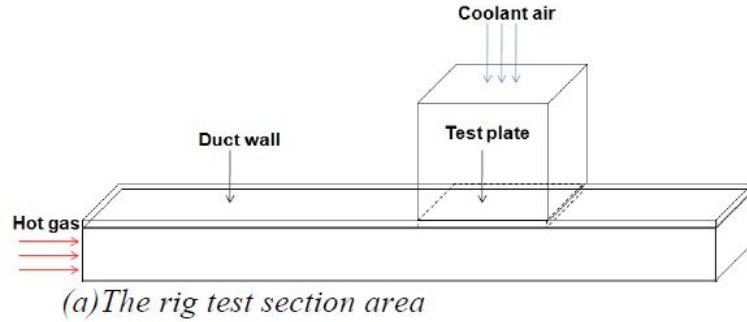
with an  $X/D = 11$ , as the hole exit velocity was much lower for the same coolant mass flow rate with  $90^\circ$  holes at an  $X/D = 4.6$  than with  $30^\circ$  holes at an  $X/D = 11.0$

## 3.2 Effusion Wall Geometries Investigated

The effusion wall designs investigated in this study had a square array of normal injection holes with an exposed squared surface area of  $152 \times 152$  mm. The injection holes length,  $L$ , was 6.35 mm for all the wall designs. The key design variable investigated had a  $10 \times 10$  square array of holes with a total of number of holes per square metre surface area,  $N=4306$  holes/ $m^2$ , as shown in Fig.3.2. The blowing ratio  $M$ , is given as a function of the mass flow per surface area,  $G$ , by

$$M = \frac{1.27G(X/D)^2}{\rho_g u_g} \quad (3.2.1)$$

The overall effectiveness  $\eta_{ov}$  is given by equation:



\* - Embedded thermocouples    o - Film cooling holes

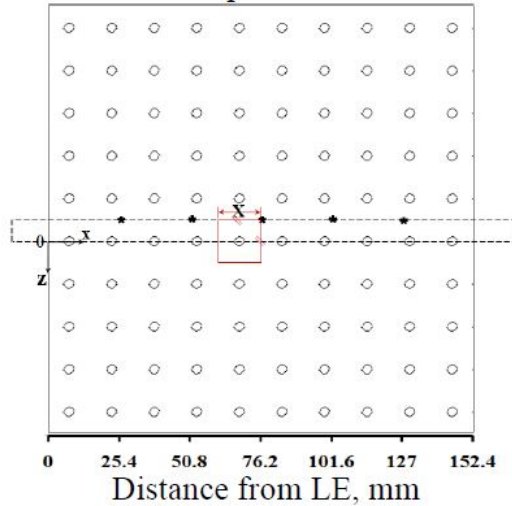


Figure 3.2: Computational Apparatus

$$\eta_{ov} = \frac{T_g - t_w}{T_g - T_c} \tag{3.2.2}$$

where  $T_g$  is the temperature of the hot gas,  $T_c$  is the temperature of the cooling air,  $T_w$  is the measured metal temperature from the imbedded thermocouples shown in Fig.3.2. These were located on the centreline between the effusion holes and thus were at the hottest part of the metal wall. This was done

so that the measured cooling effectiveness data would be conservative. The experimental data was applied directly by the industrial sponsors in the design of effusion cooling walls and hence needed to be conservative.

The hottest part of the metal wall would be the part to fail first and hence the determination of the hottest wall temperature was important in the experimental work. The experimental uncertainty in the determination of  $\eta_{ov}$  was mainly due to the measurement of  $T_g$  as  $T_c$  was close to ambient and the imbedded metal temperature  $T_w$  a steady temperature. The hot gas temperature was measured by a bare bead thermocouple mounted 50mm away from the centre of the test wall.

There was no correction made for radiation losses and it was considered that at the 27 m/s crossflow velocity the convective gain was high and the radiative loss was low, as none of the walls were water cooled.

However, the error was significant, but it was considered that a suction pyrometer would be too bulky and the gas suction would interfere with the duct aerodynamics. Precedent equation is a ratio involving the temperature difference from the gas temperature and the error was largely cancelled out.

However,  $T_g$  would always be low due to the radiant heat losses to the cooler walls.

Calculations of the worst case heat losses and the convection heat gain from the hot crossflow using a cylinder in a crossflow heat transfer, gives the maximum error in  $T_g = 20\text{ }^\circ\text{C}$  which gives a maximum underestimation of  $\eta_{ov}$  of 0.02 at the highest coolant flow rate, which gives the highest temperature difference

and thus the greatest radiation losses from the thermocouple. Thus the measurements should be just below the predictions, especially at high  $G$ . The error in the flow rate determination for  $G$  was 2% as calibrated variable area flow meters were used referenced against a standard orifice flow meter.

### **3.3 Experimental Facilities**

The experimental flat effusion walls that were modelled were made from Nimonic-75. The experimental test rigs consisted of an insulated coolant air plenum chamber mounted in the top wall of the 76mm deep by 152.4 mm wide duct, as shown schematically in Fig.3.1.

The test plates, with an array of equispaced lateral and streamwise hole pitch,  $X$ , formed the bottom part of the plenum chamber which was bolted to the plenum chamber. Internally, the plenum chamber was insulated to prevent heat loss from the coolant to the plenum wall.

Imbedded thermocouples, located with the thermocouple junction on the hot gas side and flush with the surface, were used in the experiments to determine the overall cooling effectiveness. These were located on the centreline between the rows of effusion hole, which is the worst case location. Surface averaged overall cooling effectiveness were not directly measured, but it was assumed that internal wall conduction would effectively locally average the heat transfer. This occurs at low Biot numbers which was the case in the experimental work. The choice of the worst case location in the experiments for the measuring thermocouple was to ensure that the resultant overall cooling effectiveness

was conservative, as the results were to be directly applied in gas turbine combustor design.

These experimental results are predicted to be close to the centreline worst case measurements, which was the assumption used in the original experimental work. The thermocouples were located at 25.4, 51.8, 76.2, 101.6 and 127mm from the leading edge.

These locations were kept fixed for all the experimental test walls, so that comparison could be made for effusion cooling where  $N$  was a variable but the length of metal to be cooled was fixed. This enables comparison between different designs at the same axial location from the leading edge. The imbedded thermocouples were located relative to the nearest coolant holes

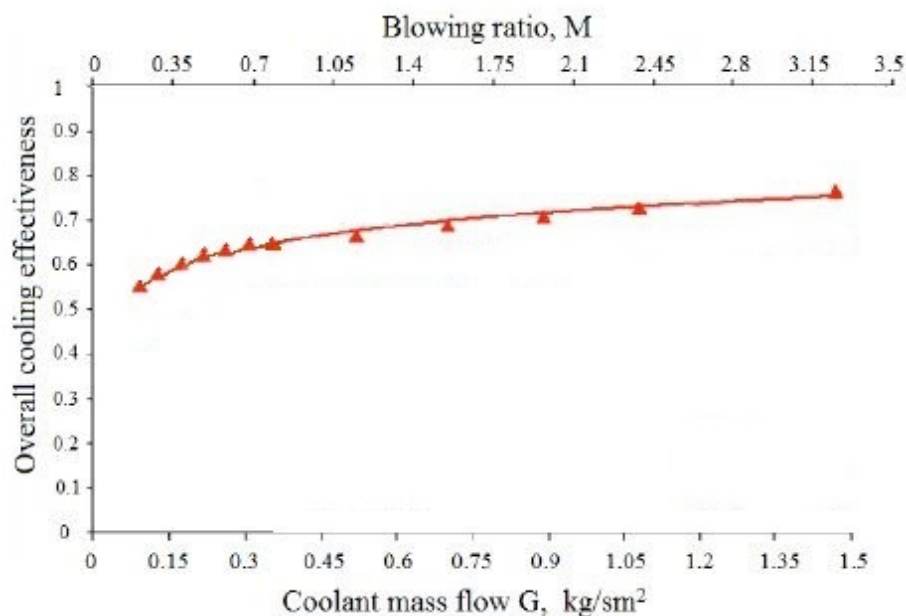


Figure 3.3: Area averaged cooling effectiveness as a function of  $G$  at the last thermocouple



in a different way for each thermocouple, as shown in Fig.3.2. Only at the 76mm position is the thermocouple in the centre of the four hole square array of effusion holes.

In addition to presenting the experimental thermocouple positions, the surface averaged overall and adiabatic cooling effectiveness predictions are presented. For each hole, the  $X^2$  surface area (i.e. the lateral and streamwise pitch are the same and equal to  $X$ ) predictions are averaged so that the mean surface area-average of the cooling effectiveness as a function of coolant mass flow rate can be showed. Also the ninth hole position surface average cooling effectiveness is used to show the dependence of the fully developed average effusion cooling effectiveness as a function of the coolant mass flow rate,  $G$ .

The hot gas crossflow passed through a grid 45 mm upstream of the start of effusion cooling test. The hot gas flow duct was 76 x 152mm cross section and had air cooled stainless steel walls. The air coolant flow for the duct walls was varied to achieve the same duct wall temperature as for the centre of the effusion test wall. This used a thermocouple mounted in the duct wall opposite the centre of the test section.

The hot gas temperature was generated using an upstream natural gas combustor, which was operated very lean in order to generate the desired hot gas temperature. This was mounted upstream of a turbulence generating grid plate. This had a combustor flow pressure loss of 3% and hence generated high turbulence in the crossflow, similar to that existing in a combustor.

The dimensionless temperatures of the hot gas adjacent to the test plate

surface was related to the local adiabatic cooling effectiveness and this was measured by traversing a bare bead thermocouple positioned at the centre of the duct. The traversing thermocouple had a low voltage electric circuit that would indicate contact of the thermocouple with the test wall.

The traverse thermocouple stepper motor was then moved slightly to break the contact with the test plate and the gas temperature at that point was recorded.

The spatial location of the thermocouple was not precise, due to differential thermal expansion of the test wall and duct, and this uncertainty in position is about  $+/- 1mm$ . It is important to note that this thermocouple does not measure the conventional adiabatic cooling effectiveness, which in this work is predicted using a scalar gas tracer.

However, it does measure a temperature close to the wall which was compared with the CFD predictions of the temperature at that location.

This temperature was non-dimensionalised and is referred to as a "pseudo-adiabatic cooling effectiveness".

The Biot number was less than 0.1 for the investigated flow conditions. This is representative of combustor wall cooling applications. The original data was aimed at a design procedure for combustor effusion cooling and for impingement/effusion cooling and has been in use for several years by industry. However, the wall conduction is similar for turbine blades as the alloys used have similar thermal conductivities to that of Nimonic 75.

One of the weaknesses in these data sets for CFD validation is that the

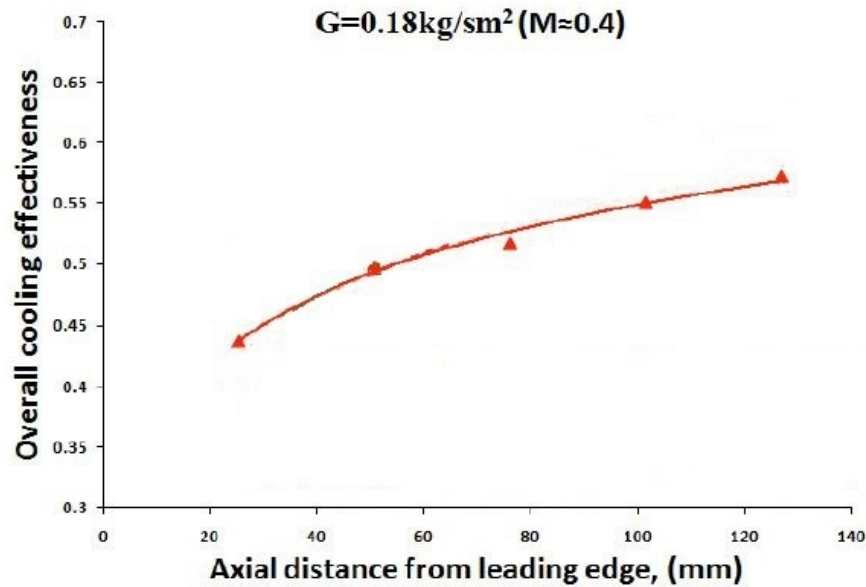


Figure 3.4: Variation of  $\eta_{ov}$  with axial distance from LE of the wall for  $G=0.18 \text{ kg/sm}^2$

turbulence level of the mainstream and coolant was not measured, but a real combustor was used to generate the hot-gas mainstream. Therefore, a turbulence intensity level of 10% was assumed for the crossflow in the CFD predictions.

# Chapter 4

## Mesh and CFD Model

### 4.1 Computational Geometry

The computational geometry was created with the CAD software Dessault Systemes Solidworks according to the experimental apparatus described in Chapter 3. Due to symmetry of the geometry, the computational domain is only half pitch ( $X/2$ ) between the centerline of the holes arrows, and it is 7.62 mm thick ( $X=15.4\text{mm}$ ).

The geometry consist of a structure is composed with a hot duct 791 mm long, 76.2 mm high orizontal hot duct with injection of cold air at 300 mm from the inlet. The coolant air flows through 10 holes, with diameter  $D=3.27\text{mm}$ , from a 152.4mm x 6.35mm vertical duct.

### 4.2 Mesh

The computational domain was discretised with a multiblock structured mesh Generated with Ansys Icem. Grid generation is of extreme importance in CFD, and can be defined as the process of breaking the physical domain into

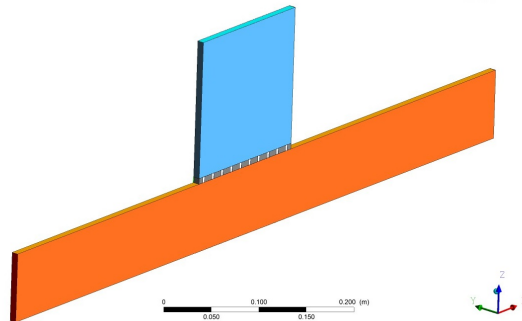


Figure 4.1: Base Geometry

small discrete sub-domains, in order to calculate numerical partial differential equations on a discrete number of points.

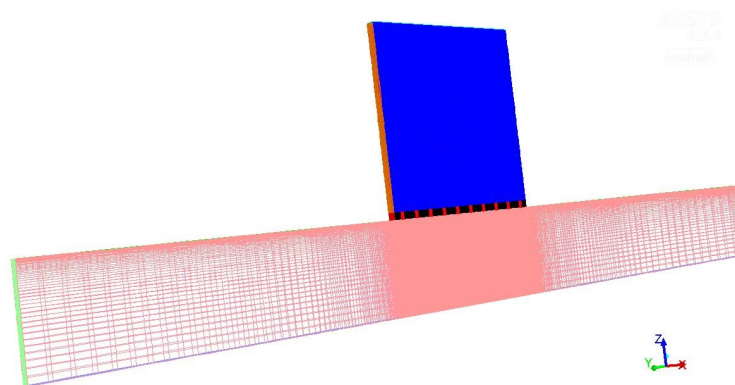


Figure 4.2: Mesh

There are several general advantages to using a structured grid:

- Time and memory. You can fill the same volume with fewer hexes than tets, thereby lowering the cell count and your CFD computation time and memory usage. Structured grids generally have a different topology than unstructured grids, so it is difficult to make a direct cell count comparison. At its simplest, each hexahedron can be decomposed into 5

tetrahedra that share its edges, giving a 5:1 reduction in cell count for the same flowfield resolution. The benefit to reducing cell count becomes very apparent when generating a mesh with a wide variation in resolved length scales; you will use many more tets than you would hexes.

- **Resolution.** Flow of a fluid will often exhibit strong gradients in one direction with milder gradients in the transverse directions (e.g. boundary layers, shear layers, wakes). In these instances, high quality cells are easily generated on a hex grid with high aspect ratio (on the order of one thousand or more). It is much more difficult to generate accurate CFD solutions on highly stretched tetrahedra. (Plus, not all stretched tets are equal depending on the maximum included angles.)
- **Alignment.** CFD solvers converge better and can produce more accurate results when the grid is aligned with the predominant flow direction. Alignment in a structured grid is achieved almost implicitly because grid lines follow the contours of the geometry (as does the flow), whereas there's no such alignment in an unstructured mesh.
- **Definable normals.** Application of boundary conditions and turbulence models work well when there is a well-defined computational direction normal to a feature such as a wall or wake. Transverse normals are easily defined in a structured grid.

First mesh generated with Icem had following features:

- 664594 Cells

- 2058907 Faces
- 729388 Nodes.

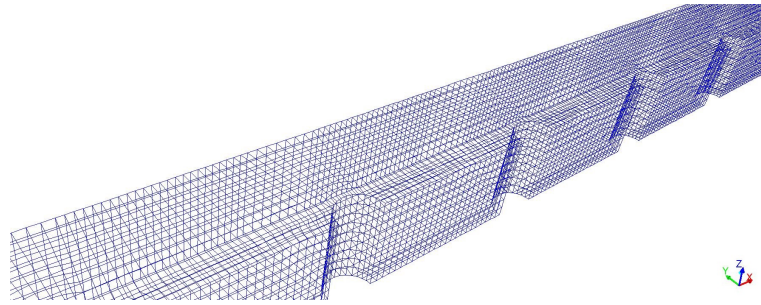


Figure 4.3: Mesh Detail

After a preliminary run in Fluent, this mesh was refined, in order to improve the results in boundary layer. Three layers of cells were split near the plate inside the holes, obtaining a final mesh made of:

- 926870 Cells
- 2912539 Faces
- 1058156 Nodes.

Fig.4.4 and Fig.4.5 show the two meshes near the cooling holes.

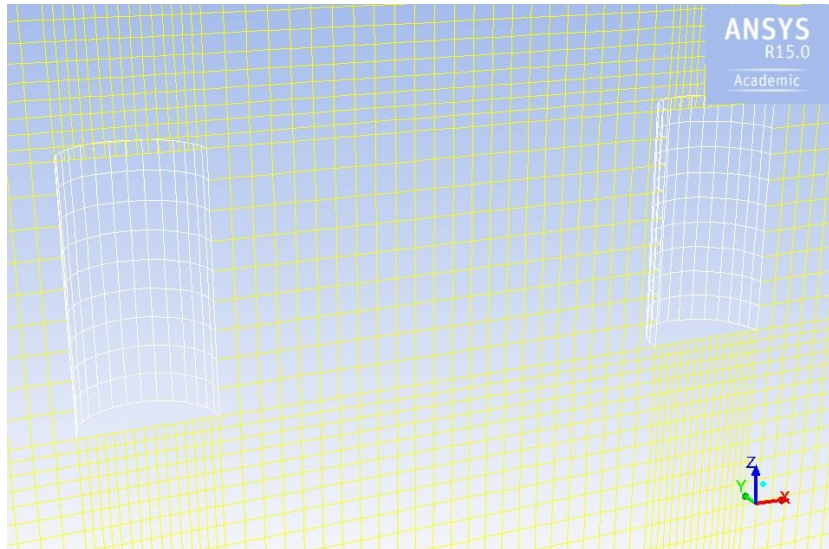


Figure 4.4: Start Mesh

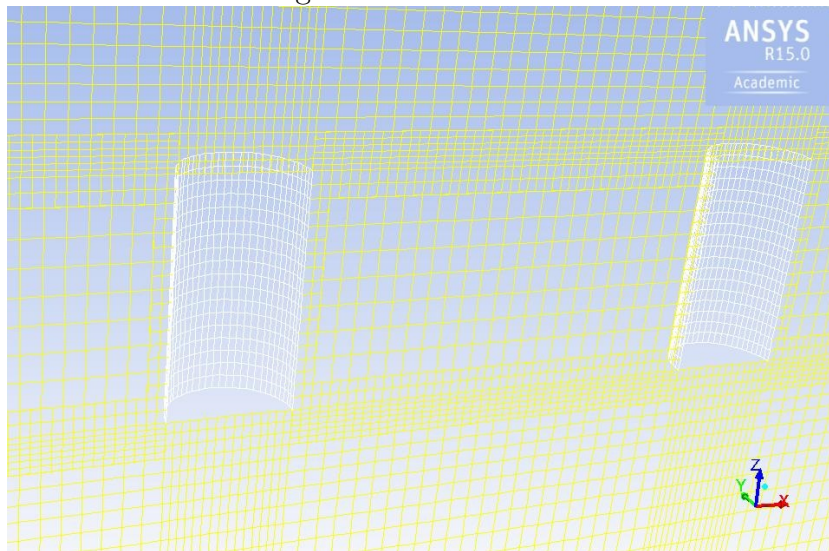


Figure 4.5: Refined Mesh



## 4.3 CFD Model

### 4.3.1 Boundary zones

The geometry is divided into surfaces:

- Inlet cold
- Inlet Hot
- Outlet Hot
- Holes
- Symmetry surfaces
- Wall surfaces

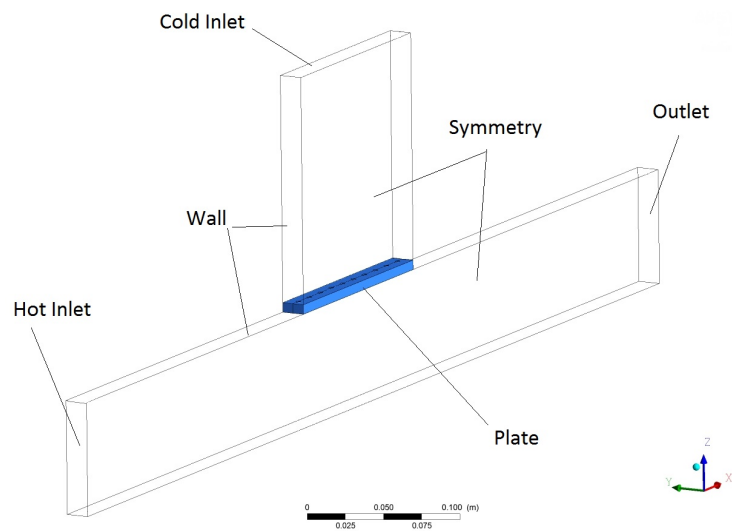


Figure 4.6: CFD Geometry

### 4.3.2 Turbulence model

Several Viscous Model were used for the validation:

- Standard  $k - \epsilon$
- Standard  $k - \omega$
- Realizable  $k - \epsilon$
- SST  $k - \omega$

### 4.3.3 Radiation model

Discrete ordinates (DO) Radiation model was used with 10 energy iteration per radiation iteration, Angular Discretizations Theta divisions=3, Phi divisions=3, Theta pixels=3, Phi Pixels=3.

### 4.3.4 Materials

Materials considered were air for the fluid, and Nimonic 75 for the plate (according with experimental apparatus). The main air properties are:

- Density= $1.225\text{kg}/\text{m}^3$
- Cp (specific Heat)= $1006.43\text{ J}/\text{kgK}$
- Thermal conductivity= $0.0242\text{W}/\text{mK}$

NIMONIC alloy 75 is an 80/20 nickel-chromium alloy with controlled additions of titanium and carbon. First introduced in the 1940s for turbine blades

in the prototype Whittle jet engines, it is now mostly used for sheet applications calling for oxidation and scaling resistance coupled with medium strength at high operating temperatures. It is still used in gas turbine engineering and also for industrial thermal processing, furnace components and heat-treatment equipment. It is readily fabricated and welded. It has the following properties:

- Density= $8370\text{kg}/\text{m}^3$
- Cp (specific Heat)= $461\text{ J}/\text{kgK}$
- Thermal conductivity= $11.2\text{ W}/\text{mK}$

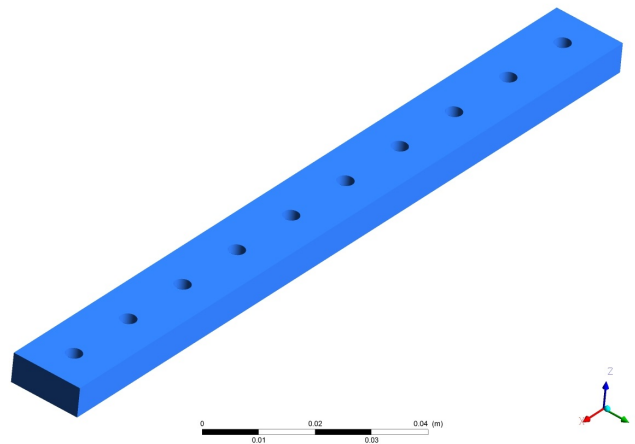


Figure 4.7: Plate detail

### 4.3.5 Boundary condtion

**Inlet cold** A mass flow inlet was imposed on the coolan tream inlet with the following properties:

- Mass Flux  $G=0.18\text{kg}/\text{sm}^2$

- Temperature  $T=300$  K
- Gauge Pressure  $P=0$  Pa
- Turbulence Intensity= 5 %
- Turbulence Viscosity Ratio=10%

Mass flow boundary conditions can be used in FLUENT to provide a prescribed mass flow rate or mass flux distribution at an inlet. Physically, specifying the mass flux permits the total pressure to vary in response to the interior solution. This is in contrast to the pressure inlet boundary condition, where the total pressure is fixed while the mass flux varies.

A mass flow inlet is often used when it is more important to match a prescribed mass flow rate than to match the total pressure of the inflow stream. An example is the case of a small cooling jet that is bled into the main flow at a fixed mass flow rate, while the velocity of the main flow is governed primarily by a (different) pressure inlet/outlet boundary condition pair.

**Inlet Hot** VELOCITY INLET condition was imposed to inlet hot with Velocity Normal To boundary:

- Velocity  $v = 27m/s$
- Temperature  $T=770$  K
- Gauge Pressure  $P=0$  Pa
- Turbulence Intensity= 10 %
- Turbulence Viscosity Ratio=10%

Velocity inlet boundary conditions are used to define the flow velocity, along with all relevant scalar properties of the flow, at flow inlets. The total (or stagnation) properties of the flow are not fixed, so they will rise to whatever value is necessary to provide the prescribed velocity distribution.

**Outlet Hot** A pressure outlet condition was imposed on the outlet, assuming:

- Temperature  $T=770$  K
- Gauge Pressure  $P=0$  Pa
- Turbulence Intensity= 10 %
- Turbulence Viscosity Ratio=10%

Pressure outlet boundary conditions require the specification of a static (gauge) pressure at the outlet boundary. The value of the specified static pressure is used only while the flow is subsonic. Should the flow become

locally supersonic, the specified pressure will no longer be used; pressure will be extrapolated from the flow in the interior. All other flow quantities are extrapolated from the interior.

**Wall surfaces** A no slip shear condition was assumed for all the wall of the domain.

Wall boundary conditions are used to bound fluid and solid regions. In viscous flows, the no-slip boundary condition is enforced at walls by default, but you can specify a tangential velocity component in terms of the translational or rotational motion of the wall boundary, or model a "slip" wall by specifying shear.

**Symmetry surfaces** A symmetry boundary condition was imposed on all the surfaces on ZX plane, because the cfd model is only a slice of the entire model.

Symmetry boundary conditions are used when the physical geometry of interest, and the expected pattern of the flow/thermal solution, have mirror symmetry. They can also be used to model zero-shear slip walls in viscous flows. This section describes the treatment of the flow at symmetry planes and provides examples of the use of symmetry. You do not define any boundary conditions at symmetry boundaries, but you must take care to correctly define your symmetry boundary locations.

## 4.4 Validation

As said previously were tested a start mesh and a refined mesh, on the refined mesh also were tested different turbulence model. Parameter checked was the overall effectiveness of cooling,

$$\eta_{ov} = \frac{T_g - t_w}{T_g - T_c} \quad (4.4.1)$$

across the centerline between the holes, this is the worse case (see Cap.3), and was plotted in function of distance from leading edge.

### 4.4.1 Mesh sensitivity study

Realizable k-eps turbulence model was employed when assessing the sensitivity of the results to the computational mesh, since it was already employed in previous studies successfully (ref.) The enhanced wall treatment was used to model the flow field near the solid walls of the domain. The resultant overall effectiveness was compared. Fig.4.8 shows that the coarse mesh does not provide a good agreement with the experimental data. In order to improve the results, the mesh was therefore refined near the walls as described in Section4.2.

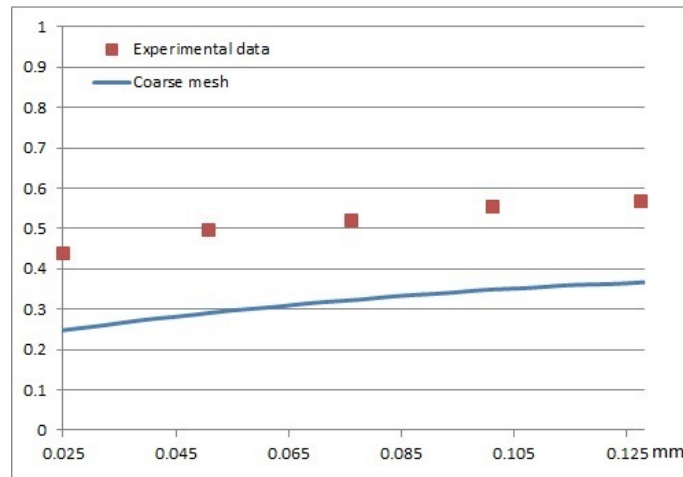


Figure 4.8: Overall effectiveness in function of distance from the leading edge. Comparison with experimental data

#### 4.4.2 Effect of turbulence model in refined mesh

For the refined mesh we will compare the overall effectiveness with the experimental data with different turbulence model, in order to understand how much does the turbulence model change this parameter, and then for the best agreement with experimental data we will proceed to observe some results about the turbulence model chosen.



**Standard k- $\epsilon$**

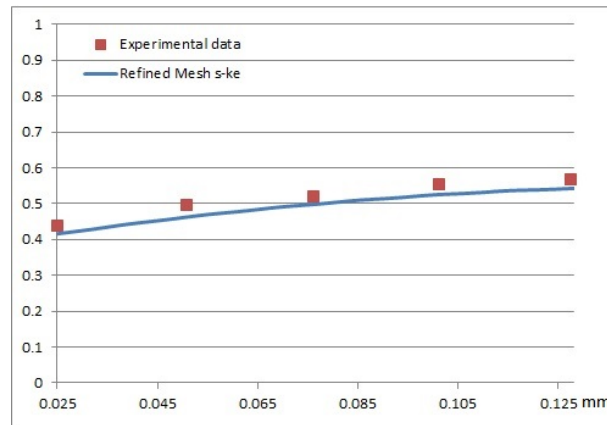


Figure 4.9: Overall effectiveness in function of distance from the leading edge comparison with experimental data

**Realizable k- $\epsilon$**

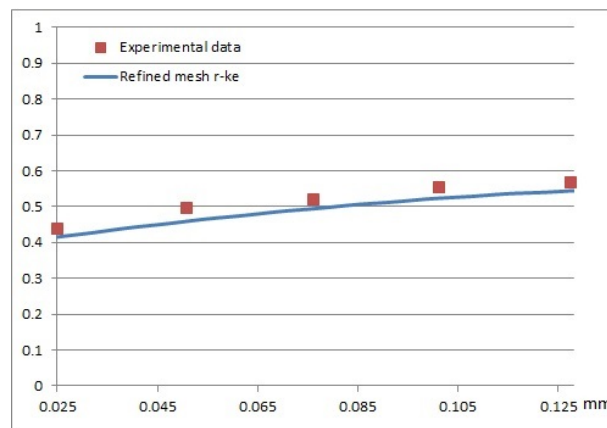


Figure 4.10: Overall effectiveness in function of distance from the leading edge comparison with experimental data

**Standard  $k-\omega$**

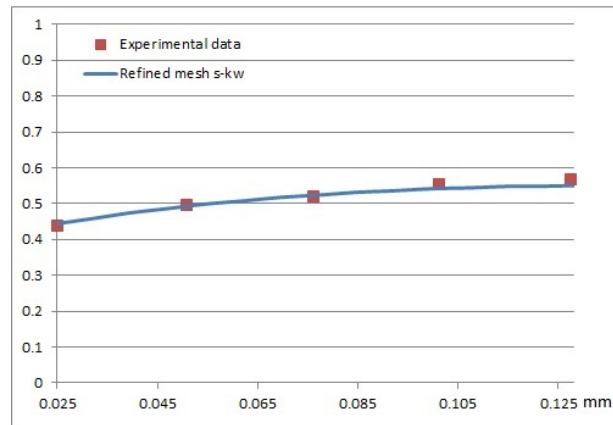


Figure 4.11: Overall effectiveness in function of distance from the leading edge comparison with experimental data

**SST  $k-\omega$**

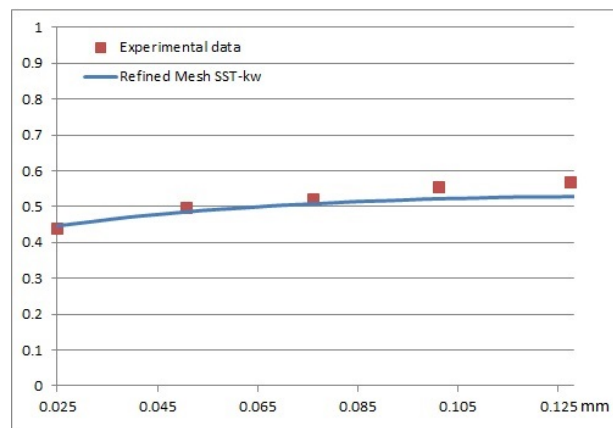


Figure 4.12: Overall effectiveness in function of distance from the leading edge comparison with experimental data

### Comments

All the turbulence models produce an overall good agreement with the experimental data available. Both realizable and standard  $k - \epsilon$  predict the trend of the overall effectiveness better than the standard  $k - \omega$  model. The standard  $k - \omega$  model gives a better agreement for the first three thermocouples, while the difference with the experimental data increases towards the end of the plate. Similar behaviour can be observed with the SST  $k - \omega$  model.

Based on these results, the optimisation study was performed employing the realizable  $k - \epsilon$ .

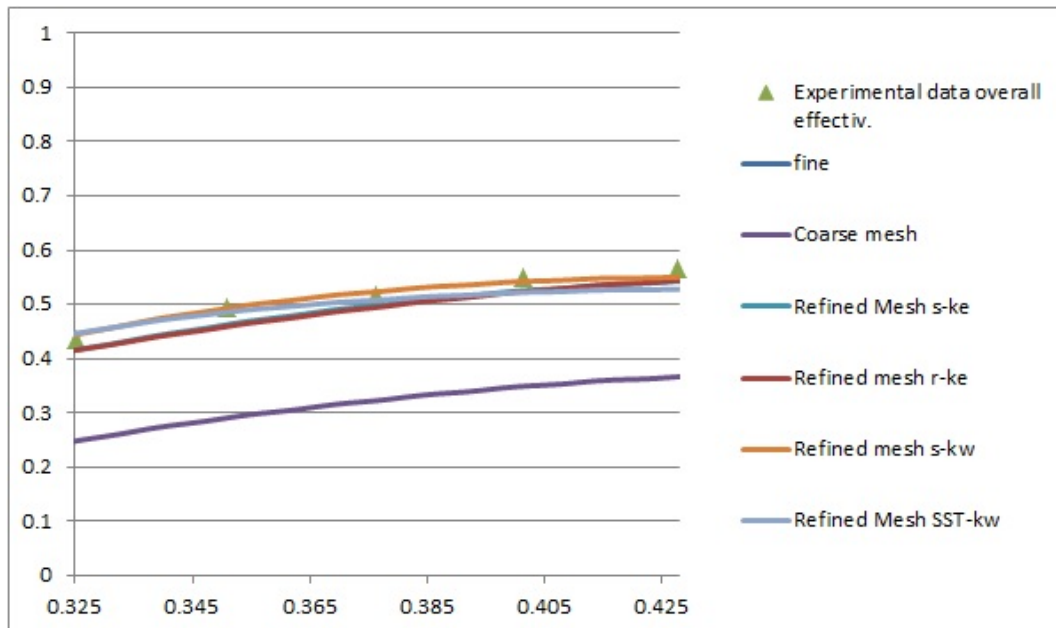


Figure 4.13: Overall effectiveness. Comparison of different turbulence models in refined mesh.

## 4.5 Baseline Results

### 4.5.1 Temperature

From the temperature map on the symmetry plane of the fluid zone, it is possible to see that the cooling stream generates a low temperature region adjacent to the plate.

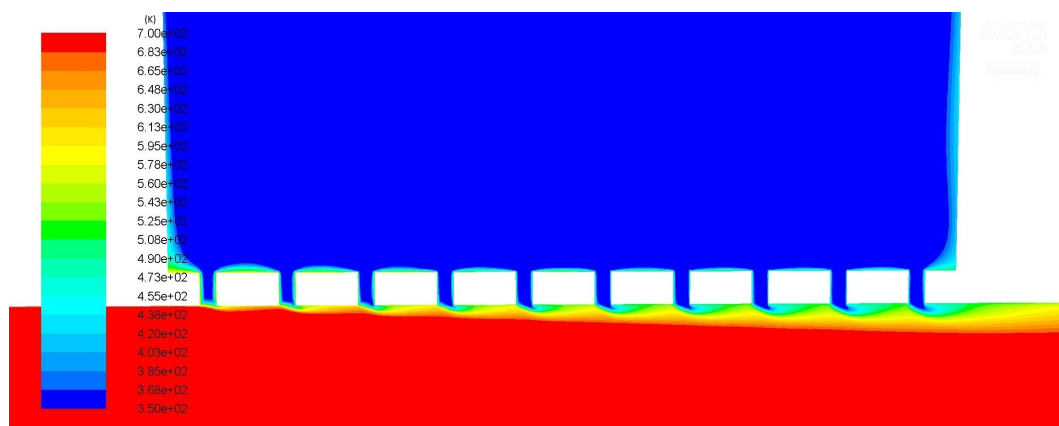


Figure 4.14: Temperature contours on symmetry plane

### 4.5.2 Velocity vectors

From this pictures of velocity vectors it is possible to observe that this model get the detachment of the flow at the inlet of the holes, and a little recirculation zone after each hole. Moreover the boundary layer is good described, because we have value of  $y^+ < 10$ . It is clear that the cooling jet separated from the test plate surface as it created a recirculation zone extending no farther than one hole diameter from the cooling hole trailing edge. The flow quickly

reattached to the wall.

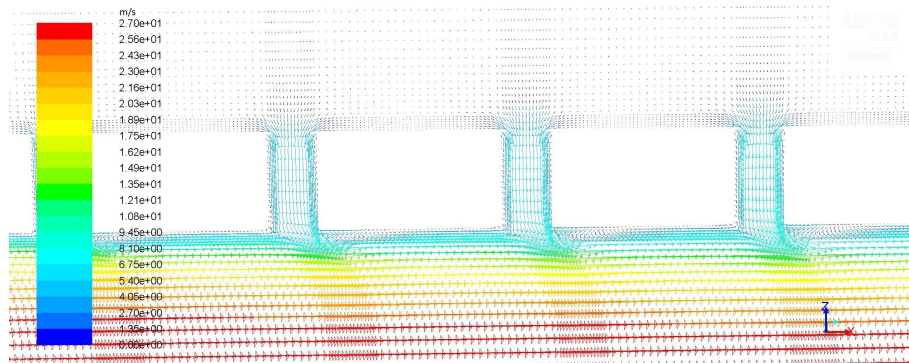


Figure 4.15: Velocity vectors on symmetry plane

### 4.5.3 Concentration of tracer

In order to verify the absence of mixing between hot and coolant fluids, a tracer was introduced in the coolant. The absence of mixing would ensure the effectiveness of the cooling. Following figure shows that a high concentration of the tracer is present near the plate.

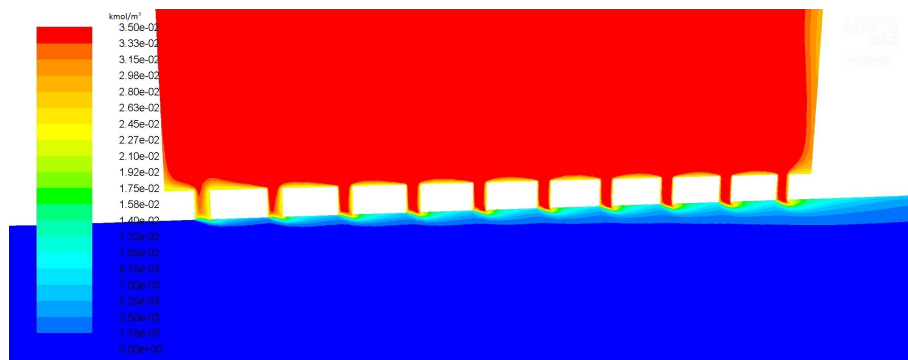


Figure 4.16: Molar concentration of tracer

#### 4.5.4 Overall Effectiveness on the plate

Adiabatic effectiveness measurements were made on the effusion test plate. This region was chosen to capture the cooling characteristics of all 10 rows of cooling holes. The measurement region captured one column of cooling holes located at the midpitch of the test plate. Conditions were found to be pitchwise periodic over the measurement region. It can also be seen from the contours that there is conduction upstream of the test plate, evidenced by the nonzero effectiveness levels at the leading edge. This conduction can be explained by the fact that the cooling holes are cooling the plate through convection within the holes.

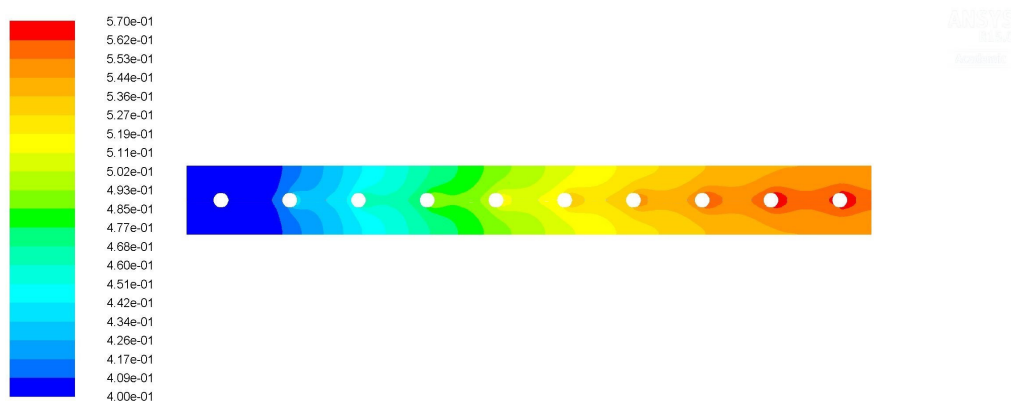


Figure 4.17: Overall effectiveness contours on the plate

### 4.5.5 Pseudo-Adiabatic Effectiveness

The film temperature adjacent to the wall is the adiabatic temperature if there is no heat transfer to the wall. Its measurement in the present work with active heat transfer is referred to as a pseudo adiabatic cooling effectiveness. It is a measurement that can be predicted in conjugate heat transfer CFD. The pseudo adiabatic wall cooling effectiveness was defined in the same way as for the overall cooling effectiveness, but uses the temperature of the gas adjacent to the wall at the midpoint of the square array of holes. This was a measurement of the worst case (furthest from the effusion jet centreline) heat transfer location. The pseudo adiabatic cooling effectiveness and its development with axial distance is shown in Fig.4.18

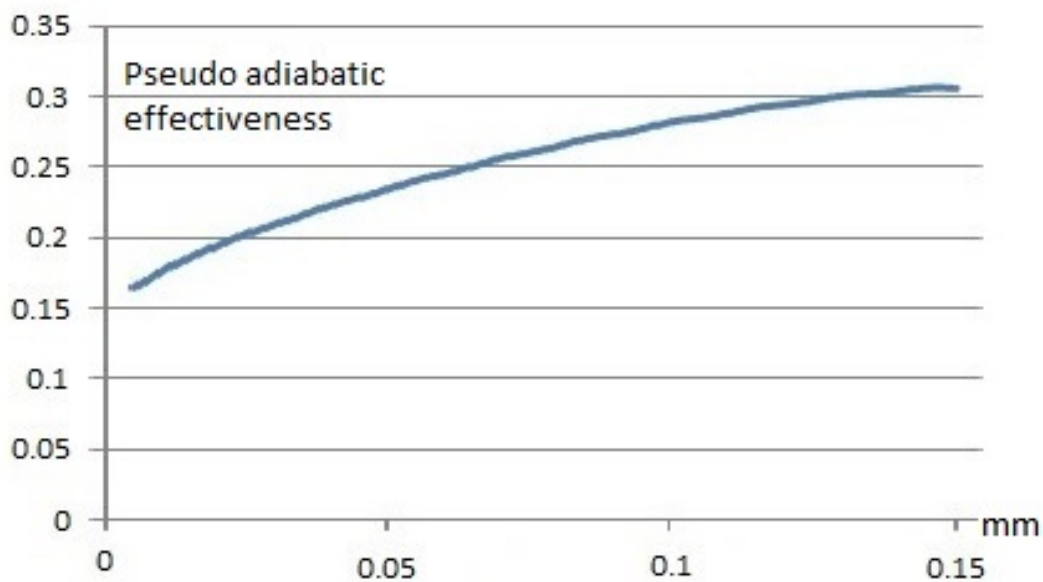


Figure 4.18: Comparison of overall effectiveness between the different meshes and turbulence models

# Chapter 5

## RBF-Morph for shape optimization

### 5.1 RBF Morph

In the last chapter were shown results of baseline. In literature many approach where developed to optimize the overall effectiveness.

This is the most important parameter to optimize, and it could be done in different way.

One way is changing the pitch between holes array. Most of research use to optimize plate with square array of holes. In this work we will change the X-pitch and Y-pitch independently, in order to have an improvement of cooling effectiveness. In particular it will be take in consideration, non just the pitch  $(X,Y)$ , but also the ratio  $X/D$ ,  $Y/D$ , fixing the diameter of the holes.

Other shape modification, used in most of scientific researches, is changing the angle of injection; historically the angle used were  $90^\circ$  and  $30^\circ$ , we will develop a larger number of injection angle.

The starting mesh has an injection with an angle of  $90^\circ$ .



Even negative angles will be investigated, i.e. injection in opposite direction of the main flow. Apparently the last one solution discussed, could be an anti-intuitive solution. But in this way, we could have a better coverage of the plate by the hot flow, and a better attachment of the cold flow on the plate.

Following these assumptions, in the next few pages will be shown how the optimization process has been developed.

Furthermore using RBF-Morph could be done an optimization without re-execute the entire process of regeneration of the geometry and re-meshing, so this system would speed up the time of the entire project. Besides this allows us to implement a greater number of tests, and create mixed solutions with different modifications applied simultaneously.

Once developed the morph modification, these will be included in Ansys Workbench and it will be created a grid of cases with different amplifications of the different RBF-Morph solutions.

Hence starting from the design point the workbench will create the response surface of the parameter of interest in function of the amplification of the shape modification.

Thanks this we get information about sensitivity of the output parameter  $(\eta_{ov}, \eta_{ad})$  to the changes in the input parameter  $(X/D, Y/D, \alpha)$

### 5.1.1 X-Pitch

The first solution implemented is changing X-Pitch, fixing  $D=\text{cost}$ .

#### Setup Details

First thing to do is define a domain, the mesh out of domain is non affected by morph solution. If a domain isn't defined the Morph solution will affect the entire mesh.

In this case it isn't set any domain. Then we will assign the same displacement to each hole and to external surfaces as can be seen in Fig.5.1 and 5.2. In this way we will have a greater (with positive amplification) or lower X-Pitch (with negative amplification).

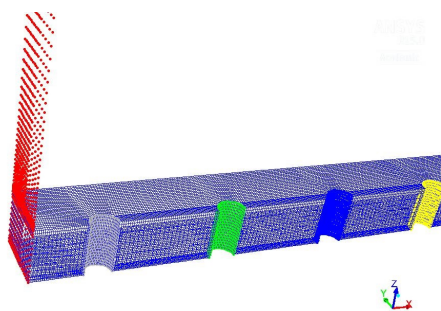


Figure 5.1: Display Points

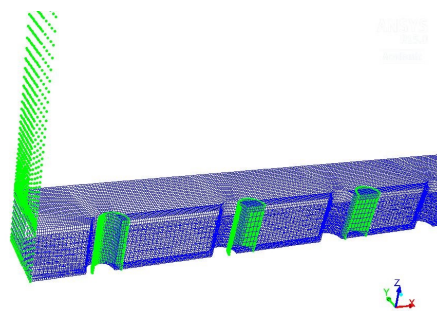


Figure 5.2: Preview Points

### Shape modification

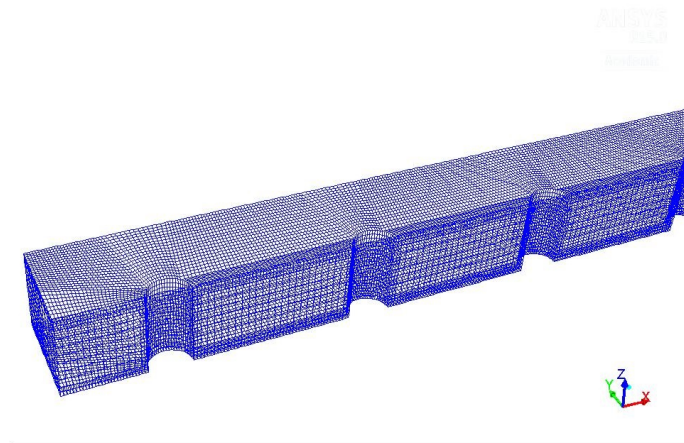


Figure 5.3: Base

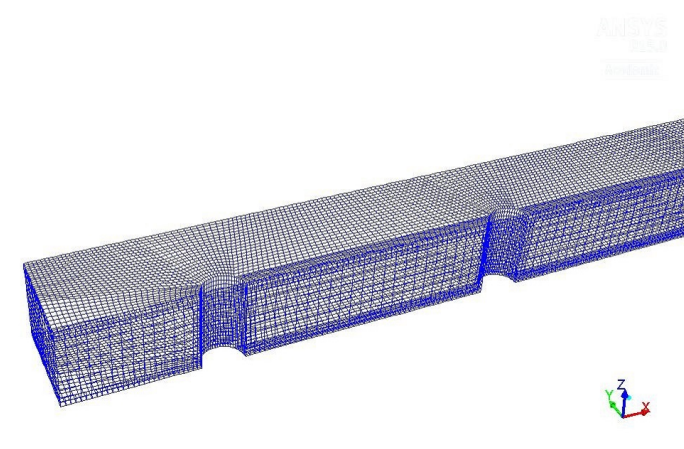


Figure 5.4: Amplification 5

### 5.1.2 Y-Pitch

Second solution developed is changing Y-Pitch, even in this case fixing  $D=cost$ .

#### Setup Details

In this shape modification the entire domain will be expanded, so in particular the left symmetry plane will be fixed, and the right plane with the holes will be moved, the rest of the mesh will be adapted accordingly to this conditions. Also negative amplification will be used, i.e. reduction of the YPitch. In this way we will have a greater or lower Y-Pitch, as can be seen in Fig.5.7 and 5.8.

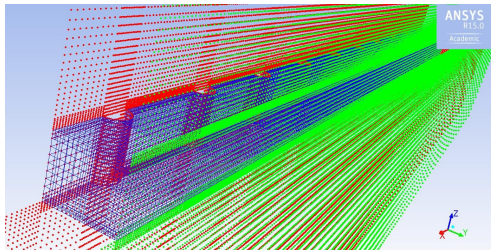


Figure 5.5: Display Points

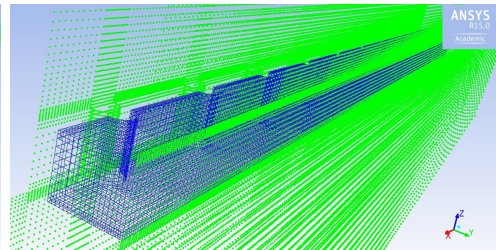


Figure 5.6: Preview Points

**Shape modification**

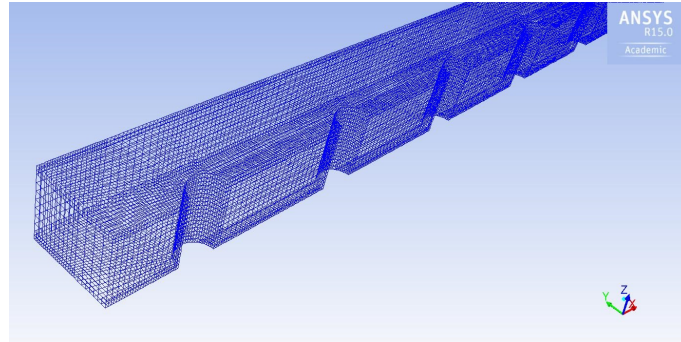


Figure 5.7: Base

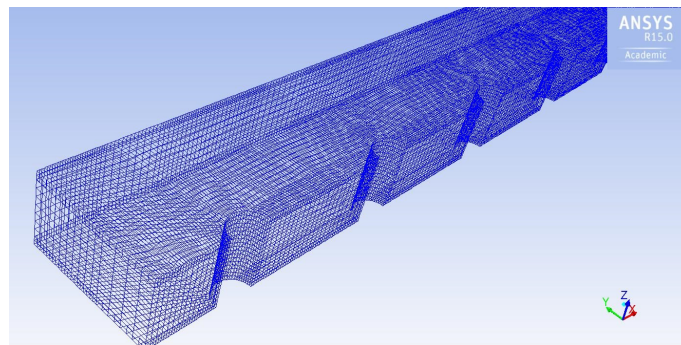


Figure 5.8: Amplification 5

### 5.1.3 Rotation

Last solution developed is variation of injection angle, giving a rotation to the holes, even in this case fixing  $D=\text{cost}$ .

#### Setup Details

This shape modification is done giving an opposite displacement to the two different fluid zones, i.e. the cold fluid zone has a negative displacement in x-direction, the hot fluid zone has a positive displacement in x-direction, thereafter monitoring the displacement of the points belonging to the holes surfaces, keeping attention that the hole remain cylindrical. As previously said this solution will be used even with negative amplifications, getting a backward injection of cooling air.

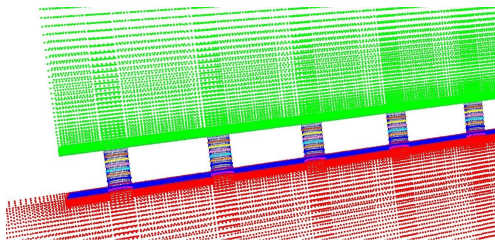


Figure 5.9: Display Points

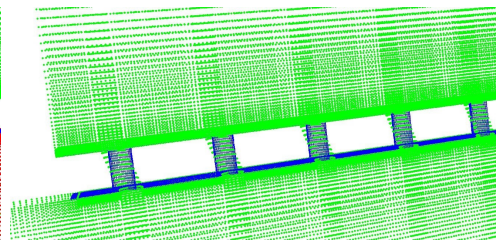


Figure 5.10: Preview Points

### Shape modification

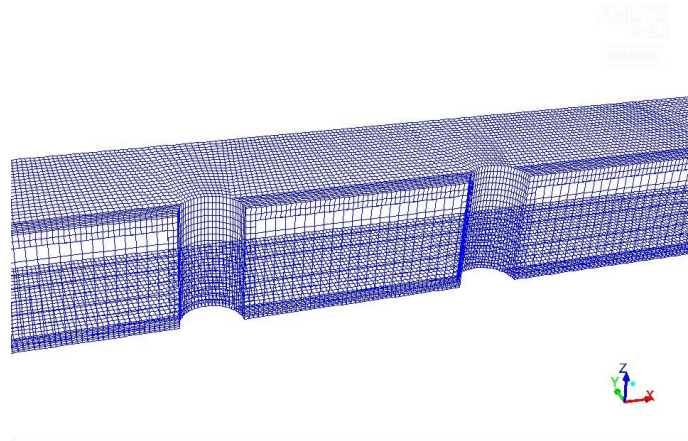


Figure 5.11: Base

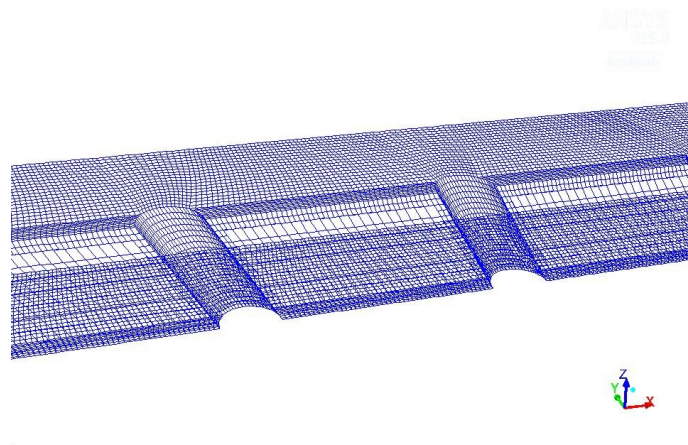


Figure 5.12: Amplification 5

# Chapter 6

## Workbench and Results

### 6.1 Workbench Implementation

#### 6.1.1 Design of experiment

The main purpose of design exploration is to identify the relationship between the performance of the product (maximum stress, mass, fluid flow, velocities, etc.) and the design variables (dimensions, loads, material properties, etc.). Based on these results, the analyst will be able to influence the design so as to meet the product's requirements. He will be able to identify the key parameters of the design and how they influence the performance.

The first step of any design simulation is to create the simulation model. The simulation model can use anything from a single physics up to a complex multiphysics simulation involving multiple conditions and physics coupling.

In addition to performing the standard simulation, this step is also used to define the parameters to be investigated. The input parameters (also called design variables) are identified, and may include CAD parameters, loading conditions, material properties, etc.



The output parameters (also called performance indicators) are chosen from the simulation results and may include maximum stresses, fluid pressure, velocities, temperatures, or masses, and can also be custom defined. Product cost could be a custom defined parameter based on masses, manufacturing constraints, etc.

In this work why didn't use CAD parameters but RBF-Morph parameter, this let us to have a shorter time to run the simulation, without re-meshing the model.

### **6.1.2 Response Surface**

Once the initial model has been created and parameters defined, the next step in the session is to create a response surface. After inserting a Response Surface system in the project, you need to define the design space by giving the minimum and maximum values to be considered for each of the input variables. Based on this information, the Design of Experiment (DOE) part of the Response Surface system will create the design space sampling. Note that this sampling depends upon the choice made for the DOE scheme – usually, the default CCD scheme will provide good accuracy for the final approximation. Then, the DOE needs to be computed.

Once the DOE has been updated, a response surface is created for each output parameter. A response surface is an approximation of the response of the system. Its accuracy depends on several factors: complexity of the variations of the output parameters, number of points in the original DOE, and choice of the response surface type. Several main types of response surfaces

are available in DesignXplorer. As a starting point, the Standard Response Surface (based on a modified quadratic formulation) will provide satisfying results when the variations of the output parameters is mild, while the Kriging scheme will be used for stronger variations.

After the response surfaces have been computed, the design can be thoroughly investigated using a variety of graphical and numerical tools, and valid design points identified by optimization techniques.

Usually, the investigation will start with the sensitivity graphs. This bar or pie chart will graphically show how much the output parameters are locally influenced by the input parameters around a given response point. Note that varying the location of the response point may provide totally different graphs. Thinking of the hill/valley analogy, if the response point is in a flat valley, the influence of the input parameters will be small. If the point is at the top of a steep hill, the influence of the parameters will be strong. The sensitivity graphs provide the first indication about the relative influence of the input parameters.

The response surfaces will provide curves or surfaces that show the variation of one output parameter with respect to one or two input parameters at a time. These curves/surfaces also are dependent on the response point.

Once one or several design points have been identified, the probabilistic analysis will help quantify the reliability or quality of the product by means of a statistical analysis. Probabilistic analysis typically involves four areas of statistical variability: geometric shape, material properties, loading, and

boundary conditions. For example, the statistical variability of the geometry of a product would try to capture product-to-product differences due to manufacturing imperfections quantified by manufacturing tolerances. Probabilistic characterization provides a probability of success or failure and not just a simple yes/no evaluation. For instance, a probabilistic analysis could determine that one part in 1 million would fail, or the probability of a product surviving its expected useful life.

To get accurate response surfaces within a reasonable amount of time, the number of input parameters should be limited to 10 to 15. If more parameters need to be investigated, the correlation matrix will provide a way to identify some key parameters before creating the response surface. The Parameters Correlation systems should be used prior to the Response Surface systems, to reduce the number of parameters to the above mentioned limit. The Parameters Correlation method will perform simulations based on a random sampling of the design space, so as to identify the correlation between all parameters. The number of simulations will depend upon the number of parameters, as well as the convergence criteria for the means and standard deviations of the parameters. The user can provide a hard limit for the number of points to be computed, it should be noted that the accuracy of the correlation matrix might be affected if not enough points are computed.

ANSYS DesignXplorer provides tools to estimate and improve the quality of the response surfaces. Once response surfaces are built, you can create and manage response points and charts. These postprocessing tools allow exploring

the design and understanding how each output parameter is driven by input parameters and how the design can be modified to improve its performances.

### 6.1.3 Optimization

A Response Surface Optimization system draws its information from its own Response Surface component, and so is dependent on the quality of the response surface.

To create a Goal Driven Optimization system on your Project Schematic:

- With the Project Schematic displayed, drag either a Response Surface Optimization or a Direct Optimization template from the Design Exploration area of the toolbox and drop it on the Project Schematic. You may drag it:
  - directly under the Parameter Set bar or an existing system directly under the Parameter Set bar, in which case it will not share any data with any other systems in the Project Schematic.
  - onto the Design of Experiments component of a system containing a Response Surface, in which case it will share all of the data generated by the DOE component.
  - onto the Response Surface component of a system containing a Response Surface, in which case it will share all of the data generated for the DOE and Response Surface components. For more detailed information on data transfer, see [Transferring Design Point Data for Direct Optimization](#)

- For a Response Surface Optimization system, if you are not sharing the DOE and Response Surface cells, edit the DOE, set it up as described in Design of Experiments Component Reference, and solve both the DOE and Response Surface cells.
- For a Direct Optimization system, if you have not already shared data via the options in Step 1, you have the option of creating data transfer links to provide the system with design point data.
- On the Project Schematic, double-click on the Optimization cell of the new system to open the Optimization tab.
- Specify the optimization method.
  - In the Optimization tab Outline view, select the Optimization node.
  - In the Properties view, select an optimization method and specify its optimization properties. For details on the available optimization algorithms, see Goal Driven Optimization Methods .
- Specify optimization objectives or constraints.
  - In the Optimization tab Outline view, select either the Objectives and Constraints node or an item underneath it.
  - In the Table or Properties view, define the Optimization objectives and constraints. For details, see Defining Optimization Objectives and Constraints .
- Specify the optimization domain.

- In the Optimization tab Outline view, select the Domain node or an input parameter or parameter relationship underneath it.
  - In the Table or Properties view, define the selected domain object. For details, see *Defining the Optimization Domain* (p. 148).
- Click the Update toolbar button.

## 6.2 Computational Procedure

Final step of this work is the optimization of the model created and validated in previous chapters. The optimization process is driven by Ansys Workbench. the main parameter monitored are:

- Average *Overall effectiveness*
- Average *Adiabatic effectiveness*
- Maximum *Overall effectiveness*
- Maximum *Adiabatic effectiveness*

The most important Parameter to optimize between these is the average *overall effectiveness* on the wall.

The entire process start with fluent creating five output parameters, previously listed, and three input parameters:

- Rotation of the holes
- Stretching Pitch in X direction

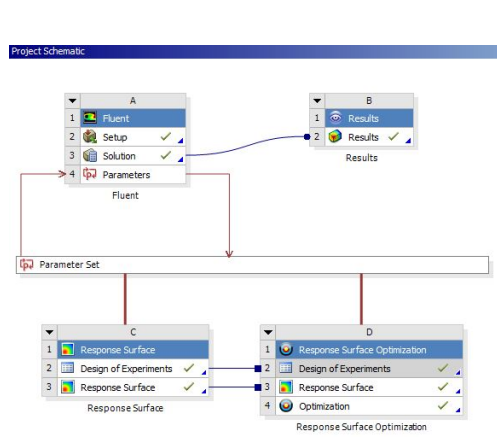


Figure 6.1: Ansys Workbench project

Outline of Schematic (2): Design of Experiments	
A	B
1	Enabled
2	Design of Experiments
3	Input Parameters
4	Fluent (A1)
5	P1 - rotation
6	P2 - stretchX
7	P3 - stretchY
8	Output Parameters
9	Fluent (A1)
10	P8 - ad-effectiveness-average
11	P7 - ov-effectiveness-average
12	P9 - ad-effectiveness-max
13	P10 - ov-effectiveness-max
14	Charts
15	Parameters Parallel
16	Design Points vs Parameter

Properties of Outline / Design of Experiment	
A	B
Property	Value
1	Design Points
2	Preserve Design Points After OX Run
3	Export Project for Each Preserved Design Points
4	Failed Design Points Management
5	Number of Retries
6	Design of Experiments Type
7	Optimal Space-Filling Design
8	Design Type
9	Max-Min Distance
10	Maximum Number Of Cycles
11	10
12	Samples Type
13	CCD Samples
14	Random Generator Seed
15	0

Figure 6.2: Design of experiments

- Stretching Pitch in Y direction

Control of all transactions will be done by main Workbench platform, creating the various combinations of RBF-Morph sol, and showing directly on the screen of the parameter set the desired output.

The creation of the design point is done using **Design of experiment**, and the sequent setting for it:

- Design of Experiment Type: Optimal Space Filling Design
- Design Type: Max-Min distance
- Maximum Number of Cycles: 10
- Samples Type: CCD Samples

With this procedure Design of experiment will choose 15 Design Points, with an optimal space filling in the space of the parameters.

## 6.3 Results

After run the 15 Design Points chosen with design of experiment, we have the sequent results:

Input Parameter			Output Parameter				
Rotat. of the holes	Stretch Pitch in X	Stretch Pitch in Y	Adiab. effect. aver.	Over. effect. aver.	Adiab. effect. max	Over. effect. max	Over. effect. min
3.3	3.2	-2.0	0.243	0.468	0.356	0.616	0.408
0.0	2.4	2.8	0.216	0.409	0.290	0.514	0.358
-2.7	5.6	0.0	0.223	0.383	0.314	0.550	0.367
-3.3	0.0	-1.6	0.249	0.413	0.388	0.650	0.405
-0.7	-5.6	-1.2	0.204	0.351	0.323	0.573	0.275
2.0	4.8	0.8	0.220	0.416	0.310	0.548	0.369
-2.0	-3.2	2.4	0.210	0.351	0.319	0.557	0.284
-1.3	4.0	-2.4	0.258	0.445	0.382	0.643	0.424
-4.0	1.6	1.6	0.228	0.389	0.319	0.576	0.381
2.7	-4.8	1.2	0.209	0.360	0.308	0.546	0.279
-4.7	-4.0	0.4	0.213	0.366	0.354	0.654	0.285
4.7	-1.6	-0.8	0.242	0.407	0.342	0.596	0.338
1.3	-2.4	-2.8	0.245	0.411	0.382	0.640	0.327
4.0	0.8	2.0	0.232	0.393	0.315	0.563	0.480
0.7	-0.8	-0.4	0.220	0.363	0.332	0.557	0.344

In this table we can see what happens to the output parameter with changing in the input parameter. In the first three column we can see the amplification of the modification imposed.

The amplification of the shape modification are the input parameters given in Ansys to manage the optimization process, but the meaning of that amplification is explained in the next table.

We imposed an amplification for the rotation  $\pm 5$ , that gives a variation of



the angle between the holes axis and the plate in the range  $\pm 32.7^\circ$ .

The amplification of the pitch in X direction is in the range  $\pm 6$ , and the amplification of the pitch in Y direction is in the range  $\pm 3$  because XZ plane has a symmetry condition, and hence an amplification in Y direction worth double than in X.

	Rotation	Stretch X	Stretch Y
Ampl.	Angle (deg)	Pitch-X (mm)	Pitch-Y (mm)
-6	/	10.64	/
-5	32.7 °	11.4	/
-4	39.0 °	12.16	/
-3	46.7 °	12.92	10.64
-2	57.8 °	13.68	12.16
-1	72.5 °	14.44	13.68
0	90 °	15.2	15.2
1	72.5 °	15.96	16.72
2	57.8 °	16.72	18.24
3	46.7 °	17.48	19.76
4	39.0 °	18.24	/
5	32.7 °	19	/
6	/	19.76	/

### 6.3.1 Average Overall effectiveness

#### 2D Maps

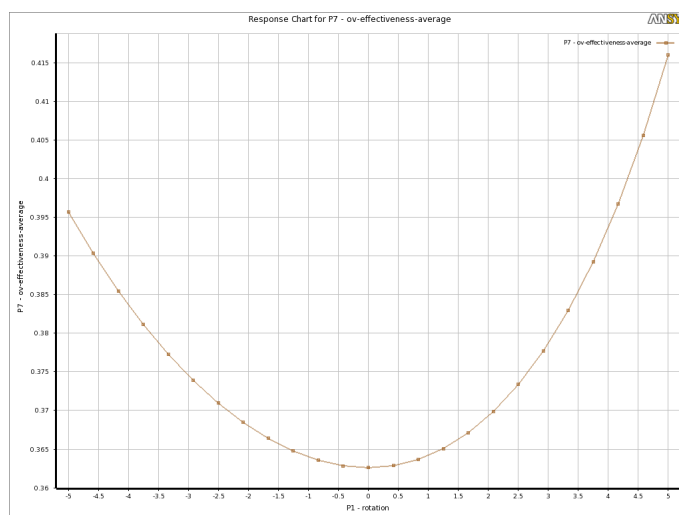


Figure 6.3: Average Overall effectiveness as a function of rotation

Now it will be discussed the trend of the output parameters as functions of the input parameters variations.

In Fig.6.3 we can see, as previously said, that the average overall effectiveness, increases if is increased the angle, or even if it is decreased the angle. The curve has a lower gradient if the angle is negative, this is because of a recirculation zone that born after the hole, but this gives a better coverage of the plate surface.

Increasing the X (Fig.6.4) pitch we have an improvement of the average overall effectiveness with a maximum for the amplification 2.4, but this is not much relevant, and decreasing the pitch we have a worsening of the effectiveness. This will bring us to use positive value for amplification of stretch X, without using extreme amplification.

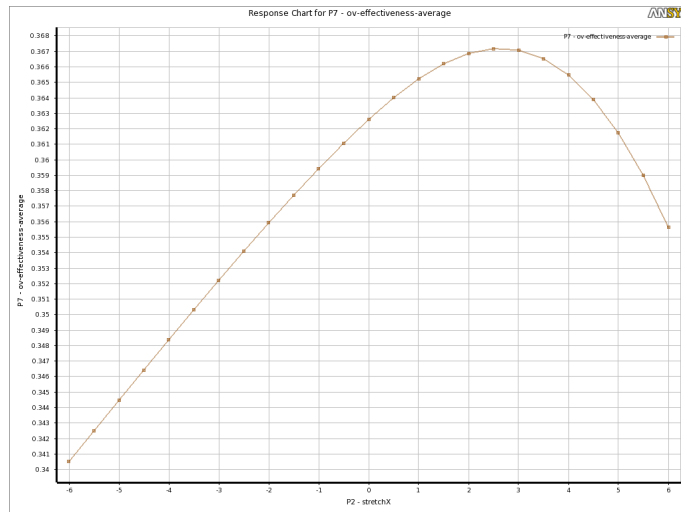


Figure 6.4: Average Overall effectiveness as a function of stretch X

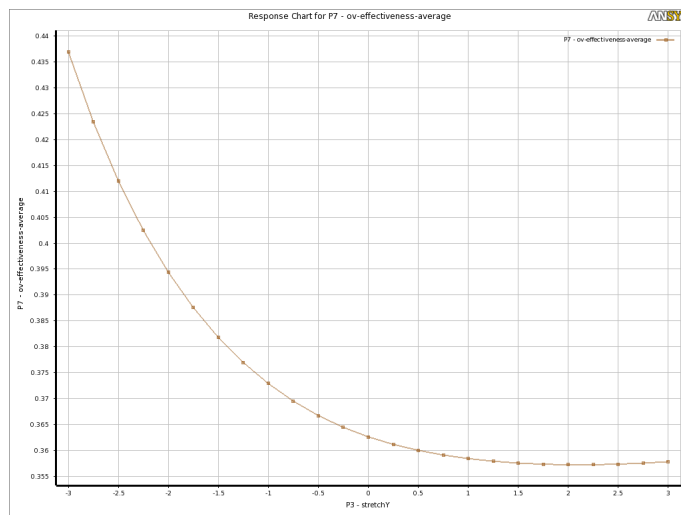


Figure 6.5: Average Overall effectiveness as a function of stretch Y

In Fig.6.5 we can see that it is not convenient use positive amplification for Y pitch, so in the candidate point for the optimization we will have only negative amplification for this solution, this means that in the cross section the holes are more closer.

### 3D Maps

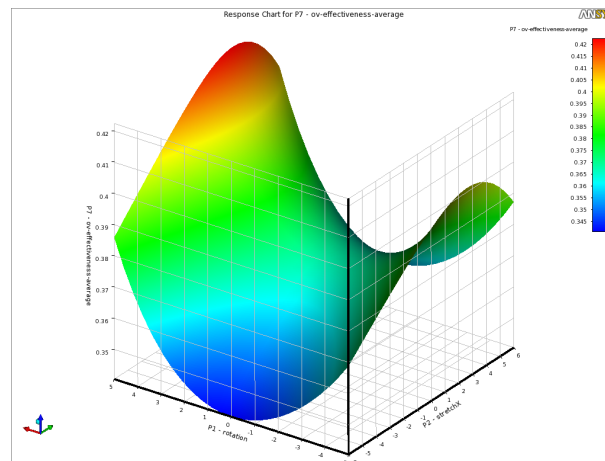


Figure 6.6: Average Overall effectiveness as a function of rotation and stretchX

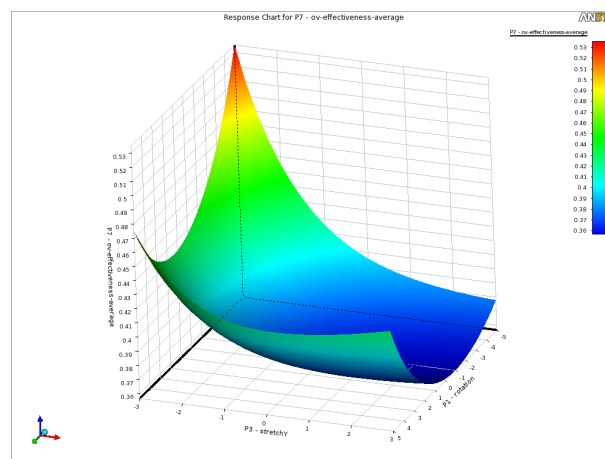


Figure 6.7: Average Overall effectiveness as a function of rotation and stretchY

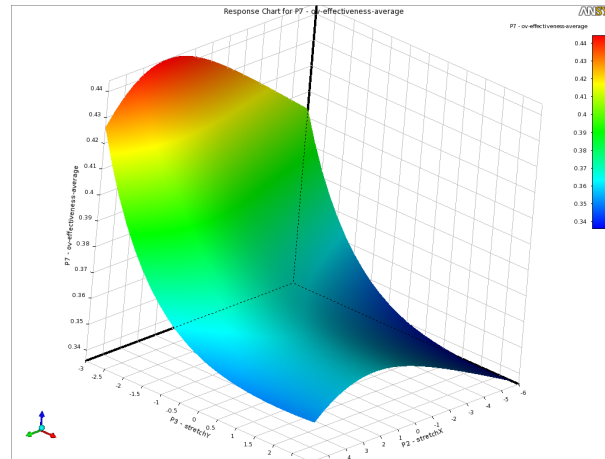


Figure 6.8: Average Overall effectiveness as a function of stretchX and stretchY

### 6.3.2 Maximum Overall effectiveness

#### 2D Maps

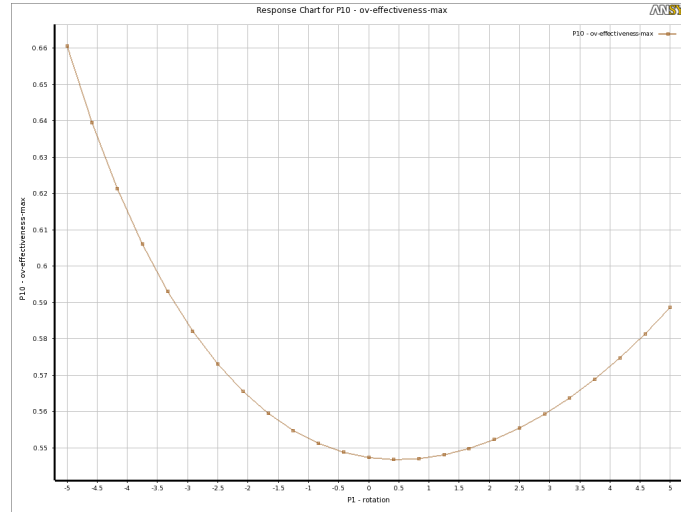


Figure 6.9: Maximum Overall effectiveness as a function of rotation

The maximum overall effectiveness has a similar behaviour of the average overall effectiveness, but the minimum point isn't on amplification 0 but 0.7, that means a rotation of 12°. And an improvement if it is increased or

decreased the angle. From Fig.6.9 we can see that increasing the angle we have an increasing of the max overall effectiveness, but with a negative amplification, i.e. backflow, the increasing of the overall effectiveness is more significant.

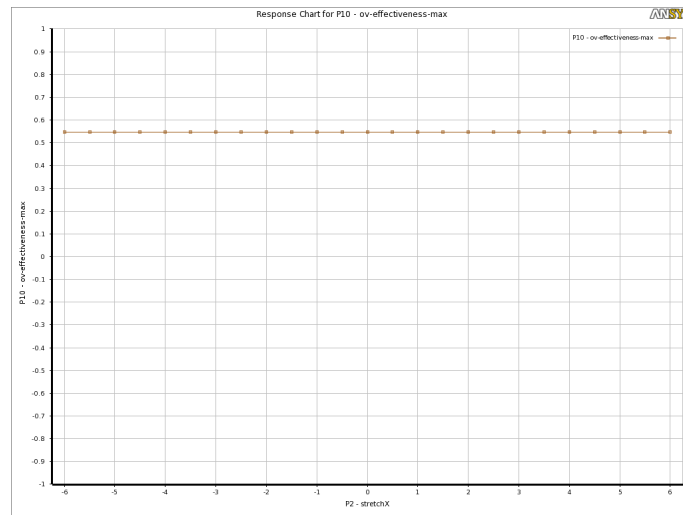


Figure 6.10: Maximum Overall effectiveness as a function of stretch X

Unlike the average overall effectiveness Fig.6.10 show that for the max overall effectiveness is sensible with the variation of the pitch in X direction.

In Fig.6.11 like, the average overall effectiveness, it can be seen that increasing the Y-pitch we get a decreasing of the maximum overall effectiveness, and an increasing of this with a smaller Y-pitch. This give us no way out than choose a decreasing of Y-pitch for the candidate points.

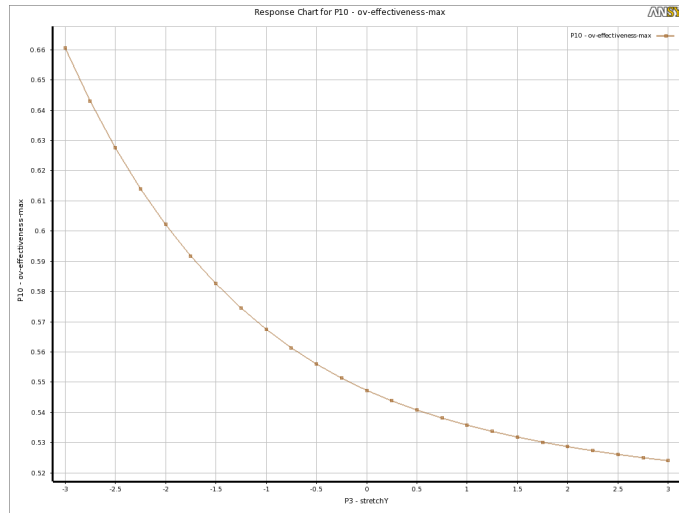


Figure 6.11: Maximum Overall effectiveness as a function of stretch Y

### 3D Maps

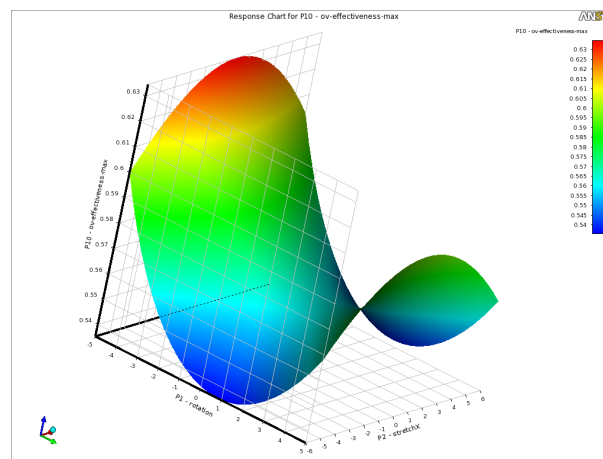


Figure 6.12: Maximum Overall effectiveness as a function of rotation and stretchX

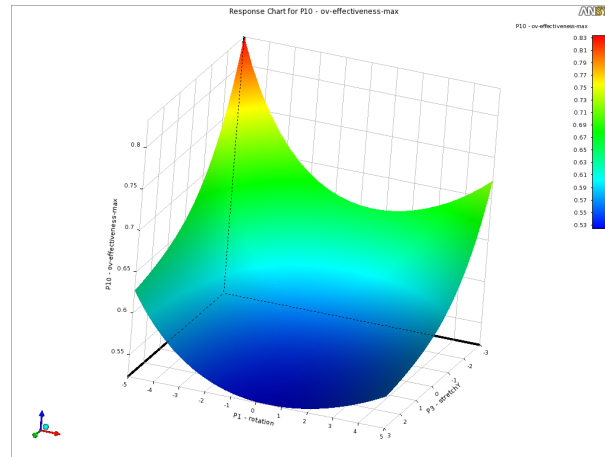


Figure 6.13: Maximum Overall effectiveness as a function of rotation and stretchY

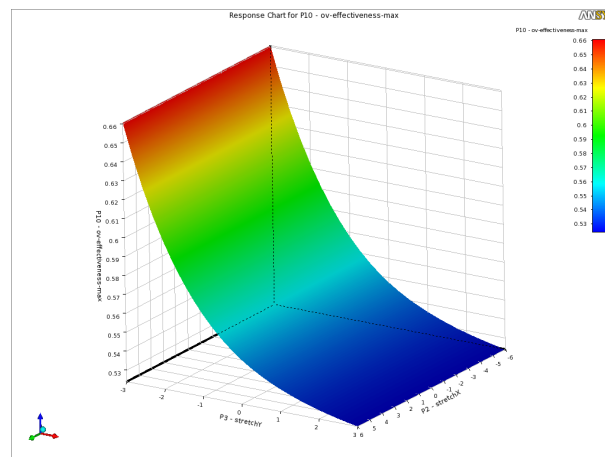


Figure 6.14: Maximum Overall effectiveness as a function of stretchX and stretchY

### 6.3.3 Minimum Overall effectiveness

#### 2D Maps

We have to check this parameters because this ensures that we have a good cooling coverage on the plate.



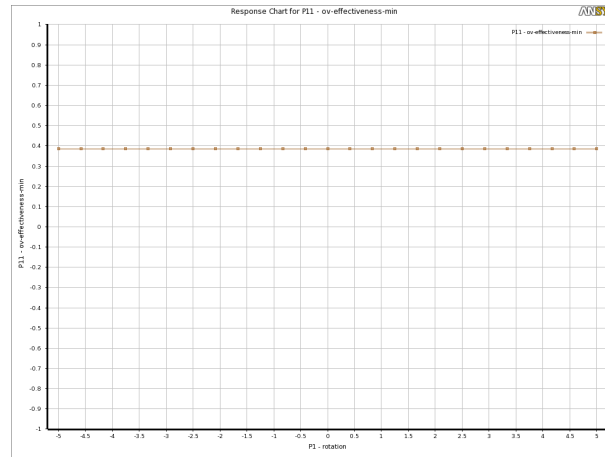


Figure 6.15: Minimum Overall effectiveness as a function of rotation

In particular Fig.6.15 shows that the minimum overall effectiveness is not sensitive to the rotation of the holes.

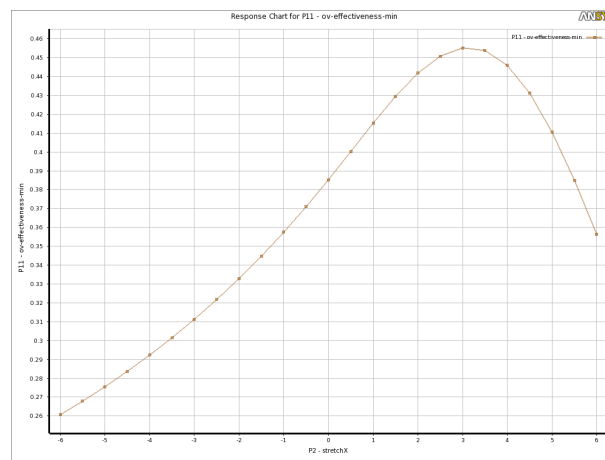


Figure 6.16: Minimum Overall effectiveness as a function of stretch X

As for as the previous cases stretch X (Fig.6.16) with a low amplification gives an improvement with a maximum around amplification 3, and decreasing the X pitch there is a worse minimum overall effectiveness.

In Fig.6.17 like, the average overall effectiveness, it can be seen that

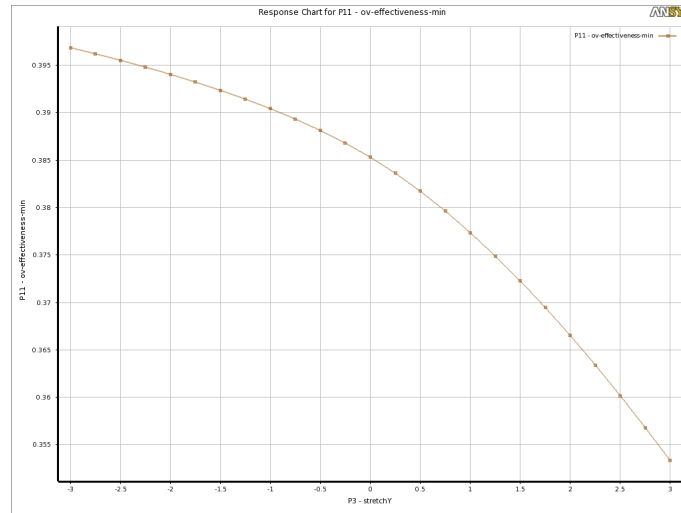


Figure 6.17: Minimum Overall effectiveness as a function of stretch Y

increasing the Y-pitch we get a decreasing of the maximum overall effectiveness, and an increasing of this with a smaller Y-pitch. This give us no way out than choose a decreasing of Y-pitch for the candidate points.

### 3D Maps

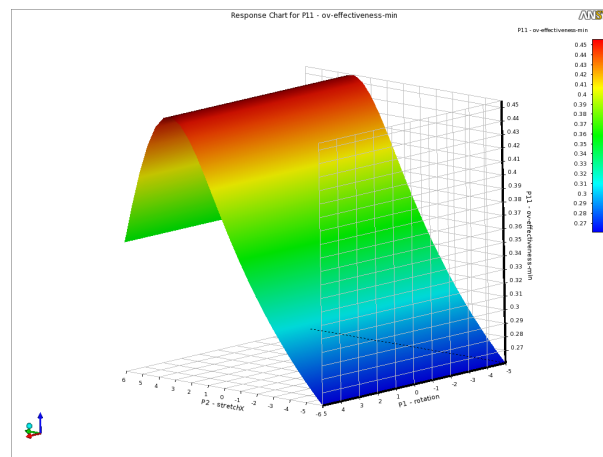


Figure 6.18: Minimum Overall effectiveness as a function of rotation and stretchX

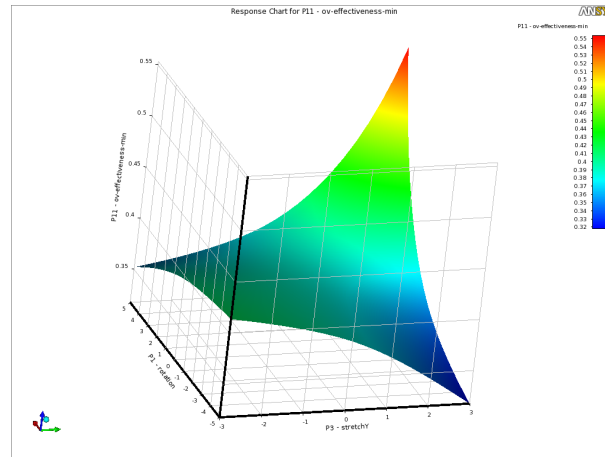


Figure 6.19: Minimum Overall effectiveness as a function of rotation and stretchY

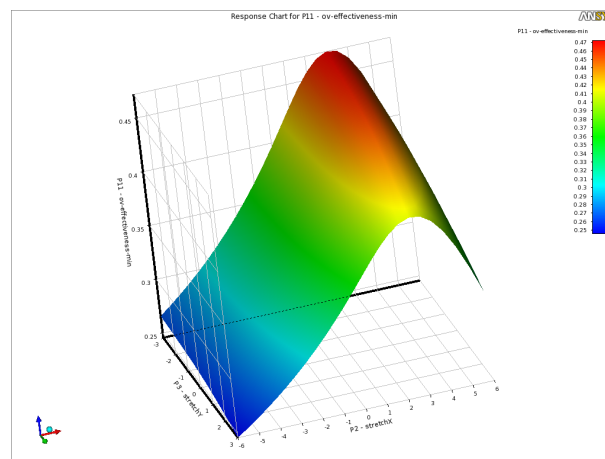


Figure 6.20: Minimum Overall effectiveness as a function of stretchX and stretchY

### 6.3.4 Average Adiabatic effectiveness

#### 2D Maps

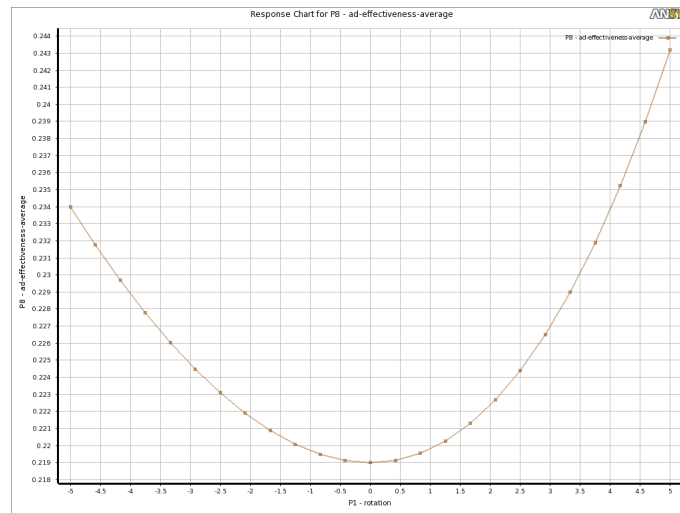


Figure 6.21: Average adiabatic effectiveness as a function of rotation

In Fig.6.21 we can see, as previously said, that the average adiabatic effectiveness, increases if is increased the angle, or even if it is decreased the angle. The curve has a lower gradient if the angle is negative, this is because of a recirculation zone that born after the hole, but this give a better coverage of the plate surface. Of course this results is lower than overall effectiveness because it is measured at 0.2 mm from the surface, and this allow us to consider that like an adiabatic results like if there isn't conjugate heat transfer in the wall.

Increasing the X pitch (Fig.6.22) we have an improvement of the average adiabatic effectiveness, with a maximum around the amplification 2, but this is not much relevant, also decreasing the pitch we have a worse effectiveness. This will bring us to use positive value for amplification of stretch X, without

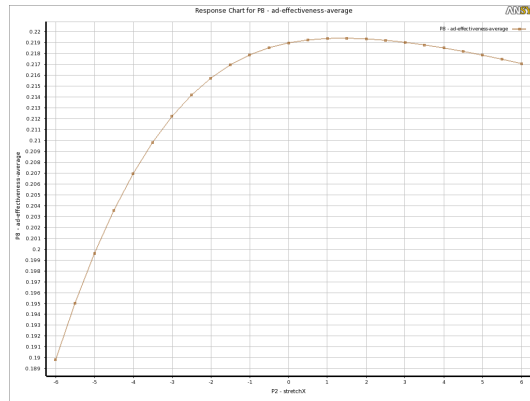


Figure 6.22: Average adiabatic effectiveness as a function of stretch X

using extreme amplification.

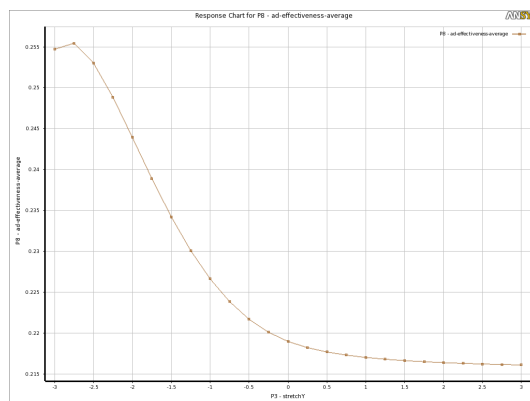


Figure 6.23: Average adiabatic effectiveness as a function of stretch-Y

In Fig.6.23 we can see that it is not convenient use positive amplification for Y pitch, so in the candidate point for the optimization we will have only negative amplification for this solution, this means that in the cross section the holes are more closer.

### 3D Maps

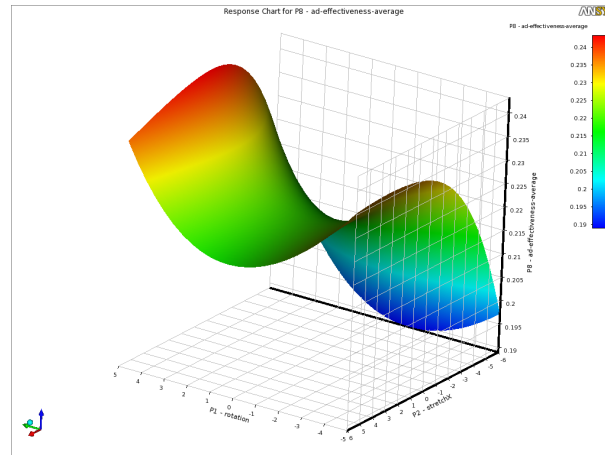


Figure 6.24: Average adiabatic effectiveness as a function of rotation and stretchX

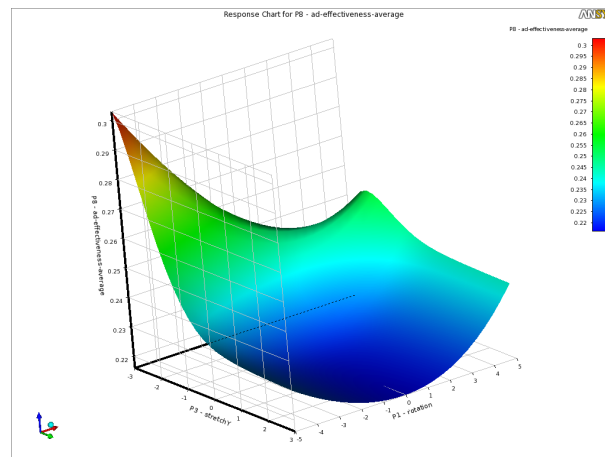


Figure 6.25: Average adiabatic effectiveness as a function of rotation and stretchY

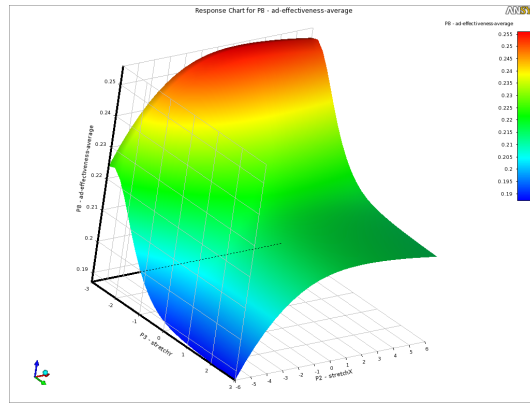


Figure 6.26: Average adiabatic effectiveness as a function of stretchX and stretchY

### 6.3.5 Maximum Adiabatic effectiveness 2D Maps

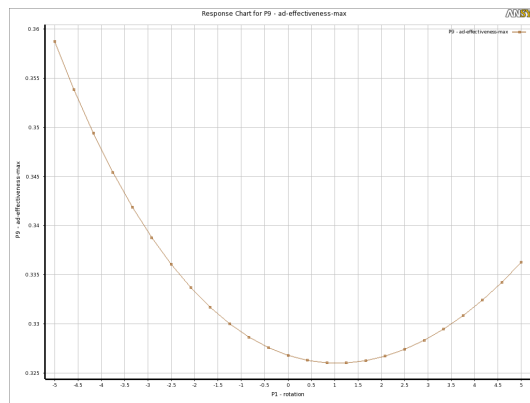


Figure 6.27: Maximum adiabatic effectiveness as a function of rotation

In Fig.6.27 like the previous we can see that the maximum adiabatic effectiveness increase with the variation of the angle of the holes, both sides.

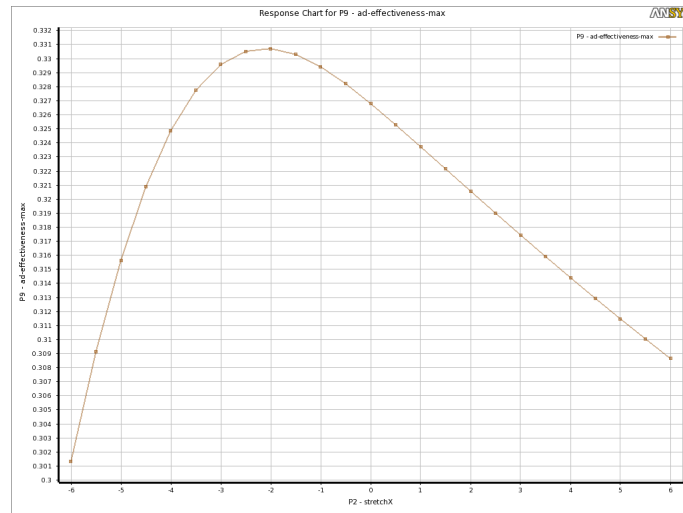


Figure 6.28: Maximum adiabatic effectiveness as a function of stretch X

As the max overall effectiveness, even the adiabatic one decrease at least about 5 % changing the X-Pitch (Fig.6.28). This does means nothing because this parameter is just for check that everything is going right, and isn't a parameter to optimize.

Fig.6.17 gives us the last confirm that it has to be used a negative amplification for the solution stretch-Y to improve the solution.



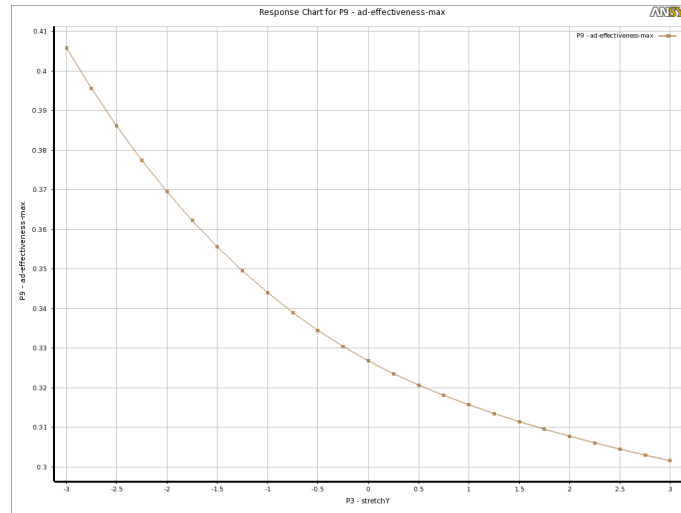


Figure 6.29: Maximum adiabatic effectiveness as a function of stretch Y

### 3D Maps

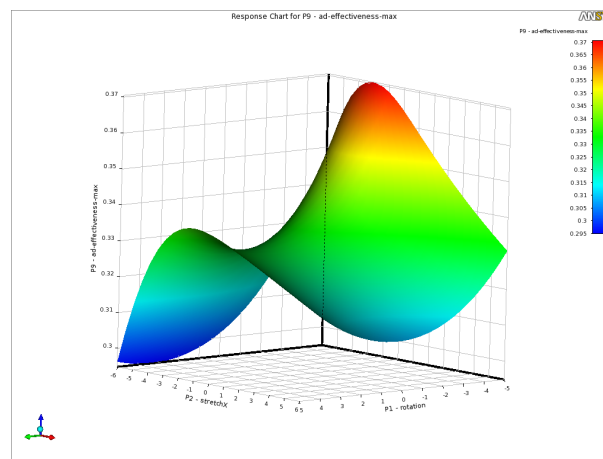


Figure 6.30: Max adiabatic effectiveness as a function of rotation and stretchX

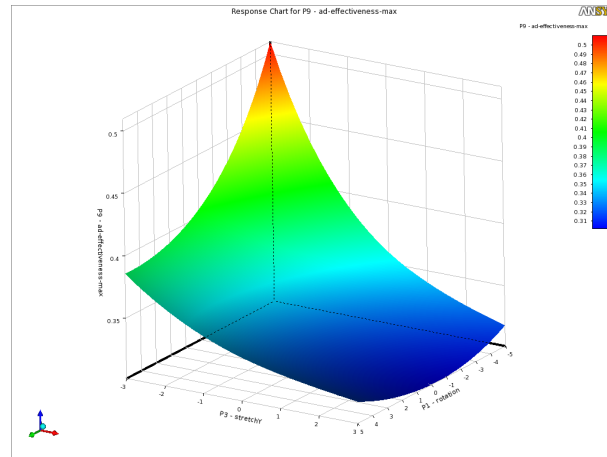


Figure 6.31: Max adiabatic effectiveness as a function of rotation and stretchY

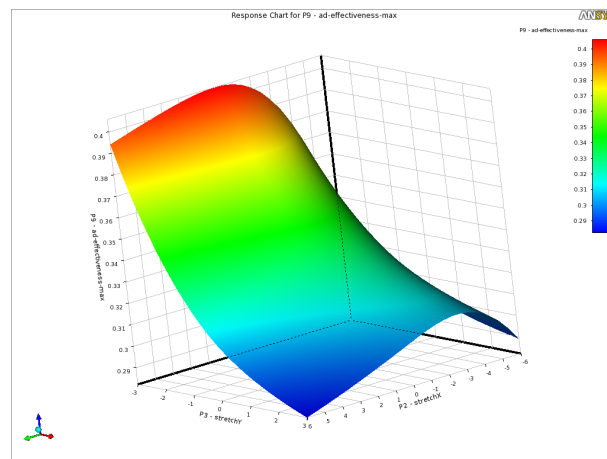


Figure 6.32: Max adiabatic effectiveness as a function of stretchX and stretchY

### 6.3.6 Sensitivity

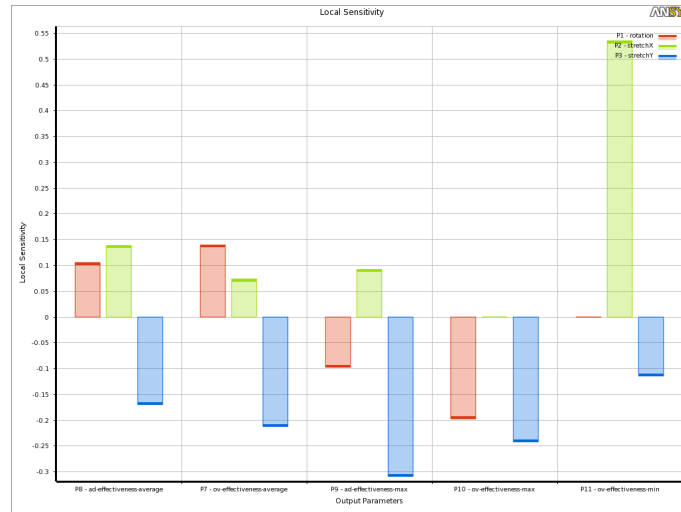


Figure 6.33: Local sensitivity of the all parameters

DesignXplorer has two types of sensitivity charts: the standard Local Sensitivity chart and the Local Sensitivity Curves chart. The Local Sensitivity chart is a powerful project-level tool, allowing you see at a glance the impact of all the input parameters on output parameters.

For each output, it allows you to see the weight of the different input; it calculates the change of the output based on the change of each input independently, at the current value of each input parameter in the project. The Local Sensitivity chart can be displayed as a bar chart or a pie chart.

As can be seen the rotation gives to the baseline an improvement of the average overall effectiveness, average adiabatic effectiveness, no action on the

maximum adiabatic effectiveness and a decreasing of the maximum overall, as said previously till an amplification of 0.7.

The stretchX solution otherwise gives an improvement in every output parameter measured.

Stretch Y solution as said previously gives a worsening of every output parameter, than we will impose a negative amplification of this.

The Local Sensitivity Curves chart helps you to further focus your analysis by allowing you to view independent parameter variations within the standard Local Sensitivity chart. It provides a means of viewing the impact of each input on specific outputs, given the current values of other parameters. Those will be not shown because of the local sensibility curves are very similar to the 2D maps shown in previous subsection, and so don't gives value added.

### 6.3.7 Check Method

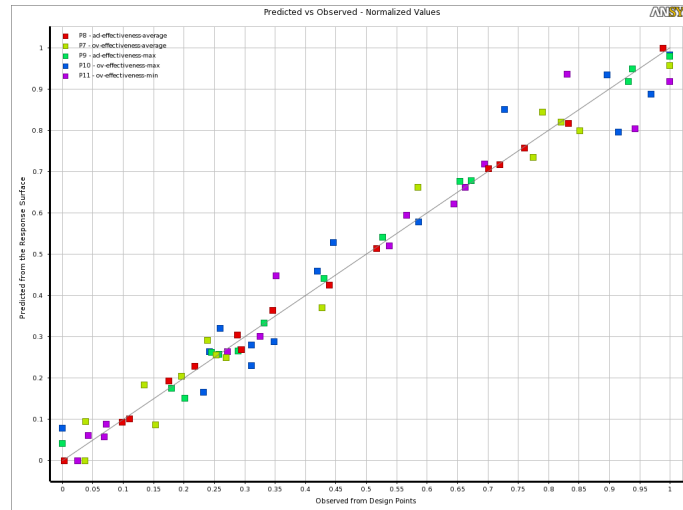


Figure 6.34: Goodness of fit

In the Chart view, a scatter chart presents for each output parameter the values predicted from the response surface versus the values observed from the design points. This chart lets you quickly determine if the response surface correctly fits the points of the Design of Experiments and the refinement table: the closer the points are to the diagonal line, the better the response surface fits the points.

### 6.3.8 Candidate points

Because a good design point is often the result of a trade-off between various objectives, the exploration of a given design cannot be performed by using optimization algorithms that lead to a single design point. It is important to gather enough information about the current design so as to be able to answer the so-called “what-if” questions – quantifying the influence of design variables on the performance of the product in an exhaustive manner. By doing so, the right decisions can be made based on accurate information - even in the event of an unexpected change in the design constraints. Design exploration describes the relationship between the design variables and the performance of the product by using Design of Experiments (DOE), combined with response surfaces. DOE and response surfaces provide all of the information required to achieve Simulation Driven Product Development. Once the variation of the performance with respect to the design variables is known, it becomes easy to understand and identify all changes required to meet the requirements for the product. Once the response surfaces are created, the information can be shared in easily understandable terms: curves, surfaces, sensitivities, etc. They can be used at any time during the development of the product without requiring additional simulations to test a new configuration.

Watching at the Response surface the parameter to be optimize will be set the Average Overall Effectiveness and there will be imposed a constraint on the parameter: Min Overall Effectiveness  $\geq 0.4$ . This will give us the three candidate points:

Candidate Points								
N°	Input Parameter			Output Parameter				
	Rotat. of the holes	Stretch Pitch in X	Stretch Pitch in Y	Over. effect. min.	Over. effect. aver.	Over. effect. max	Adiab. effect. aver.	Adiab. effect. max
1	-5.0	2.6	-3.0	0.483	0.591	0.681	0.266	0.392
2	-4.7	4.1	-2.9	0.482	0.563	0.652	0.260	0.383
3	-0.9	2.0	-2.9	0.452	0.603	0.668	0.273	0.403

And the we can see the trend of the overall effectiveness in the X direction. On the abscissa axis is reported the distance in a non-dimensional way, in order to have the same length for the four curves (that haven't the same length, X pitch is changed).

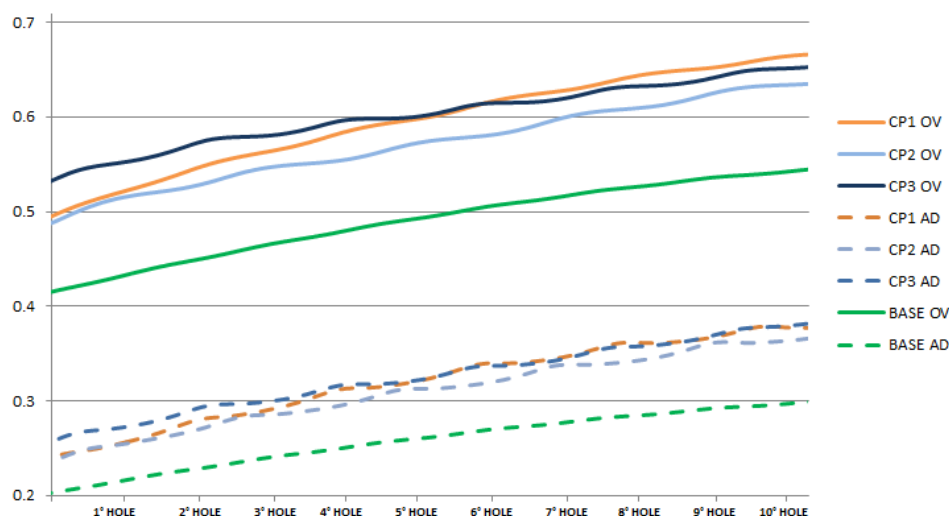


Figure 6.35: Overall and adiabatic effectiveness comparison

So it is palpable that we had a great improvement between 15-20% on the overall effectiveness, and 10 % in adiabatic effectiveness. We have to note that with the CP3 we have a more flat curve, this will give less gradient on the plate, i.e. lower thermal stresses.

Candidate Point 1



Figure 6.36: Overall effectiveness contour of plate in candidate point 1

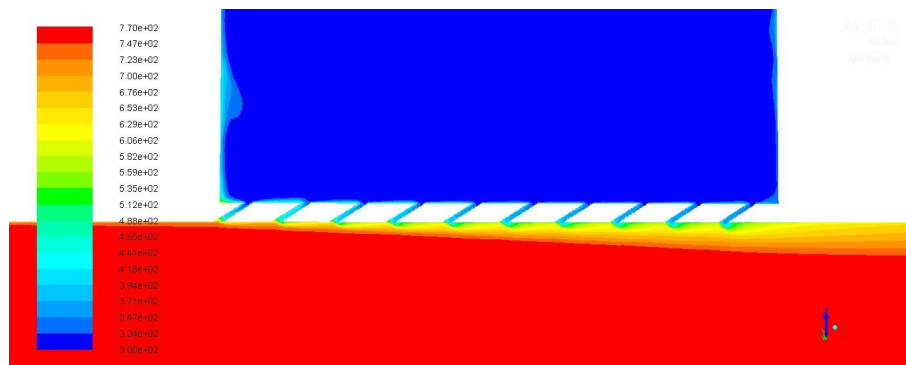


Figure 6.37: Temperature on symmetry plane in candidate point 1



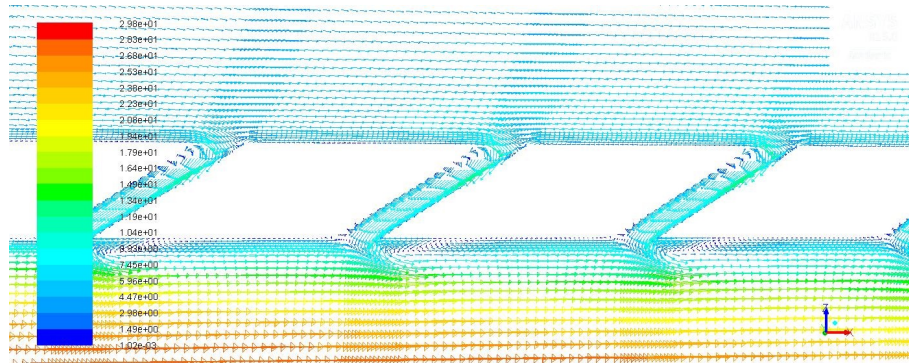


Figure 6.38: velocity vectors on symmetry plane in candidate point 1

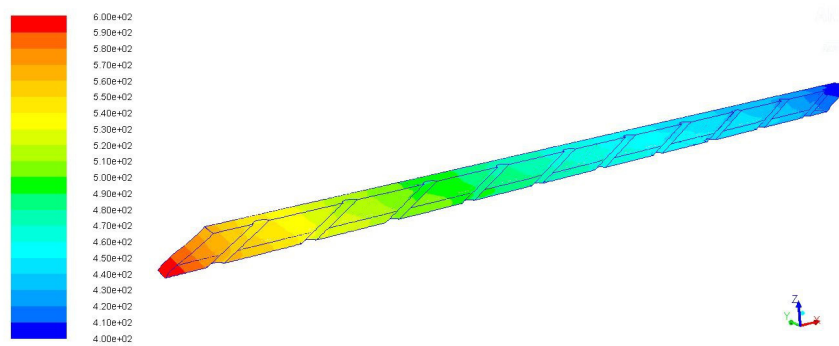


Figure 6.39: Temperature gradient on the plate for candidate point 1

In these four graphics we can see the improvement in the cooling effectiveness, having a better coverage of the plate. But we pay this improvement with a greater detachment zone in the inner of the holes, and a recirculation zone near the exit of the holes. Moreover there is a gradient in X direction about  $200^{\circ}\text{C}$ , but in the thin not more than  $30^{\circ}\text{C}$ .

Candidate Point 2

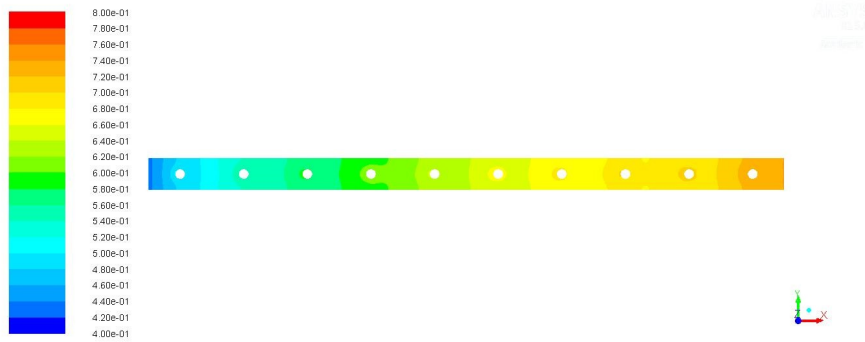


Figure 6.40: Overall effectiveness contour of plate in candidate point 2

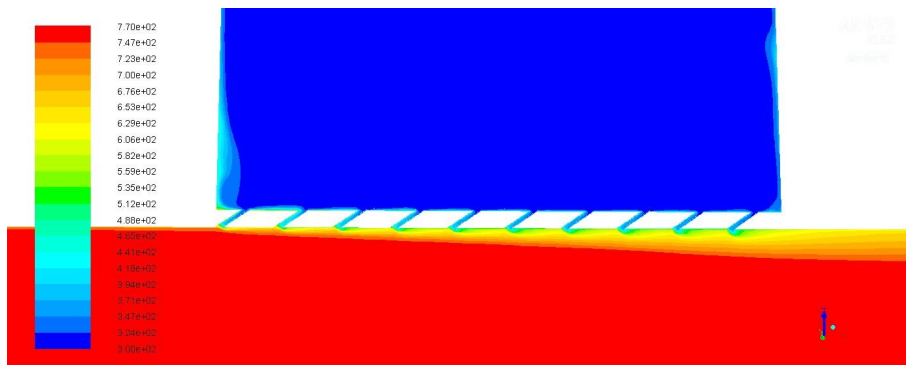


Figure 6.41: Temperature on symmetry plane in candidate point 2

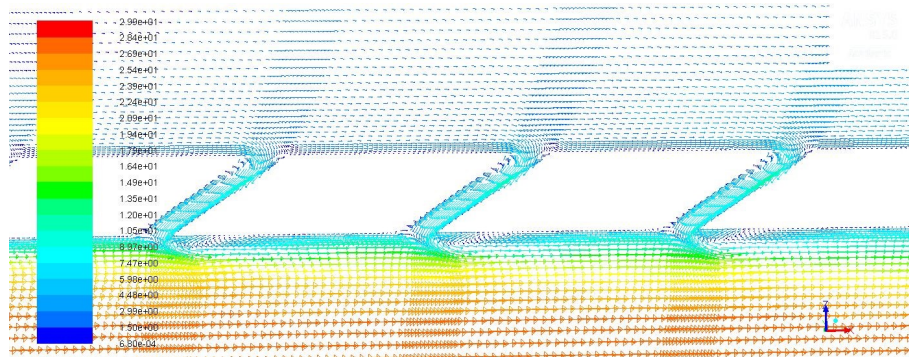


Figure 6.42: velocity vectors on symmetry plane in candidate point 2

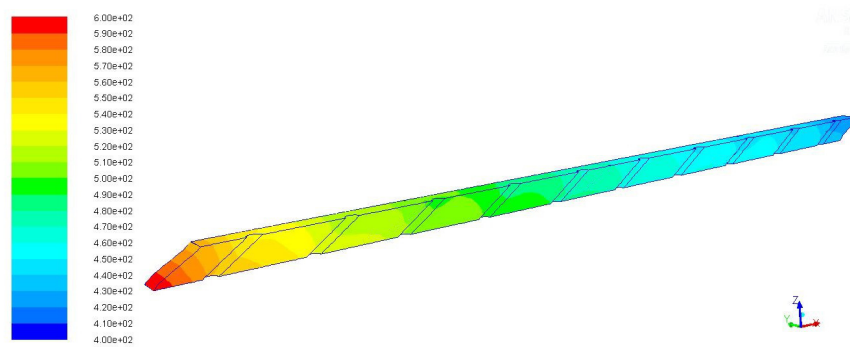


Figure 6.43: Temperature gradient on the plate for candidate point 2

As said for the previous section also in this case we have a better coverage of the plate but greater turbulence zones on the inlet and the outlet of the holes, in this case this phenomenon is also amplified because of the greater rotation of the angle. For this case we have more or less the same temperature gradient along the plate.

**Candidate Point 3**

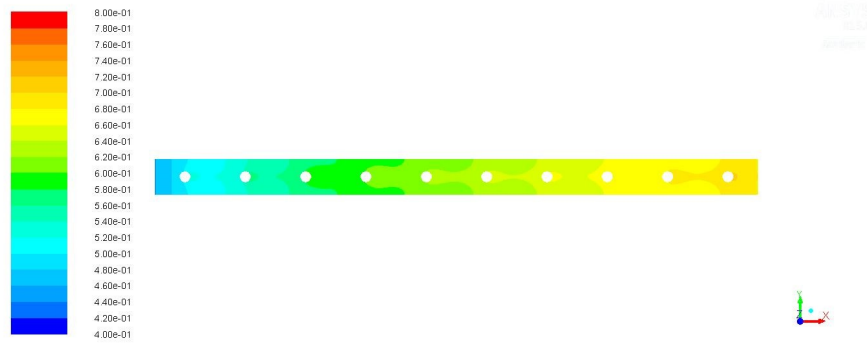


Figure 6.44: Overall effectiveness contour of plate in candidate point 3

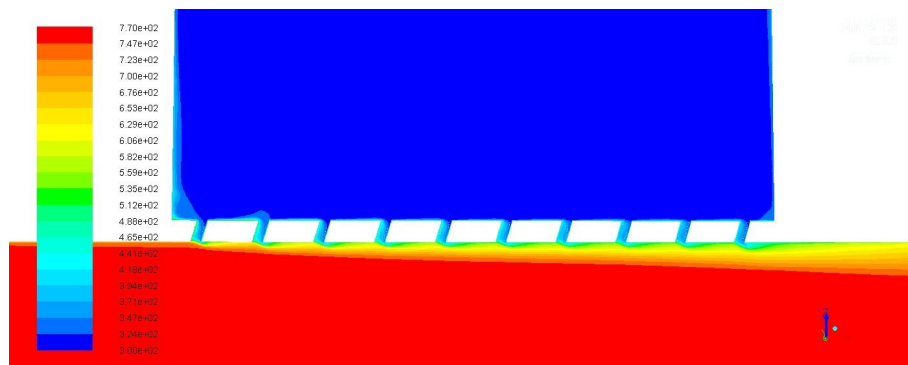


Figure 6.45: Temperature on symmetry plane in candidate point 3

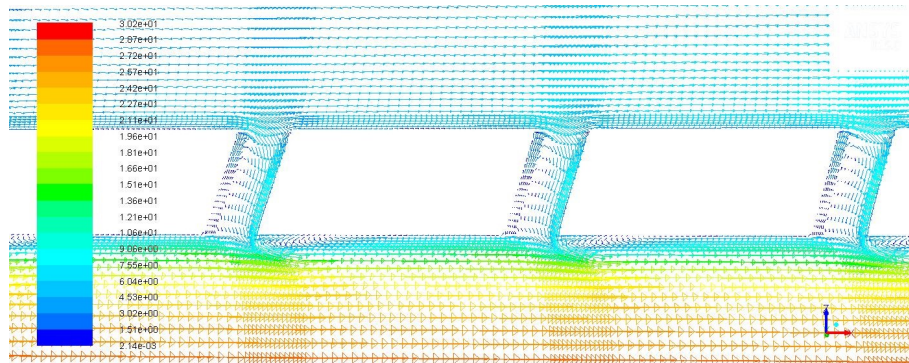


Figure 6.46: velocity vectors on symmetry plane in candidate point 3

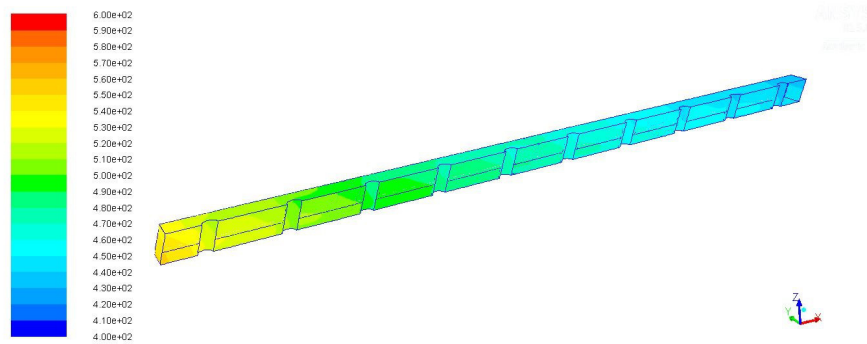


Figure 6.47: Temperature gradient on the plate for candidate point 3

In this case, unlike the previous we have a very small rotation that allows the cooling flow. This reduced drastically the turbulence zones. This also gives a better coverage of the plate than the previous case. We can see also a lower temperature gradient  $\nabla T < 130^{\circ}C$  in X direction and  $\nabla T < 10^{\circ}C$  in Z direction.

## 6.4 Overall effectiveness as a function of $G$

In this section will be shown the trend of the overall cooling effectiveness maximum and minimum, as a function of the coolant mass flow  $G$ . There will be compared two geometry: the baseline, and the candidate point one that gives the best cooling effectiveness.

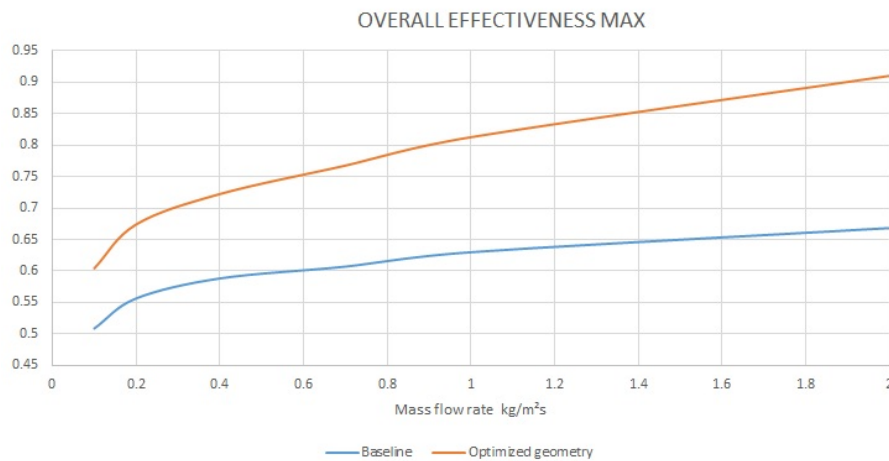


Figure 6.48: Overall effectiveness max as a function of  $G$  in the baseline and optimized geometry

From this chart we can see that with the optimized geometry not only gives a great improvement on the cooling effectiveness, but allows to use a lower coolant mass to have the same effectiveness: for example to have an effectiveness max of 0.65 in the baseline we have to use a coolant mass flow rate of  $1.6 \text{ kg/sm}^2$  and in optimized geometry it is sufficient use coolant mass flow of  $0.1 \text{ kg/sm}^2$ .

However is more significant look at the minimum effectiveness that gives an information of the minimum cooling coverage guaranteed to the plate. Even in this case we can see that to have a minimum effectiveness of 0.55 in

the baseline we have to use a  $2 \text{ kg/sm}^2$  of coolant mass, and in the optimized geometry this mass flow is reduced at  $0.7 \text{ kg/sm}^2$ .

Another important thing to observe is that for both the chart, both the geometry, the curve has a plateau; this means that increasing too much the cooling mass flow rate, after a certain value, is useless because it doesn't give further improvement.

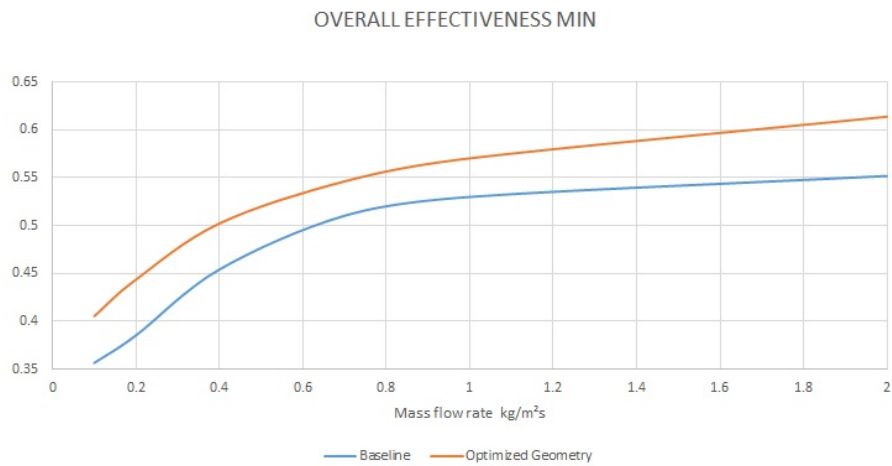


Figure 6.49: Overall effectiveness min as a function of  $G$  in the baseline and optimized geometry

# Conclusions

Full coverage effusion cooling was numerically investigated by means of computational fluid dynamics (CFD) for an array of effusion cooling holes in order to optimise the overall cooling effectiveness.

The influence of hole density per unit surface area, and influence injection angle, on the cooling performances, has been investigated computationally using FLUENT. Experimental data for validation have been taken from the article of G. E. Andrews et al. in "Effusion Cooling: The Influence of the Number of Holes" Proceedings of the Institution of Mechanical Engineers, Part A: Journal of Power and Energy 1990, Showing a maximum disagreement between the prediction and the experimental data of 3%.

The baseline case study considered in this paper consisted of a 152x152x6.35mm perforated wall with a 300K, 0.18  $kg/sm^2$  coolant flow through a square array of 90°effusion holes. The plate is posed a in 770K duct flow.

The effects of three geometrical parameters, i.e. the inclination of the holes, the pitch in X direction and the pitch in Y direction, on the overall cooling effectiveness were investigated without varying the coolant flow rate. The inclination of the effusion holes was varied between -33deg and +33deg from the plane of the plate, while the pitch in both directions was varied between



10.64 mm and 19.76 mm.

Then numerical investigation was performed using the commercial software ANSYS Workbench following a design of experiments approach.

The geometrical modifications were obtained automatically in the CFD solver ANSYS FLUENT for each design point by means of the RBF Morph software. This allowed avoiding the manual modification of the geometry and the subsequent mesh generation.

The optimised configuration was obtained considering the maximisation of the average overall cooling effectiveness as a goal and a chosen minimum value for the local cooling effectiveness as a constraint. Design of experiment approach allowed to generate Response Surfaces, i.e. a surface that shows the variation of the output parameters as a function of 2 input parameters for time, keeping the third input parameter constant.

Results showed that the inclination of the effusion holes and the pitch in the y direction have a greater impact on the cooling effectiveness than the pitch in the x direction, up to 17%, 28% and 5% from the baseline, respectively, within the range of values considered.

Then looking at the response surface the software generated three candidate point to use for the optimization imposing a maximization of the average overall cooling effectiveness, and imposing a minimum overall cooling effectiveness at least 0.45, this means that the minimum temperature allowed in the plate is 558 °C. So an optimal combination of the three parameters considered is finally proposed.

Results of the Candidate Point showed that for the new geometries there are improvement between 15-20% on the overall effectiveness, and 10 % in adiabatic effectiveness. Furthermore for the third candidate point we have lower thermal gradient, and so lower stresses on the plate.

Finally using the geometry proposed in the candidate point 3, an investigation on the influence of the mass flow rate is done. This analysis showed that for a given cooling effectiveness in the baseline, with the new geometry it is possible to use a very lower mass flow rate to have the same effectiveness.

# List of Figures

1.1	A frame-type gas turbine with DLE combustors. . . . .	2
1.2	Three different types of combustion chambers utilized in aircraft and power generation gas turbines. (a) Annular type, (b) tubular type, (c) heavy duty, single cylindrical power generation (BBC)	3
1.3	Generic modular representation of a combustion chamber . . .	4
1.4	A DLN annular combustor in a Siemen’s V94.3 gas turbine . .	7
1.5	A large frame-type gas turbine with two silo-type side combustors	8
1.6	A Combustor . . . . .	8
1.7	Combustion on cool slurry in the externally fired combustor .	11
2.1	Fluent window: “Grid” menù . . . . .	45
2.2	Fluent window: Viscous model . . . . .	46
2.3	Fluent Database Materials . . . . .	47
2.4	Operating Condition & Boundary Condition . . . . .	48
2.5	Solution Controls . . . . .	48
2.6	Solution Methods . . . . .	49
2.7	Monitors . . . . .	50
2.8	Solution Inizialization . . . . .	51

2.9	Run Calculation . . . . .	52
3.1	Experimental Apparatus . . . . .	68
3.2	Computational Apparatus . . . . .	69
3.3	Area averaged cooling effectiveness as a function of G at the last termocouple . . . . .	72
3.4	Variation of $\eta_{ov}$ with axial distance from LE of the wall for $G=0.18 \text{ kg/sm}^2$ . . . . .	75
4.1	Base Geometry . . . . .	77
4.2	Mesh . . . . .	77
4.3	Mesh Detail . . . . .	79
4.4	Start Mesh . . . . .	80
4.5	Refined Mesh . . . . .	80
4.6	CFD Geometry . . . . .	81
4.7	Plate detail . . . . .	83
4.8	Overall effectiveness in function of distance from the leading edge. Comparison with experimental data . . . . .	88
4.9	Overall effectiveness in function of distance from the leading edge comparison with experimental data . . . . .	89
4.10	Overall effectiveness in function of distance from the leading edge comparison with experimental data . . . . .	89
4.11	Overall effectiveness in function of distance from the leading edge comparison with experimental data . . . . .	90

---

4.12 Overall effectiveness in function of distance from the leading edge comparison with experimental data . . . . .	90
4.13 Overall effectiveness. Comparison of different turbulence models in refined mesh. . . . .	91
4.14 Temperature contours on symmetry plane . . . . .	92
4.15 Velocity vectors on symmetry plane . . . . .	93
4.16 Molar concentration of tracer . . . . .	93
4.17 Overall effectiveness contours on the plate . . . . .	94
4.18 Comparison of overall effectiveness between the different meshes and turbulence models . . . . .	95
5.1 Display Points . . . . .	98
5.2 Preview Points . . . . .	98
5.3 Base . . . . .	99
5.4 Amplification 5 . . . . .	99
5.5 Display Points . . . . .	100
5.6 Preview Points . . . . .	100
5.7 Base . . . . .	101
5.8 Amplification 5 . . . . .	101
5.9 Display Points . . . . .	102
5.10 Preview Points . . . . .	102
5.11 Base . . . . .	103
5.12 Amplification 5 . . . . .	103
6.1 Ansys Workbench project . . . . .	111

---

6.2	Design of experiments . . . . .	111
6.3	Average Overall effectiveness as a function of rotation . . . . .	114
6.4	Average Overall effectiveness as a function of stretch X . . . . .	115
6.5	Average Overall effectiveness as a function of stretch Y . . . . .	115
6.6	Average Overall effectiveness as a function of rotation and stretchX	116
6.7	Average Overall effectiveness as a function of rotation and stretchY	116
6.8	Average Overall effectiveness as a function of stretchX and stretchY . . . . .	117
6.9	Maximum Overall effectiveness as a function of rotation . . . . .	117
6.10	Maximum Overall effectiveness as a function of stretch X . . . . .	118
6.11	Maximum Overall effectiveness as a function of stretch Y . . . . .	119
6.12	Maximum Overall effectiveness as a function of rotation and stretchX . . . . .	119
6.13	Maximum Overall effectiveness as a function of rotation and stretchY . . . . .	120
6.14	Maximum Overall effectiveness as a function of stretchX and stretchY . . . . .	120
6.15	Minimum Overall effectiveness as a function of rotation . . . . .	121
6.16	Minimum Overall effectiveness as a function of stretch X . . . . .	121
6.17	Minimum Overall effectiveness as a function of stretch Y . . . . .	122
6.18	Minimum Overall effectiveness as a function of rotation and stretchX . . . . .	122

6.19	Minimum Overall effectiveness as a function of rotation and stretchY . . . . .	123
6.20	Minimum Overall effectiveness as a function of stretchX and stretchY . . . . .	123
6.21	Average adiabatic effectiveness as a function of rotation . . . .	124
6.22	Average adiabatic effectiveness as a function of stretch X . . .	125
6.23	Average adiabatic effectiveness as a function of stretch-Y . . .	125
6.24	Average adiabatic effectiveness as a function of rotation and stretchX . . . . .	126
6.25	Average adiabatic effectiveness as a function of rotation and stretchY . . . . .	126
6.26	Average adiabatic effectiveness as a function of stretchX and stretchY . . . . .	127
6.27	Maximum adiabatic effectiveness as a function of rotation . . .	127
6.28	Maximum adiabatic effectiveness as a function of stretch X . . .	128
6.29	Maximum adiabatic effectiveness as a function of stretch Y . . .	129
6.30	Max adiabatic effectiveness as a function of rotation and stretchX	129
6.31	Max adiabatic effectiveness as a function of rotation and stretchY	130
6.32	Max adiabatic effectiveness as a function of stretchX and stretchY	130
6.33	Local sensitivity of the all parameters . . . . .	131
6.34	Goodness of fit . . . . .	133
6.35	Overall and adiabatic effectiveness comparison . . . . .	135
6.36	Overall effectiveness contour of plate in candidate point 1 . . .	136

---

6.37	Temperature on symmetry plane in candidate point 1 . . . . .	136
6.38	velocity vectors on symmetry plane in candidate point 1 . . . . .	137
6.39	Temperature gradient on the plate for candidate point 1 . . . . .	137
6.40	Overall effectiveness contour of plate in candidate point 2 . . . . .	138
6.41	Temperature on symmetry plane in candidate point 2 . . . . .	138
6.42	velocity vectors on symmetry plane in candidate point 2 . . . . .	139
6.43	Temperature gradient on the plate for candidate point 2 . . . . .	139
6.44	Overall effectiveness contour of plate in candidate point 3 . . . . .	140
6.45	Temperature on symmetry plane in candidate point 3 . . . . .	140
6.46	velocity vectors on symmetry plane in candidate point 3 . . . . .	141
6.47	Temperature gradient on the plate for candidate point 3 . . . . .	141
6.48	Overall effectiveness max as a function of G in the baseline and optimized geometry . . . . .	142
6.49	Overall effectiveness min as a function of G in the baseline and optimized geometry . . . . .	143



# Bibliography

- [1] Andrews, G. E. and Kim, M. N. "*The influence of film cooling on emissions for a low radial swirler gas turbine combustor*" in ASME International Gas Turbine & Aeroengine Congress & Exhibition, New Orleans, 2001.
- [2] H. I. Oguntade, G. E. Andrews, A. D. Burns, D. B. Ingham<sup>2</sup> and M. Pourkashanian "*Conjugate Heat Transfer Predictions of Effusion Cooling with Shaped Trench Outlet*" Proceedings of ASME Turbo Expo, Dusseldorf, Germany, 2014
- [3] H. I. Oguntade, G.E. Andrews, A. D. Burns, D. B. Ingham and M. Pourkashanian "*Conjugate Heat Transfer Predictions of Effusion Cooling: The Influence Hole Density on Cooling Performance*" Proceedings of ASME Turbo Expo, 2014
- [4] G.E.Andrews "*Effusion cooling backside crossflow cooling and the backside coolant mass flow rate*" Proceedings of ASME Turbo Expo, San Antonio, USA, 2013
- [5] G.E.Andrews "*Full coverage effusion cooling with a narrow duct backside coolant supply*" Proceedings of ASME Turbo Expo, Copenhagen,

Denmark, 2012

- [6] Luca Andrei, Antonio Andreini, Cosimo Bianchini, Gianluca Caciolli, Bruno Facchini, Lorenzo Mazzei, Alessio Picchi, Fabio Turrini ” *Effusion cooling plates for combustor liners: experimental and numerical investigations on the effect of density ratio* ” 68th Conference of the Italian Thermal Machines Engineering Association, ATI2013
- [7] Antonio Andreini, Bruno Facchini, Lorenzo Mazzei, Alessio Picchi, Fabio Turrini ” *Experimental and Theoretical Investigation of Thermal Effectiveness in Multiperforated Plates for Combustor Liner Effusion Cooling* ” Journal of turbomachinery, 2014
- [8] J.J. Scrittore, K.A. Thole, S.W. Burd ” *Investigation of Velocity Profiles for Effusion Cooling of a Combustor Liner* ” Transactions of the ASME, 2007
- [9] Reaz Hasann, AginPuthukkudi ” *Numerical study of effusion cooling on an adiabatic flat plate* ” Propulsion and Power Research, 2013
- [10] Bohn, D., Ren, J. and Kusterer, K. ” *Conjugate Heat Transfer Analysis for Film Cooling Configurations With Different Hole Geometries* ” in ASME Conference Proceedings 2003
- [11] Ceccherini, A., Facchini, B., Tarchi, L., Toni, L. and Coutandin, D. ” *Combined Effect of Slot Injection, Effusion Array and Dilution Hole on the Cooling Performance of a Real Combustor Liner* ” in ASME Conference Proceedings, 2009

- 
- [12] Harrington, M. K., McWaters, M. A., Bogard, D. G., Lemmon, C. A. and Thole, K. A. " *Full-Coverage Film Cooling With Short Normal Injection Holes* " Journal of Turbomachinery, 2001
- [13] Dorrington, J.R., Bogard, D.G., and Bunker R.S. " *Film Effectiveness Performance for Coolant Holes Embedded in Various Shallow Trench and Crater Depressions* " Proc. ASME Turbo Expo 2007
- [14] Andrews, G.E., F. Bazdidi-Tehrani, C.I. Hussain, and J.P. Pearson " *Small Diameter Film Cooling Hole Heat Transfer: The Influence of the Hole Length* " ASME Paper, 1991
- [15] Ceccherini, A., Facchini, B., Tarchi, L., and Toni, L. " *Adiabatic and Overall Effectiveness Measurements of an Effusion Cooling Array for Turbine Endwall Application* " ASME Paper 2008
- [16] Cho HH, Goldstein RJ. " *Heat (mass) transfer and film cooling effectiveness with injection through discrete holes: Part I-within holes and on the back surface.* " ASME J Turbomach 1995
- [17] Cho HH, Rhee D-H " *Local heat/mass transfer measurement on the effusion plate in impingement/effusion cooling systems* " Journal of Turbomachinery 2001
- [18] G E Andrews, A A Asere, M L Gupta and M C Mkpadi " *Effusion Cooling: The Influence of the Number of Holes* " Proceedings of the Institution of Mechanical Engineers, Part A: Journal of Power and Energy 1990

- 
- [19] Meherwan P. Boyce *"Gas Turbine Engineering handbook"* Elsevier 2012
- [20] Johannes Janicka, Amsini Sadiki, Michael Schafer, Christof Heeger *"Flow and Combustion in Advanced Gas Turbine Combustors"* Springer 2013
- [21] R.S. L. Lee .J. H. Whitelaw·1 S.Wung (Eds.) *"Aerothermodynamics in Combustors "* Springer 1991
- [22] *"Fundamentals of Fluid Mechanics"* Springer 2013
- [23] Munson, Young, Okiishi, Huebsech *"Flow and Combustion in Advanced Gas Turbine Combustors"* Wiley 2009
- [24] Frank White *"Fluid Mechanics"* McGraw-Hill